



POLITECNICO DI MILANO

ELECTRICAL ENGINEERING DEPARTMENT – ENERGY DEPARTMENT

DOCTORAL PROGRAMME IN ELECTRICAL ENGINEERING

AN INSULATION CAUSE OF FAILURE IN ELECTRICAL MACHINES AND DIAGNOSTIC TOOLS FOR A RAILWAY APPLICATION

Doctoral Dissertation of:

Matteo Maria Maglio

Supervisor:

Prof. Francesco Castelli Dezza

Tutor:

Prof. Antonino Di Gerlando

The Chair of the Doctoral Program:

Prof. Alberto Berizzi

2013 – XXV Cycle

CONTENTS

INTRODUCTION	III
Summary	IV
1 Overvoltage Originated by Square-Wave Feeding of AC Electrical Machines – Insulation Property and Standards	1
1.1 Insulation base concept and standards.....	2
1.2 Insulation resins, VPI process and tapes.	5
1.3 Stator winding tests.....	9
References.....	15
2 Motor Overvoltage Analysis in PWM AC Drives Using a Universal Model	16
2.1 Overvoltage Effects	17
2.2 System Parameters Computation and Filter Design.....	19
2.3 Simulation Results and Model Validation	26
References.....	33
3 Voltage Distribution Inside a Coil	35
3.1 Coil Model and Voltage Distribution	36
3.2 Solution Algorithm	40
3.3 Simulation Results.....	41
References.....	47
4 Diagnostic Tools for Railway Systems – Telemetry Axle Power Feeding.....	49
4.1 Strain Measurement.....	50
4.2 High Frequency Induction Power Feeding	54
4.2.1 Resonant Winding	62
4.2.2 Non-resonant windings	75
4.3 Contactless Energy Transfer Using Rectifying Antennas	83
4.4 Energy Transfer on Rotating Shafts Using PM Printed-Winding Machine	94
References.....	105
CONCLUSIONS	108
APPENDICES.....	110
Appendix A	111
Appendix B.....	123
Appendix C.....	128
Appendix D	136

INTRODUCTION

This Ph.D. thesis is based on the work the author performed during the three years course spent in the XXV Doctoral programme in Electrical Engineering at Politecnico di Milano, Italy.

The research was supported by the “Dipartimento di Elettrotecnica” (Electrical Engineering Department), the “Dipartimento di Meccanica” (Mechanical Engineering Department), the “Dipartimento di Energia” (Energy Department), ITALCERTIFER, the certification authority for the Italian railway system and MCM Energy Lab, a spin-off of Politecnico di Milano University.

The main topic of the research is “An insulation cause of failure in electrical machines and diagnostic tools for a railway application”.

Basing on this topic the author focused on two different aspects; the first is related to the electrical machine’s diagnostic and the second is related to the development of diagnostic tools for monitoring a real important part of the train: the train axle.

The electrical machine diagnostic is a very wide topic and in the past years a lot of aspects have been faced. Very powerful tools have been produced to better analyze the machines and to deeply understand the fault causes. Nowadays state observers, precise sensors and estimation algorithms have been integrated resulting in more efficient and reliable tools for the electrical machine’s diagnostic. A particular cause of insulation fault has been analyzed in this work and some considerations not always well-recognized by the machine’s manufacturer, are derived. Simulation tools and computation algorithm help in supporting this observations.

The second aspect of the thesis comes from a research on the train axle diagnostic tools. The axle is a vital part of the train and its continuous monitoring can significantly improve the safety in the railway transportation system.

Strain supervision requires proper sensors and a reliable electrical power source to guarantee an effective measurement. Different technologies are shown and compared in this work.

SUMMARY

In the first chapter one of the fault causes in an electrical machine is analyzed focusing on the train traction motor system. The analysis of the state of the art of the insulation systems for the electrical machines leads to the study of the electrical stress that the insulation stands when the voltage excitation is made of repetitive voltage steps with very steep fronts.

A fast review of the insulation systems along with the main tests to be performed for the qualification are described. The main importance is given to the tests and qualifying process for an insulation system of an electrical machine fed by a power electronic converter. An inside look is given to the construction techniques and to the present regulations for designing and testing the insulation system.

In the second chapter, a new induction motor model is derived, which can simulate the low-to-high frequency phenomena like the motor terminals over-voltages and voltage oscillations. The extension of the classic induction motor model with high frequency components is based on the motor frequency response in a wide frequency range and brings the simulation response to more realistic results.

The over-voltage effect is studied not only at the motor terminals but also inside the winding in the third chapter thanks to an analytical simplified model which can be useful to investigate the effect of the turn-to-turn and turn-to-ground capacitances on the voltage distribution.

The second part of the research starts in chapter four and is based on the diagnostic tools for the train axle. The axle strain monitoring is an effective technique to prevent massive damage to the train. The measurement of the axle strain needs sensors, data acquisition units and data transmission units that lean on the rotating shaft and, most important, need to be electrically powered. Nowadays there are some commercially available devices for the strain measurement and all of them avoid slip rings and direct contact with the shaft.

The analysis of three different solutions is carried out along with some tests performed to validate the results and verify the effectiveness of these solutions. Each of them is associated with the analytical study of the system, where possible, or with the computation of the parameters of interest through a finite element analysis software.

The first solution is an high frequency induction power feeding system which involves a primary and a secondary winding in a coreless transformer. The system equations and the design parameters for the transferred power evaluation are derived considering series resonant windings for efficiency enhancement.

The second solution is a radio frequency transmission system. Thanks to patch and rectifying antennas, DC power can be collected from a radio transmitter. The evaluation of the transferred power is performed thanks to a 3D simulation of the train axle and antennas.

The third solution relies on the construction of a Permanent Magnets (PM) printed-winding machine mounted on a bearing structure on the axle. The rotating windings are printed on a rotating circuit board while the magnets are fasten to the stator bearing track. The machine works as a PM generator which transfers energy to the rotating windings and thus to the rotating telemetry system.

For all the solutions the main advantages and drawbacks are underlined. The performance results of each feeding system show to the reader which technology can be more easily used for the next future axle monitoring system.

1 OVERVOLTAGE ORIGINATED BY SQUARE-WAVE FEEDING OF AC ELECTRICAL MACHINES – INSULATION PROPERTY AND STANDARDS

The first part of the thesis deals with the insulation systems for the electrical machine and the voltage stress when the machine's winding is powered by an electronic converter. The state of the art of the acceptance and qualification tests are described together with the reference standards for designing an insulation system when the electrical machine is powered by repetitive voltage pulses that come from an electronic converter, as a PWM inverter or a controlled rectifier.

1.1 INSULATION BASE CONCEPT AND STANDARDS

This section is not an exhaustive explanation of the insulation system process or of the testing methods but is just a small look inside this topic which, in the research field of materials, plants, testing instruments and procedure, involved the very beginning of the author's research and his first cooperation with a company which produces low to high voltage wind generators. The insulation construction and testing is a very wide topic which started as the electrical machines and plants started to be made. New materials and manufacturing technologies improved the machine's performance a lot in the past 40 years and recently the insulation technologies are facing the challenge of the high voltage power feeding through repetitive voltage pulses. The circulation of high performances power converters has increased a lot and the whole machine's construction has to deal with this changed scenario.

The standards in this field are the IEC 60034-18-41 and the IEC 60034-18-42 respectively for the Qualification and Type tests for Type I electrical insulation systems and the Qualification and Acceptance tests for partial discharge resistant electrical insulation systems (Type II) used in rotating electrical machines fed from voltage converters.

The difference between Type I and Type II is that the Type I system refers to the insulation system made of organic enamel normally used in low voltage windings while the Type II system is made of tapes and materials resistant to partial discharges and are normally used in the medium-high voltage windings.

Partial discharge (PD) is the phenomenon for which a small electrical discharge is released in a medium due to the enhancement of the electrical field in the medium itself. So obviously it depends not only on the electrical field strength but also on the intrinsic features of the materials involved. When a small electrical discharge is generated it affects the material that is hit by the discharge. The name "partial" comes from the fact that the discharge is confined to a small space of the material around the point where the discharge arose. A partial discharge example is the well-known Corona effect on the high voltage overhead power lines. Small discharges are created between the conductor and the air surrounding as the voltage, and so the electric field, pass the discharge limit due to the air condition like humidity, pressure and chemical composition. The same phenomenon can be observed in the insulating material and in particular inside the small air-gap left during the insulation system construction.

The situation is shown in the Figure 1.1:

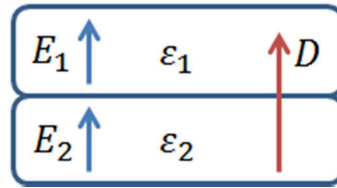


FIGURE 1.1 ELECTRICAL FIELD DISTRIBUTION

Two different materials, as can be air and Mica tapes, have two different electric permittivity. Typically the relative permittivity of air is equal to 1 while the relative permittivity of Mica goes from 3 to 6.

Being D the electric displacement, equal for both the materials, the following stands:

$$D = \epsilon_1 \cdot E_1 \quad (1.1)$$

$$D = \epsilon_2 \cdot E_2 \quad (1.2)$$

And so:

$$\epsilon_1 \cdot E_1 = \epsilon_2 \cdot E_2 \quad (1.3)$$

Being E_1 the electric field in the air and E_2 the electric field in the Mica, means that:

$$E_1 = \frac{\epsilon_2}{\epsilon_1} E_2 \quad (1.4)$$

So, as easily explained, the electric field in the air-gap can be 3 to 6 times higher than the electric field in the Mica tapes. Due to this relation small discharges can be generated in the air-gap leading to the Partial Discharge phenomenon. The small discharges can increase the temperature and locally burn the insulating material resulting in a more wide discharge and finally to a total discharge that, based on the air-gap position, can results in an inter-turn discharge or in a ground discharge.

The organic enamel insulation has molecular structure which, subjected to partial discharge, breaks up its internal connection and burns the insulation away. So for this kind of insulation system the standard IEC 60034-18-41 impose some tests to verify that in normal operating condition no partial discharges have to be registered otherwise the insulating enamel would be corrupted resulting in a winding inter-turn fault or ground fault.

The inorganic material used in Type II system is based on Mica, a special group of sheet silicate (phyllosilicate) minerals, particularly resistant to partial discharges. On the contrary the Mica tapes used for the insulation system are very friable and so they need a stronger support in order to increase its mechanical strength. To this purpose a glass fiber layer is joint with the Mica tape to form a robust and PD resistant tape.

The winding construction can be divided in two families: the "Random Wound" windings and the "Form Wound" windings. For the first the term "Random" refers to the construction of each turn of the coil which is laid in the slot without a predefined order as shown in Figure 1.2. Usually this kind of windings are used for the low voltage machine for all the kind of motors and generators and its insulation system is made of organic enamel and resin to fill the air-gap and bind the wires.

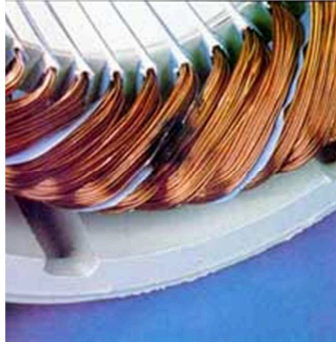


FIGURE 1.2 RANDOM WOUND WINDING

The “Form Wound” winding is instead made of copper bars neatly arranged in the slots to fill them properly basing on the machine’s design. This kind of system is used for high current density windings and the insulation material is mainly composed by an inter-turn tape that separates the coil’s turns and a ground cover which isolates the windings from the stator core.

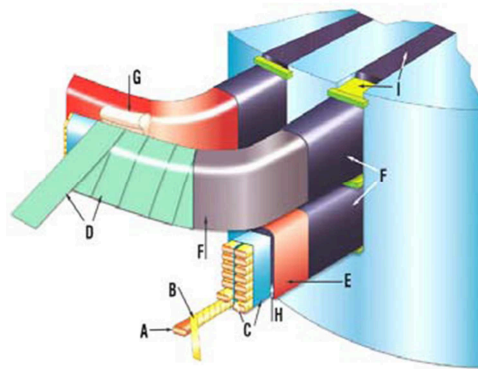


FIGURE 1.3 FORM WOUND COIL AND INSULATION TAPES

In Figure 1.3 a typical form wound insulation system is shown. It can be divided in the following parts:

- Winding wire (A)
- Conductor insulation (B)
- Stack consolidation (C)
- Main wall insulation: Mica tape (D) + resin (H)
- Conductive and stress grading paint or tape (F)
- Finishing or sealing tapes (E)
- Bracing materials (G)
- Slot wedging materials (I)

The stress grading tape (F) is used to grade the voltage enhancement between the stator core (zero voltage) and the copper bar (high voltage) at the slot exit toward the coil head. This way there’s no a high voltage difference between the coil and the ground that could generate PD. Also the Conductive paint or tape is used for the same purpose as it cancels the voltage difference between the main wall insulation and the core preventing the PD in the air-gap at the bottom of the slot.

1.2 INSULATION RESINS, VPI PROCESS AND TAPES.

As explained in the previous section the air-gap left in the insulation system can lead to partial discharges and so can damage the whole insulation system. Some kind of insulation, like the one of the random wound coils, are designed for low voltage application and there's no need to remove the air between the turns or between the turns and the stator core.

The benefit of resins, varnish and enamel in the winding construction can be summarized in the following points:

- Remove the air in the insulation gaps.
- Paste the coils and guarantee mechanical resistance.
- Enforce the electrical insulation.
- Improve the heat transfer from the copper to the core.
- Preserve and protect the windings from high temperature and environmental pollution.

A solvent is added to make the resin more fluid. It allows the resin to penetrate deeper inside the winding and fill all the air gaps. During the drying phase the solvent vaporizes leaving only the resin in contact with the winding. There are different kind of resins with different chemical composition. The mainly used one with some of their features are:

- **Polyester:** commonly used with solvent; mechanical and electrical weakness at high temperature.
- **Epoxy:** commonly used without solvent in the impregnation process; relatively high viscosity. Good mechanical and chemical properties but lower dielectric and thermal performance at high temperatures. System most commonly used in high voltage provides for the use of two components: Epoxy + Anhydride for a class F system.
- **Polyesterimide:** similar to the polyester but with higher dielectric characteristics at high temperatures. Performance in class H, excellent compatibility with the enamel.
- **Silicon:** structure resistant to high temperature; applications in class C for traction motors. Weak mechanical and chemical resistance and high manufacturing costs.

Another parameter of great interest for the resin is the viscosity which describes the ability of the resin to flow into the core through the insulating tapes.

A low viscosity brings the resin deep into the winding tapes and let the resin in excess to flow away after the impregnation process. On the other side when a low viscosity resin is dried, it leaves a thin coat more resistant to crack but less resistant in time.

In high-voltage applications the viscosity depends on the characteristics of the main insulation and should always be linked to its reactivity, i.e. the ability to change due to exposure to air or high temperatures in the cooking oven.

One aspect of reactivity is the Gel time defined as the time at which the resin begins to cure (solidify) at a given temperature.

If the gel time is too short there can be stability problems, poor drainage and considerable thickness for the resin deposited and consequent risk of fractures

A remedy may be the addition of inhibitors of the solutions inside solidification of the resin or paint.

A Gel time too long, however, may cause excessive drainage, resin thickness too thin and so little protection, worsening the productivity process.

In this case a catalytic agent can be added to promote the densification.

A second aspect of reactivity is the drying time (curing time), defined as the time that is required for the resin to be completely dried at a given temperature. The resin is completely dried when the polymerization process is finished.

At the end of the insulation process the resin must be completely dried in order to avoid gas vaporization when the machine is in operation and mass reduction in the resin content that would generate air gaps bringing to partial discharges in insulation. Moreover the best mechanical and chemical properties are obtained after curing which also ensure a long insulation life.

The reactivity of the resin should be checked regularly, at least monthly, to ensure that the resin maintains its original properties.

A growing number of manufacturers of electrical machines is applying the VPI technology (Vacuum Pressure Impregnation) as a method to isolate the electrical parts of the machine.

The VPI technology is well established and has proven to give a high level of performance and reliability if the insulation material is carefully selected according to the machine. This insulating method starts from taping the new winding bars, so called “green coils”, with glass-mica tapes already soaked with a resin content of 10% to 25% of the total resin required for the insulation. The remaining part of resin is supplied from immersion of the component in an autoclave. Thanks to the vacuum generated, the winding is filled with the low viscosity resin in order to ensure good penetration into all the air-gaps. The VPI technology can be divided in global impregnation and single bar impregnation

- Global impregnation: The whole machine, or a part of it, is mounted with the green bars and then is dipped into the resin.
- Single bar impregnation: every single copper bar is impregnated in the autoclave and then placed in the core slots.

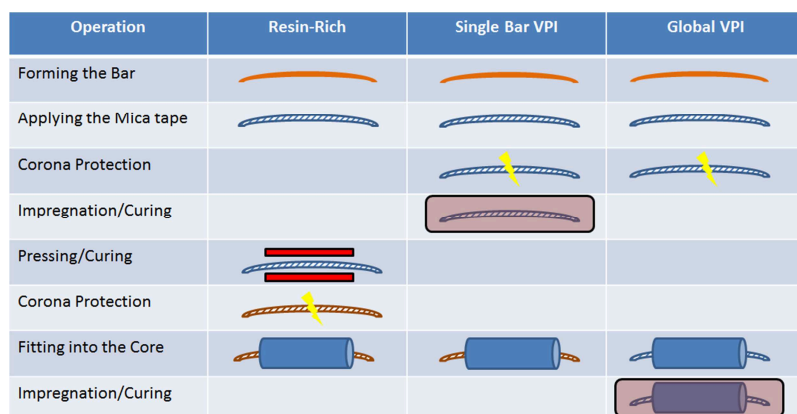


FIGURE 1.4 VPI AND RESIN RICH PROCESS

Another insulation method is the Resin-Rich process. It does not require an autoclave and so is a less expensive method. Single bars are treated with fully-impregnated Mica tapes which are pressed and cured on the bars.

Then the bars are fitted into the machine's slots. The results are not as satisfying as for the VPI process and more resin is wasted in the pressing and curing process. On the contrary, VPI process requires more resin to be stored into tanks because the bars must be fully dip into the resin and this results in a more complex and expensive plant.

In Figure 1.4 the difference between the global VPI, the single bar impregnation and the resin-rich process is shown.

The comparison between the VPI and the resin-rich method is summarized in the Table 1.

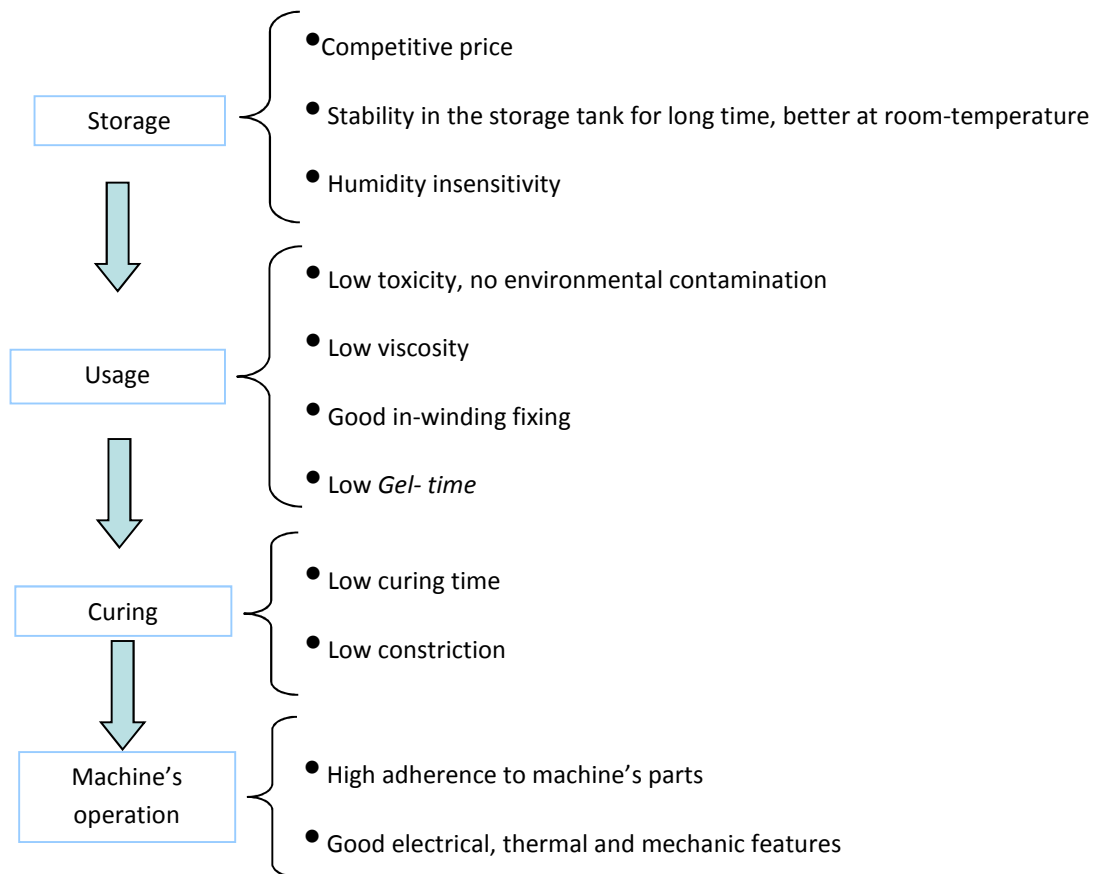
TABLE 1 IMPREGNATION PROCESS COMPARISON

	Resin – rich	VPI single bar	VPI global
Pros	The copper bars could be tested before fitting into the machine.	The copper bars could be tested before fitting into the machine.	Hermetic enclosure of the whole machine. Lower costs in comparison with the single bar VPI
Cons	High costs and delicate process	High costs	No test on the impregnated bars, difficult to remove for maintenance.

So thanks to the VPI process it's possible to effectively fill the air gaps in the insulation layers and provide a good mechanical strength for the windings. Furthermore the resin improve the heat transfer to the iron core and protect the bars from environmental pollution which, in the case of off-shore wind generators, is particularly important.

The resin is just a part of the whole VPI plant but, in order to have an efficient impregnation process, must be properly selected basing on the production cycle.

For every stage of the insulation process, different features must be considered in the resin choice. The diagram below shows some of them:



The resin choice must also respect the machine's features according to the nominal voltage which determines the insulation thickness, the thermal class (155, 180, >180), resin's stability and its reuse and the VPI plant maintenance. In Table 2 some resin features are summarized.

TABLE 2 RESIN FEATURES [5]

Resin \ Feature	Polyester	Polyesterimide	Epoxy hybrid	Epoxy – Anhydride	Epoxy catalyzed
Thermal Class	F	H	F	F	F
Life endurance	Medium	High	Moderate	Moderate/High	Moderate/High
Storage temperature	<Room-temp.	Room-temp.	5 ⁰ - 10 ⁰	<Room-temp.	<Room-temp.
Humidity sensitivity	NO	NO	SI	SI	NO
Polluting component	Styrene	Styrene	Styrene	Anhydride	-
Impregnation temperature	Room-temp.	Room-temp.	Room-temp.	40 ⁰ - 70 ⁰	Room-temp. – 60 ⁰ C
Impregnation penetration	Moderate	Moderate	Good	Good	Good
Gel – time (120 ⁰) [min]	15 – 30	2 – 4	5 – 10	3 – 6	>100

Curing time	Moderate/Long	Short	Moderate/Long	Moderate	Moderate/Long
Constriction during polymerization	High	High	Low	Low	Low
Adhesion of the resin	Moderate	Moderate	Good	Good	Good
Electric strength feature	Moderate	Good	Good	Good	Moderate/Good
Application	6.6kV	13.8 kV	28 kV	28 kV	28 kV

For what concern the insulation tape choice it must be selected according to the VPI process and the resin. In particular the attention must be focused on the agreement with the resin features and thermal class, the winding handiness, robustness during the application, storage efficiency, etc.

Another important aspect is the impregnation process monitoring. Some electric probes can be fitted inside the autoclave to measure the capacitance between the machine's windings or between the coil terminals and the ground.

This way the impregnation process is monitored as the higher is the capacitance, the higher is the resin content and the insulation thickness. This procedure can be constantly monitored and the data can be compared with insulating system of proved experience to reach the proper insulation thickness. Also the curing process can be monitored measuring the Dissipation Factor ($\tan\delta$) which provides a measure for the dielectric losses within the insulation and so a measure of the humidity level inside the resin and the tapes. Usually it must be lowered at 10% after 2 hour of curing at 150 °C. Also this measure is related to the resin type used.

1.3 STATOR WINDING TESTS

As said before, the previous explanation on the insulation system and impregnation techniques is not exhaustive on all the material present nowadays but just a focus done at the beginning of this research to better understand the possible fault causes in an electrical machine due to repetitive voltage pulses feeding. Along with this topic, the most common testing methods for a stator winding are reviewed and some of them have been applied for the qualification of a 1 MW wind generator windings.

In Table 3 the common tests are listed.

TABLE 3 COMMON STATOR WINDING TEST [6]

Name	Description	Difficulty	Effectiveness
Insulation Resistance (IR)	Apply a DC voltage for 1 minute and measure leakage current	Easy	Contaminations or serious defects
Polarization Index (PI)	$\frac{IR_{1\ min}}{IR_{10\ min}}$	Easy	Contaminations or serious defects

Dc High Potential	Apply High AC voltage for 1 minute	Easy	Contaminations or serious defects
Capacitance	Low or High voltage to measure the winding capacitance to ground	Moderate	Thermal or water leak problems
Dissipation factor	Low or High voltage to measure the winding capacitance to ground	Moderate	Thermal or water leak problems
Power factor tip-up	Differences in insulation loss from high to low voltage	Moderate	Widespread thermal or contamination problems in form windings
Off-line PD	Directly detect PD pulse voltages at rated voltage	Difficult	Find most problems except end-winding vibration
Surge comparison	Apply a voltage surge	Difficult	Find turn insulation problems

One of the most effective tool to find problems in the insulation system is the PD detector because almost every problem like delamination, resin corruption, tape detachment, etc. causes partial discharges. The detection of PD is not an easy task and the instruments are quite delicate. Besides the data analysis requires an expert consultant as the PD level can change due to lot of factors. Nowadays there are very sophisticated software that can help in data reading and fault recognition based on PD detection off-line but also on-line.

One of the recent challenge is to measure and monitor the PD when the voltage feeding comes from a voltage converter like an IGBT or MOSFET inverter.

In the following some comments on this topic based on the standards IEC 60034-18-41 and 60034-18-42 are derived.

The increasing and quite exclusive use of the motor with fast switching drives has introduced in the past years the problem of the motor overvoltage at its terminals as will be better explained later. Voltage at the motor terminals can reach up to two times the DC-Bus voltage level and some studies reporte even more.

Repetitive and steep voltage fronts bring the PD problem also into the field of the low voltage machines previously considered PD-free. In this field the insulation is made of organic enamel and so particularly vulnerable to partial discharges. Moreover this kind of windings are usually not impregnated or treated with resins and so the air-gaps between the coil's turns are massively distributed.

Some standards, as NEMA MG1 part 30-31, suggest a test with step voltage equal to 3.1 times the nominal voltage for low voltage machine (<600 V) or 2.7 times for medium voltage machines (> 600V). It's important to underline that these limits must be held for a small period of time and so the tests don't consider the repetition of the voltage steps when the machine is indeed fed by an inverter.

The standard IEC 60034-18-41 considers this aspect for Type I windings.

First of all, severity categories for the voltage stress to ground are defined based on the overvoltage shoot, that is the ratio of the maximum voltage registered at the motor terminal over the DC-Bus voltage, and on the voltage step rise-time as reported in Table 4.

TABLE 4 SEVERITY CATEGORIES

Category	Overvoltage shoot [Vp/Vdc]	Rise Time t_r [μ s]
Soft	≤ 1.1	≥ 1
Moderate	≤ 1.5	0.3 – 1
Severe	≤ 2.0	0.1 – 0.3
Extreme	< 2.5	0.05 – 0.1

In the classic PD measurement the inception voltage (PDIV = *Partial Discharge Inception Voltage*) it's a fundamental parameter to evaluate the phenomenon and qualify the insulation. In the case of repetitive voltage pulses a little bit different parameter is considered: the RPDIV (= *Repetitive partial discharge inception voltage*) defined as the minimum voltage pulse for which PD can be registered on the major part of the voltage steps when the voltage level is progressively increased starting from zero.

The qualifying test must guarantee that no PD occur in the whole machine's service life. The RPDIV is measured during a typical insulation aging test for determining the machine's thermal class. To be qualified as Type I for inverter feeding the RPDIV measured after every aging cycle must be greater than the voltage as shown in Table 5 for every category. A 30% more is considered for the phase-to-phase voltage. According to the standard IEC 60034-18-41 the detection of PD during every instant of an aging cycle for a Type I system indicates a failure.

Usually the industrial frequency voltage feeding is acceptable only for qualifying a winding sample made of two rolled wires one of which is kept to ground potential.

The repetitive pulses voltage is necessary to test the turn-to-turn voltage strength and the test must be done with a standard coil or the whole winding.

Table 5 shows the minimum RPDIV-peak values for a stator winding with 480 V nominal voltage and 650 V DC-Bus. The values refer to a voltage pulse with very steep front (1.5 μ s) and long tail time as for the common laboratory pulse tester.

TABLE 5 RPDIV VOLTAGE LEVEL EXAMPLE

Minimum RPDIV, 460Vac nominal voltage, 621Vdc-Bus 2 level converter			
Category	K : Overvoltage shoot	Phase-Phase [V] V_{P-P}	Phase-Ground or turn-to-turn [V] V_{P-G}
Soft	1.1	930	651
Moderate	1.5	1267	887
Severe	2.0	1690	1183
Extreme	2.5	2112	1478

where:

$$V_{P-P} = 1.3 \cdot V_{dc} \cdot K \quad (1.5)$$

$$V_{P-G} = 0.7 \cdot V_{P-P} \quad (1.6)$$

The phase-to-phase insulation and the phase-to-ground insulation can be tested separately. In the first case the voltage is applied across two phases with disconnected neutral. In the second case the pulse is applied to one phase with the neutral to ground.

The expression in (1.5) for the phase-to-phase test counts for the overvoltage factor K, as in Table 4, and for a 30% more of safety margin.

The phase-to-ground voltage test level is derived from experimental analysis on the overvoltage on the first coil's turns and a 0.7 coefficient has been adopted on the phase-to-phase voltage test level.

For what concern the acceptance tests is necessary so verify that the stator winding is made according to the project. At least one winding from the production line batch is tested and its RPDIV should be greater than the voltage level indicated for its category. This test has to be performed with a square pulse voltage.

Type II insulating systems, as said before, are built with glass fiber and mica tapes plus resin and are intrinsically resistant to partial discharges. Normally this kind of insulation is used for medium-high voltage machines (> 700 Vrms as indicated in the standard IEC 60034-18-42) and so the inception of partial discharges in the normal operation conditions is expected.

There are two steps for testing the insulation system of Type II. The first is the qualification of the main wall insulation toward the ground and the insulation between the turns. For the main wall insulation, coils or bars are treated with an accelerating aging process to determine the life curve. It's possible to derive the life curve under power converter feeding, basing on the life curve derived under industrial frequency voltage feeding. Separate test are performed for the turn insulation and for the stress grading system. The main wall and turn insulation test can be skipped if PD activity is not expected during the machine's life.

The second step is the acceptance test. Complete coils, made according to the production standards, are subjected to an endurance test at 50 Hz or 60 Hz and the test is performed in accordance between the manufacturer and the client.

- **Qualification Test**

The qualification test described in the IEC 60034-18-42 guarantees the materials, design rules and insulation system construction qualification for a PD resistant system under a determined voltage level. These tests are based on the general procedures for evaluating an insulation system described in the IEC 60034-18-1. According to that standard the insulation subjected to electronic converter voltage feeding (candidate system) is compared to an insulation with proved endurance under industrial frequency voltage or converter feeding voltage (reference system).

For a Type II the main insulation qualification and the turn insulation qualification is performed by an endurance voltage test at room-temperature or at higher temperature (IEC 60034-18-32) and with different overvoltage or frequencies. This way a life-curve can be derived. The mutual aging between the main-wall and turn insulation is not considered.

Basing on the previous considerations, the life-curve under power electronic voltage feeding can be derived from the life-curve taken with sinusoidal feeding. Furthermore the following conditions are assumed:

- a) The aging rate due to the voltage pulse or due to the sinusoidal voltage is the same on equal peak-to-peak voltage and cycle numbers at the nominal frequency
- b) The exponent n for the life span is independent from frequency below 1000 Hz

$$L = cV^{-n} \quad (1.7)$$

with L: insulation system life [hours]

c: constant

V: voltage level

n: life exponent

The qualification of the conductive or semi-conductive layer is performed by a separate aging test. A sample of an impregnated coil in the slot is tested with an impulsive voltage similar to that expected in service for a period of time adequate to visibly evaluate the inception of worsening, discoloration and material damages.

- o *Main wall Insulation*

The main-wall insulation is more subjected to the fundamental frequency voltage (50Hz/60Hz) and the important parameter is the peak-to-peak voltage stress. The life-curve can be derived if at least three voltage levels are chosen for the test. The test is successfully passed if the average life of the candidate system is similar to the proven system at the same voltage level.

The life reduction due to the high frequency can be evaluated thanks to the following equation:

$$L_2 = \left(\frac{f_1}{f_2} \right) L_1 \quad (1.8)$$

with: L_2 : life span at frequency f_2

f_1 : industrial frequency (50Hz/60Hz)

f_2 : high frequency for life evaluation.

L_1 : life span at frequency f_1

Normally 5 coils or 10 bars are tested for every voltage level.

- o *Turn insulation*

The turn insulation is particularly stressed by the repetitive voltage pulses, by the overvoltage at the motor terminals and by the rise-time of the voltage steps.

The turn insulation test could not be necessary where the voltage converter produces voltage steps with long rise-time ($t \geq 500$ ns). In this case the voltage distribution inside the winding is more regular and also the overvoltage is moderate. (Table 4).

The test is similar to that of the main-wall insulation with a candidate system and a proven system to be compared.

Two copper bars with tape and resin can be placed side by side as in a real coil representing two turns in order to build a test specimen.

The test voltage (U_{turn}) is equal to the maximum peak-to-peak voltage expected between turns during normal service plus a safety factor. This factor can be given by the manufacturer according with the design criteria.

The voltage U_{turn} is applied across the two conductor for 60 s at 50/60 Hz and if no PD are detected, the qualification test can be skipped. On the contrary if PD are detected the specimen must be tested with repetitive voltage pulses or with sinusoidal voltage at the converter frequency until the insulation break down.

The standard suggest the use of at least 5 samples with a test voltage equal to $4.5U_{turn}$, $4.0U_{turn}$ e $3.5U_{turn}$ for each. Once the time to failure (t_F) for every voltage level and for every sample is obtained, a voltage curve as a function of t_F can be derived. This curve, compared with the same obtained for the main-wall insulation, has to be of the same quality or superior.

- *Semi-conductive grading tape (Corona effect protection)*

This kind of protection is placed at the coil exit in correspondence to the slot end to prevent partial discharges due to the electric field enhancement in this region. This tape is particularly sensitive to the voltage converter feeding because high losses are created by the high frequency and concentrated in the grading tape [4].

The qualification test for the grading tape is complicated due to the high frequency sensitivity. Samples representing the winding are subjected to an aging test with pulse voltage and at least 100 hours of life are required. The voltage level is equal to 1.3 times the peak-to-peak voltage level in normal operating condition. The test has to be performed with two different temperatures: room-temperature and in-service temperature. The hot spot must be checked with an infra-red camera and PD with a ultraviolet sensitive camera. During the 100 hours every sample must stand the voltage without visible discharge and without overheating above the thermal class.

- **Acceptance Test**

Type II insulating systems are subjected to accelerated aging tests at 50 Hz or 60 Hz sinusoidal voltage with a peak-to-peak voltage of 4.3 times the maximum peak-to-peak phase-ground voltage during the converter feeding. The 4.3 coefficient corresponds to a life exponent (n) equal to 10.

This test refers to the main-wall insulation and can be too severe for the stress grading material so if damages occur, its remedial is allowed. After 250 h of test, no sample should be damaged in order to consider the test passed.

This concludes the first part in which the most commonly used insulation systems are described together with their main features and manufacturing techniques.

The standards also describe the tests on the insulation subjected to repetitive voltage pulse voltage feeding. This topic is still growing as the power electronics technology improves and new maintenance data are being collected from in-service machine in the last few years which can help in the definition of the most proper test to perform to qualify an insulation system with non-sinusoidal voltage feeding.

REFERENCES

- [1] CEI, IEC Technical Specification TS 60034-18-41, *Rotating electrical machines - Part 18-41: Qualification and type tests for Type I electrical insulation systems used in rotating electrical machines fed from voltage converters.*
- [2] CEI, IEC Technical Specification TS 60034-18-42, *Rotating electrical machines - Part 18-42: Qualification and acceptance tests for partial discharge resistant electrical insulation systems (Type II) used in rotating electrical machines fed from voltage converters.*
- [3] CEI, IEC Technical Specification TS 60034-18-32, *Rotating electrical machines - Part 18-32: Functional evaluation of insulation systems - Test procedures for form-wound windings - Evaluation by electrical endurance.*
- [4] Stranges, M.K.W.; Stone, G.C.; Bogh, D.L.; , "Progress on IEC 60034-18-42 for Qualification of Stator Insulation for Medium-Voltage Inverter Duty Applications," *Petroleum and Chemical Industry Technical Conference, 2007. PCIC '07. IEEE* , vol., no., pp.1-7, 17-19 Sept. 2007.
- [5] 2012 Von Roll Holding AG.
- [6] Boulter, E., Culbert, I., Dhirani, H., Stone, G., *Electrical Insulation For Rotating machines – design, Evaluation, Aging, testing and Repair*, Wiley-IEEE Press, 2004

2 MOTOR OVERVOLTAGE ANALYSIS IN PWM AC DRIVES USING A UNIVERSAL MODEL

This second chapter deals with the analysis of the overvoltage at the motor terminals when the voltage wave is made of repetitive square pulses due to the inverter feeding.

As said before this topic has been well described in literature since the first fast switching devices started to be widespread in the market. The combination, as will be explained later, of very fast switching plus long cable can lead to overvoltage at the motor terminals as high as two times the DC-Bus voltage level (but some authors refers even more [6]). This phenomenon leads to high insulation stress in the first turns of the winding and a proper action must be taken to contrast it. The passive action possible is to enforce the insulation in the first machine's coil and the disadvantage of this solution will be shown in the third chapter. Thanks to the standards, the voltage test level can be computed and the correct insulation system can be tested. The active action possible is the use of filters to reduce the overvoltage level at the machine's terminals. A complete motor model for overvoltage prediction will be explained in this section considering a fast switching square voltage excitation, long cable and high frequency motor parameters. With the help of high frequency measurements made by the author on a 1.1kW induction motor, an accurate simulation with Matlab Simulink®, based on differential mode analysis, is made. The simulation results are validated through comparison with measured values. The model response shows realistic results for the determination of the filter parameters among different values of rise time and cable length. This work has been presented in the XIX International Conference on Electrical Machines [1].

2.1 OVERVOLTAGE EFFECTS

When AC rotating machines are fed by inverters based on insulated gate bipolar transistor (IGBT) technology, high frequency switching pulses feed the machine. As reported in [2] this square wave pulses can have a very small rise time t_r , that is the time to get from 0 V to the DC voltage level for every pulse as shown in an example of Figure 2.1 for a rise time of $0.1\mu\text{s}$.

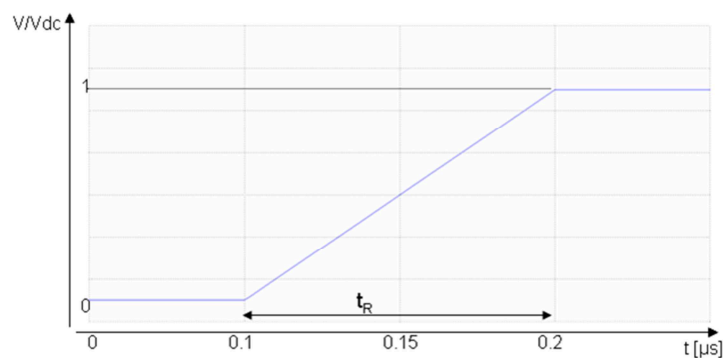


FIGURE 2.1 VOLTAGE RISE TIME

If this electrical stress is long-lasting and of a suitable high value, it drastically accelerates the aging of the insulation, with the consequence of partial discharges and destructive effects on windings, causing out-of-service for the rotating machine and increasing the cost of the operations [3].

Figure 2.2 shows the model components that have been selected in order to realize an effective simulation model. The inverter model for the simulation allows the control of the rise time, in order to see the response of

the system in different situations. The high frequency parameters of the three phase cable model are computed from LCR meter measurement [4].

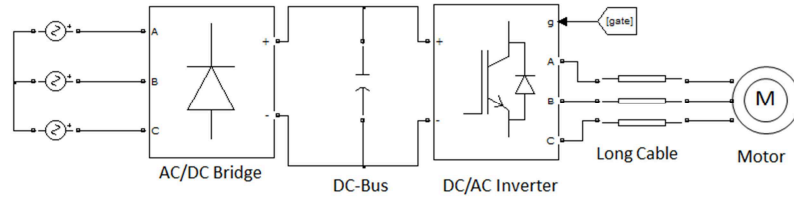


FIGURE 2.2 COMPLETE SYSTEM FOR THE ANALYSIS OF OVERVOLTAGE

Now, considering the situation described above, the origin of the overvoltage is briefly explained. Every transmission wave which runs along the electrical line is subjected to the propagation law. This is described by the following differential equation with the ideality of no-loss line:

$$\frac{1}{LoCo} \frac{\partial^2 u}{\partial x^2} = \frac{\partial^2 u}{\partial t^2} \quad (2.1)$$

where t is the time, x the distance and Lo [H/m] and Co [F/m] the line parameter per unit length.

The solution of the equation is the following expression:

$$u(x,t) = u^+ \left(t - \frac{x}{v} \right) + u^- \left(t + \frac{x}{v} \right) \quad (2.2)$$

where u^+ and u^- represent the transmission waves that propagate in the positive- x direction and negative- x direction respectively.

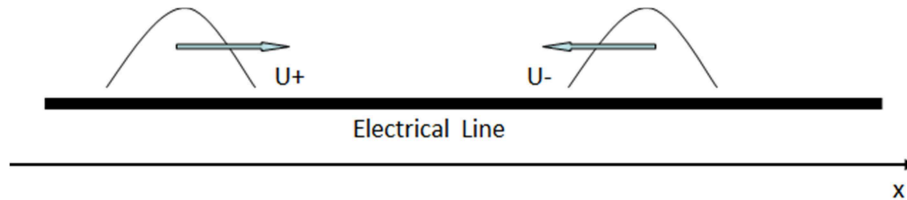


FIGURE 2.3 WAVE PROPAGATION ALONG THE LINE

For every time instant the voltage in every x -point of the line is given by the sum of two waves travelling in the opposite direction.

The propagation speed of the waves is:

$$v = \frac{1}{\sqrt{LoCo}} \quad [\text{m/s}] \quad (2.3)$$

and it's lower than the light speed because it travels in a wire with dielectric permittivity and magnetic permeability different from that of the free space.

Remembering the no-loss hypothesis, the line impedance can be defined as:

$$Z_C = \sqrt{\frac{L_o}{C_o}} \quad [\Omega] \quad (2.4)$$

and it's called the line characteristic impedance which is independent from the line length.

The square wave generated by an inverter can have a very short rise time (t_R) and it can be shorter than the transmission time (t_T). In this case, the voltage reaches the full DC-Bus voltage level before reaching the end of the line where the motor is connected.

As the wave reaches the motor, it faces a different impedance as the motor has a completely different structure in comparison with the line and that means a much higher inductance. So the characteristic impedance of the motor is usually 10 to 100 times the cable impedance [5].

At the end of the line the direct wave is reflected according to the reflection coefficient defined as:

$$\Gamma_L = \frac{Z_L - Z_C}{Z_L + Z_C} \quad (2.5)$$

where Z_L is the load impedance and Z_C is the cable impedance. So if the load has a very high impedance in comparison with the cable, $Z_L = \infty$ can be assumed and so $\Gamma_L = 1$. This means that all the direct voltage wave is reflected and, at the load terminal, the voltage amplitude is equal to the sum of the direct voltage plus the inverse voltage wave which arises the voltage at the load at two times the DC-Bus voltage level. Obviously the hypothesis of infinite impedance is true only for open-end line; that's not the case of the motor connection but is used to explain the voltage stress level limit that can be faced.

This situation occurs every time a voltage square pulse is produced by the inverter with a very severe rise time; so the following stands for the reflected wave voltage level V_R :

$$V_R(t_T) = V_{dc} \cdot \Gamma_L \quad \text{for } t_T \geq t_R \quad (2.6)$$

and

$$V_R(t_T) = \frac{t_T \cdot V_{dc} \cdot \Gamma_L}{t_R} \quad \text{for } t_T < t_R \quad (2.7)$$

respectively if the transmission time is greater than the rise time or if the transmission time is smaller than the transmission time. In this case, the reflected voltage amplitude is only a part of the Dc-Bus voltage weighted for the ratio of the transmission time over the rise time. [5]

2.2 SYSTEM PARAMETERS COMPUTATION AND FILTER DESIGN

In this section the parameters computation and the measuring techniques for the system model construction are described. The goal is to find a complete model for the power system simulation which comprehend the variable rise time inverter, the connection cable and the induction motor model. The use of a filter to reduce the overvoltage is also considered.

The motor-terminal filter has the goal of matching the motor impedance with the cable impedance so that the reflection coefficient and so the reflection voltage waves are drastically reduced and no overvoltage occurs.

From high frequency analysis on the cable, it is possible to define the parameters of the filter: in this case an RC first order filter is used to reduce the reflected wave. This is a Line Termination Network (LTN) RC filter designed to match the surge impedance between the rotating machine and the cable as shown in Figure 2.4. A design methodology to establish, in different situations, the optimum value of the resistance and the capacitance is presented in [5], [6], [7]. The cable length and the rise time will be changed to deeply investigate the overvoltage and the transients that will occur in presence or absence of the LTN RC filter.

The model of the rotating machine is comprehensive of low to high frequency effects and is constructed considering differential and common mode electric parameters. The analysis on the impedance frequency response in a wide range of frequencies is performed to obtain the motor model parameters from few peculiar values [8], [9]. In this work a 1.1kW four poles AC induction motor is analyzed to obtain the measurements of impedance and phase in order to build the model for the simulation.

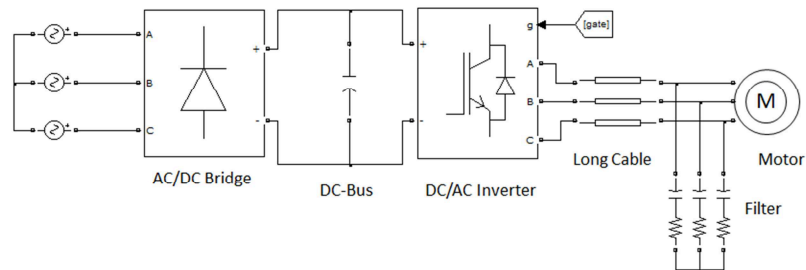


FIGURE 2.4 SYSTEM WITH LTN RC FIRST ORDER FILTER

Hereafter the design considerations for the components involved in the configuration shown in Figure 2.4 are presented.

- **Three Phase Cable for PWM AC Drives**

For the cable model the distributed parameters three phase line of SimPowerSystems Simulink® toolbox has been used for the simulation. This model is composed by a 3-phase distributed LC parameter line with lumped losses. According to [4] the model has a good high frequency response. This is very important for investigating the high frequency phenomena coming from the square wave voltage feeding. In order to obtain the R, L and C matrix for the model computation, the following measures were performed with a LRC Meter:

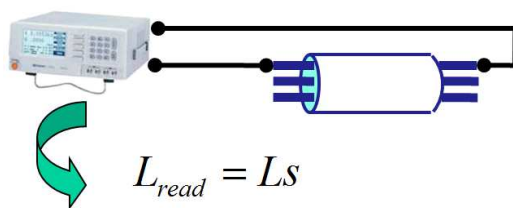


FIGURE 2.5 AUTO-INDUCTANCE MEASURE

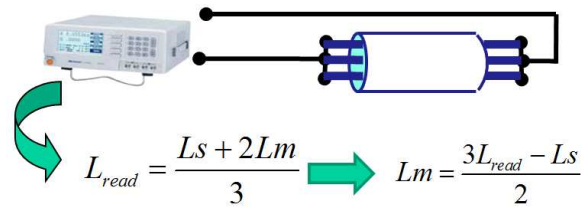


FIGURE 2.6 MUTUAL-INDUCTANCE MEASURE

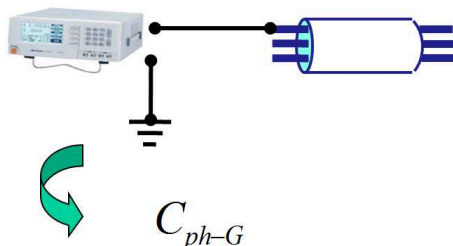


FIGURE 2.7 CAPACITANCE TO GROUND MEASURE

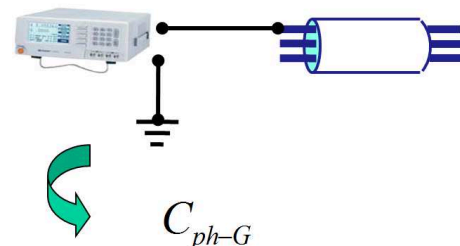


FIGURE 2.8 CAPACITANCE PHASE-PHASE MEASURE

For the auto and mutual inductance the connection scheme of Figure 2.5 and Figure 2.6 show the measurement connection while for the capacitance to ground and the phase-to-phase capacitance the

connections to the meter are shown in Figure 2.7 and Figure 2.8 respectively. Measurements on an 11AWG 4-conductors-PVC, 7.7m long cable, lead to the following matrices.

$$R = \begin{bmatrix} 17.8 & 0 & 0 \\ 0 & 17.8 & 0 \\ 0 & 0 & 17.8 \end{bmatrix} [m\Omega/m]$$

$$L = \begin{bmatrix} 909 & 552 & 552 \\ 552 & 909 & 552 \\ 552 & 552 & 909 \end{bmatrix} [nH/m]$$

$$C = \begin{bmatrix} 94.3 & -10.4 & -10.4 \\ -10.4 & 94.3 & -10.4 \\ -10.4 & -10.4 & 94.3 \end{bmatrix} [pF/m]$$

The resistance matrix is only composed by the series resistances of the three cable's wires. The inductance matrix has on the main diagonal the self-inductances and the other elements are the mutual-inductances between the phases.

The capacitance matrix has on the main diagonal the sum of three capacitances: the two between the phase and the other two phases, and the one between the phase and the ground. The mutual terms are the capacitance between the phases with negative sign.

- First Order RC Filter at Motor Terminals.

The RC filter is connected to the motor terminals in a Y connection as shown in Figure 2.4. According to the approach proposed by [5]-[7], the filter resistance has to match the surge impedance of the cable.

$$R_f = Z_1 \quad (2.8)$$

where the surge impedance of the cable is defined, at high frequency, by:

$$Z_1 = \sqrt{\frac{L_1}{C_1}} = \sqrt{\frac{(909 - 552)nH}{(94.3 + 10.4)pF}} = 58\Omega \quad (2.9)$$

As the motor surge impedance is greater than Z_1 , as reported in [5]-[7] and [10], a parallel connected RC filter balances the motor impedance. The equivalent impedance, called Z_{eq} , given by the motor impedance in parallel with the filter impedance, should be equal to the cable one. When the cable surge impedance Z_1 is equal to Z_{eq} , the reflection coefficient defined in (2.10) is zero.

$$\Gamma = \frac{Z_{eq} - Z_1}{Z_{eq} + Z_1} = 0 \quad (2.10)$$

As a consequence, the reflecting wave generated at the motor terminals which causes the overvoltage, is suppressed.

To determine the value of the filter capacitance, the rise time of the inverter voltage pulse should be known. At the very first time the filter acts like a pure resistor because the capacitor is uncharged. After the rise time, the capacitor is fully charged acting like an open circuit and avoiding power dissipation. In [7] a simple RC charge equation is proposed considering a capacitor voltage value (V_{cx}) equal to 10% of the dc voltage (V_{bus}). It leads to the following equation:

$$V_{cx} = (0.10)V_{bus} = V_{bus}(1 - e^{-t_{rise}/(R_f C_f)}) \quad (2.11)$$

and from (2.11):

$$C_f = \frac{Trise}{0.1054 * Rf} \quad (2.12)$$

With a typical inverter voltage rise time of 100ns, the capacitance turns out to be 16 nF.

- **Model of the AC Rotating Machine**

The construction of a good electric model for an induction motor has been widely developed for normal sinusoidal voltage feeding and transient conditions. When the motor is fed through a power IGBT converter, the voltage is no more sinusoidal but it's made of rectangular pulses with rising rate in the order of kV/ μ s. With this wave shape feeding the motor, a lot of high order harmonic voltage components are introduced in the power line. The capacitive elements coupling the stator windings, the frame and the rotor are not irrelevant in this case since the voltage feeding the winding has a very short rise time. Other studies related these phenomena to the shaft voltage and capacitive couplings in a motor structure, as presented in [13].

This model is built using some LCR bridge measurements in Differential Mode (DM). DM measurements are made with two motor phase terminals linked together to form one connector to the LCR bridge and the other phase terminal as the second connector as shown in Figure 2.9. The motor is put on an insulating layer to achieve good data precision.

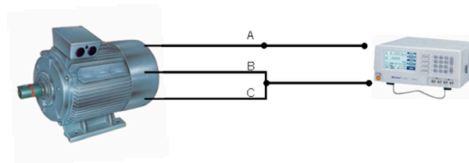


FIGURE 2.9 LRC BRIDGE AND AC ROTATING MACHINE DIFFERENTIAL MODE CONNECTION (DM)

With this configuration, it is possible to obtain the differential mode frequency response of the motor. In Figure 2.10 the measured data from a 1.1kW induction motor are presented. The range of frequency must be wide enough to include the low, medium and high frequency response of the motor. The range considered is 50Hz – 20MHz.

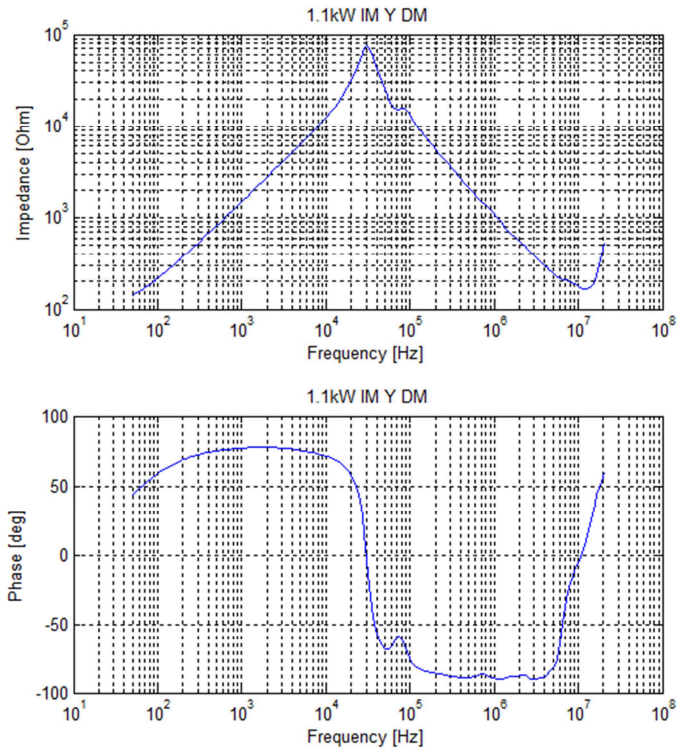


FIGURE 2.10 PLOT FROM MEASURED DATA ON A 1.1 KW INDUCTION MOTOR.

From the impedance and phase vs. frequency response of Figure 2.10, some particular values are derived to construct the motor model. These values are listed below.

Absolute impedance value and the frequency at which the phase reaches its maximum value:

$$|Z(f(\varphi_{Max}))|; f(\varphi_{Max}) \quad (2.13)$$

Absolute impedance value and the frequency at the maximum impedance point (called resonance point)

$$|Z|_{MAX}; f_r \quad (2.14)$$

Absolute impedance value and the frequency at the minimum point placed in the high-frequency area (called anti-resonance point)

$$|Z(f_a)|; f_a \quad (2.15)$$

Absolute impedance measured in DC:

$$|Z(f_{DC})| \quad (2.16)$$

From LCR Bridge measurements between one phase of the motor in Y connection and the motor frame as the second probe, the following can be obtained:

Winding to frame capacitance at high frequency ($f = 1\text{MHz}$):

$$C_{sf,HF} \quad (2.17)$$

Winding to frame capacitance at low frequency ($f = 1\text{kHz}$):

$$C_{sf,LF} \quad (2.18)$$

The complete motor model is presented in Figure 2.14. It's a three phase circuit and for every phase the classical low frequency parameters model of an induction motor can be distinguished. In addition to these, there are other parameters which model the high frequency phenomena of the leakage inductance and the capacitive coupling between the winding's turns and toward the motor frame and the ground. The equations

that allow to find the complete model parameters are explained below. Some remarks have to be done as reported in [8].

Thus, basing on the measures with a LCR bridge as explained in (2.13)-(2.18), the motor model parameters are derived.

As the DM measure sets two phases in parallel and then in series with the third phase, the amplitude values are scaled by a factor of 2/3. So, from the measurement (2.16), the series resistance can be obtained as follows:

$$R_s = \frac{2}{3} |Z(f_{DC})| \quad (2.19)$$

and the rotor resistance in the model is considered equal to the stator one:

$$R_r = R_s \quad (2.20)$$

At the maximum phase angle point, only the series resistors and inductors are relevant and so the equivalent circuit of Figure 2.11 is analyzed for each phase.

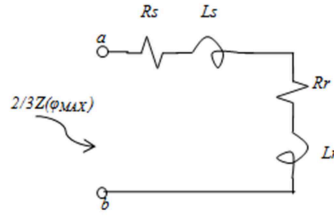


FIGURE 2.11 EQUIVALENT CIRCUIT IN THE MAXIMUM POINT OF THE PHASE ANGLE RESPONSE

Considering that the rotor resistance and the rotor leakage inductance are equal to the stator ones and analyzing the equivalent circuit of Figure 2.11, the following relation can be obtained:

$$L_s = L_r = \frac{\sqrt{\left| \frac{2}{3} \cdot Z(f(\varphi_{Max})) \right|^2 - (2R_s)^2}}{4 \pi \cdot f(\varphi_{Max})} \quad (2.21)$$

The inter-turn equivalent capacitance of the stator winding is derived looking at the main resonance frequency of the complete model. As explained in [9] an expression both for high frequencies and for low frequencies can be obtained using the data (2.17), (2.18) and considering the motor Y connected.

$$C_{sw,HF} = \frac{2\omega_r^2 L_s C_{sf,HF} - 1}{\omega_r^2 L_s (\omega_r^2 L_s C_{sf,HF} - 1)} \quad (2.22)$$

$$C_{sw,LF} = \frac{2\omega_r^2 L_s C_{sf,LF} - 1}{\omega_r^2 L_s (\omega_r^2 L_s C_{sf,LF} - 1)} \quad (2.23)$$

A mean value is then considered for the machine's model construction:

$$C_{sw} = \frac{C_{sw,HF} + C_{sw,LF}}{2} \quad (2.24)$$

This is the expression of the inter-turn capacitance as used in the complete model of Figure 2.14.

The capacitance of the parallel branch stands for the capacitive coupling between the stator and the frame at high frequency; it's simply the value measured as in (2.17) and so:

$$C_{sf} = C_{sf,HF} \quad (2.25)$$

The resistor of the parallel branch stands for the minimum impedance measured at the anti-resonance point. Thus it is derived from the measure (2.15) as follows:

$$R_{sf} = \frac{2}{3} |Z(fa)| \quad (2.26)$$

The series inductance ηL_{1s} , stands for the leakage inductance of the first winding turns.

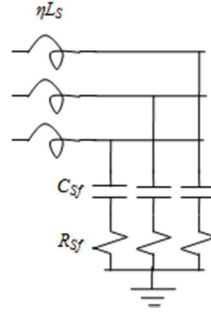


FIGURE 2.12 EQUIVALENT CIRCUIT IN THE ANTI-RESONANCE POINT

It is derived considering that, because of the high frequency coupling with the ground, in the anti-resonance point the winding has the equivalent circuit of Figure 2.12. and so the amplitude of the impedance value is only due to the series resistors R_{sf} and so:

$$\eta L_s = \frac{1}{C_{sf,HF} * (2\pi fa)^2} \quad (2.27)$$

The value R_{sw} accounts for the maximum impedance value (resonance point). It is estimated starting from the DM measurement (2.14) and then subtracting the parallel of the iron losses resistance with the rotor leakage inductance. Thus obtaining:

$$R_{sw} = \frac{2}{3} |Z|_{Max} - |R_{core} // (j2\pi fr L_r)| \quad (2.28)$$

The neutral point coupling to ground accounts for the total stator-to-frame capacitance at low frequencies. This value is computed as follows:

$$C_{sf,0} = C_{sf,LF} - 3C_{sf,HF} \quad (2.29)$$

- Measurements Results

The author performed the measurements according to DM connection to a 1.1kW 50Hz, 380V four poles induction motor in a Y connection as shown in Fig. 7, with a Newtons4th LtdPSM1735 Frequency Response Analyzer [12]. From this measurement all the data reported in (2.13)-(2.18) were derived in order to use the relations (2.19)-(2.29) to obtain the model parameters reported in Table 6.



FIGURE 2.13 MEASUREMENT WITH LRC BRIDGE ON 1.1KW AC INDUCTION MOTOR.

TABLE 6 PARAMETERS OF THE MOTOR MODEL

Parameter	Value
$R_r = R_s(\Omega)$	7.6
$L_s = L_r(mH)$	75.09
$C_{sw}(pF)$	494.2
$C_{sf}(pF)$	176.3
$R_{sf}(\Omega)$	109
$\eta L_s(\mu H)$	1.01
$R_{sw}(k\Omega)$	47.19
$C_{sf,0}(pF)$	259.9

The value of R_{core} for the iron losses and of L_m for the magnetizing inductance can be obtained from the machine constructor, and those from the 1.1kW motor analysed by the authors are reported in Table 7.

TABLE 7 PARAMETERS FROM THE MANUFACTURER DATA

Parameter	Value
$L_m(mH)$	350
$R_{core}(\Omega)$	2500

2.3 SIMULATION RESULTS AND MODEL VALIDATION

The Matlab Simulink[®] model of Figure 2.15 includes the PWM inverter with adjustable voltage rise time, the distributed line cable model based on data reported above, the three-phase induction motor model proposed of Figure 2.14 and the RC filter.

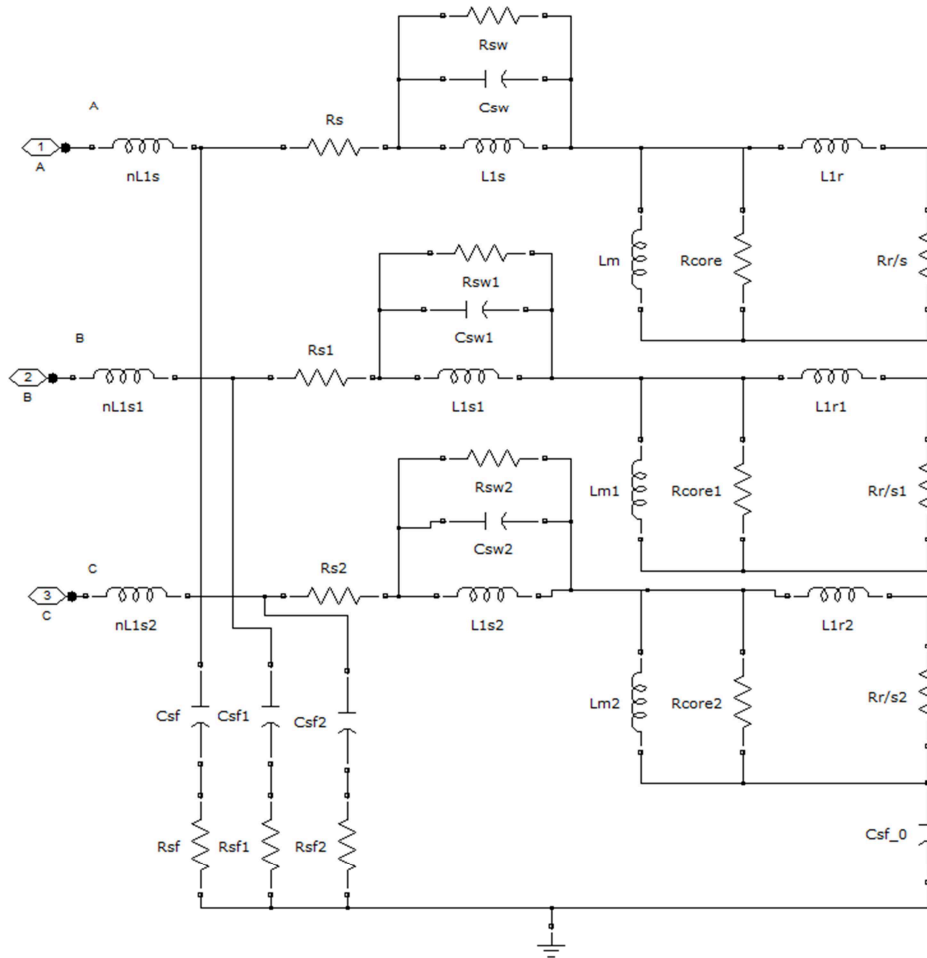


FIGURE 2.14 THREE PHASE MOTOR MODEL

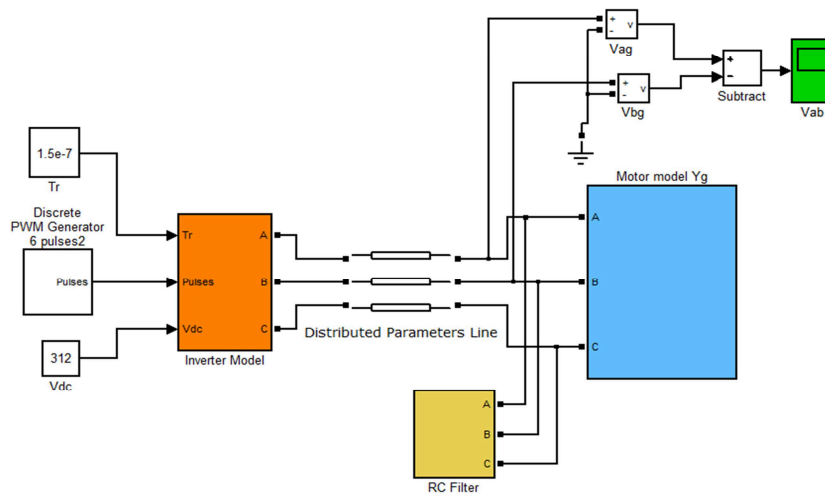


FIGURE 2.15 MATLAB-SIMULINK® MODEL OF THE SYSTEM

In the simulation, the line-to-line voltage at the motor terminals is computed and the influence of the rise time t_r , the cable length l_c and filter application is investigated. The DC-bus voltage is 312V and the switching frequency is 1080Hz. The simulation runs for 0.01s in order to have several pulses from the PWM inverter.

The filter used by the authors, designed by (2.9) and (2.12), has fixed parameters in order to evaluate the effectiveness of a single filter.

- **Case $t_r=0.1\mu s$, $l_c=10m$, Without Filter**

The line-to-line voltage at the motor terminals is shown in Figure 2.16. The overvoltage on the line is due to the reflection effect caused by the very short rise time of the square voltage imposed by the inverter.

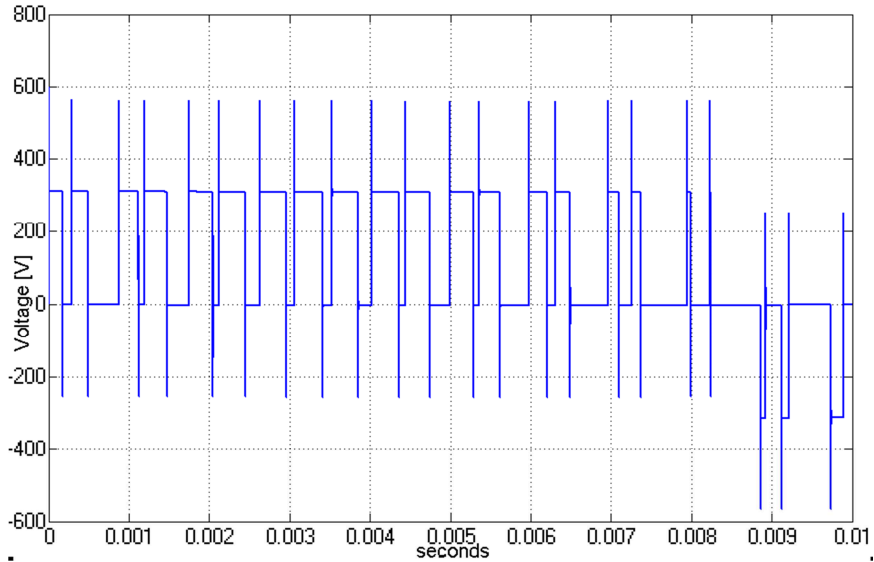


FIGURE 2.16 CASE A LINE-TO-LINE VOLTAGE WITH $t_r = 0.1 \mu s$; $l_c = 10m$; WITHOUT FILTER

An insight look at one of the voltage peaks is given in Figure 2.17. The peak value reaches 563V which means an overvoltage factor $k = 563/312 = 1.8$.

Thus the voltage is the 1.80 times higher compared to the DC-bus voltage.

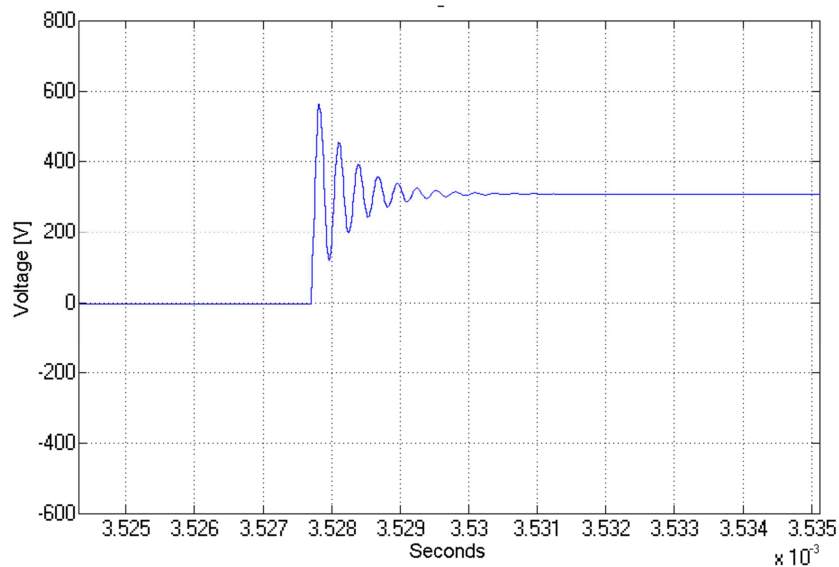


FIGURE 2.17 OVERVOLTAGE ZOOM

- Case $t_r=0.1 \mu s$, $l_c =10m$, With Filter

The effectiveness of the RC motor terminal filter is shown in Figure 2.18 where the same simulation is performed with the filter connected at the motor terminals.

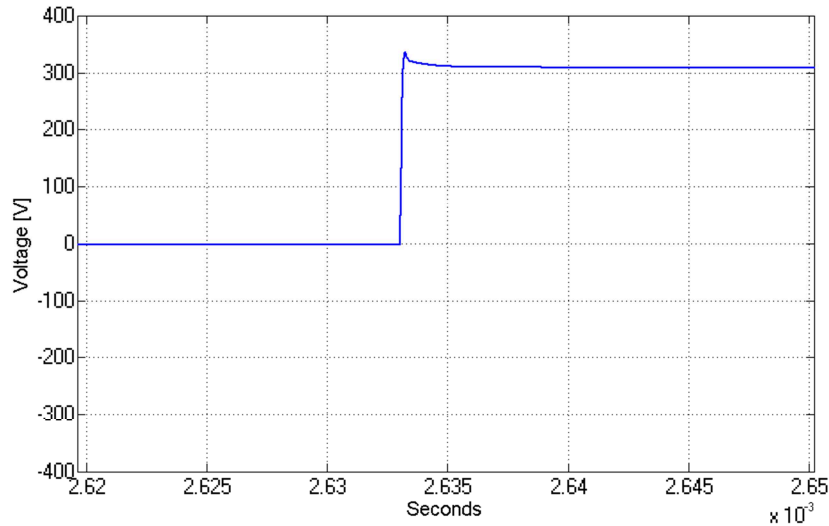


FIGURE 2.18 LINE-TO-LINE VOLTAGE ZOOM WITH $t_r = 0.1\mu s$; $l_c = 10m$; WITH FILTER

With the same cable length and the same rise time, the overvoltage is strongly reduced. In this case the voltage peak reaches only 337V that means $k = 337/312 = 1.08$. The voltage oscillation is no more present meaning a great voltage stress reduction for the machine's winding. The increasing of the voltage rise time at the inverter output is expected to reduce the overvoltage at the motor terminals, as the steep front of the voltage becomes less "severe" [5], [10], [11]. This increment of the rise time is just to demonstrate the reduction of the overvoltage in the simulation, but does not mean practical intervention on the IGBTs gate resistance. Anyway the possibility to change the rise time allows to take account for different types of inverters and their features. In Table 8 other results from the simulation without the filter, for different rise time, are presented.

TABLE 8 OVERVOLTAGE FACTOR FOR DIFFERENT RISE TIME

t_r [μs]	0,1	0,2	0,4	0,7	1	1,5
$k = \frac{V_{overvoltage}}{V_{DC}}$	1.8	1.38	1.18	1.10	1.06	1.04

Now the effect of different cable lengths is investigated. As reported in all the studies concerning motor overvoltage from PWM feeding [5], [10], [11], the longer the cable, the nearer the overvoltage is to $2 \cdot V_{DC,bus}$ value. Other overvoltage factors for different cable lengths are presented in Table 9 with $t_r = 0.1\mu s$ and without the filter.

TABLE 9 OVERVOLTAGE FACTOR FOR DIFFERENT CABLE LENGTH

l_c [m]	5	10	15	20	30	40
$k = \frac{V_{\text{overvoltage}}}{V_{DC}}$	1,39	1,8	1,92	1.94	1.94	1.94

As expected, from 15 meters and over, the overvoltage factor is near to 2. The influence of both the rise time and the cable length is clearly shown in Figure 2.19.

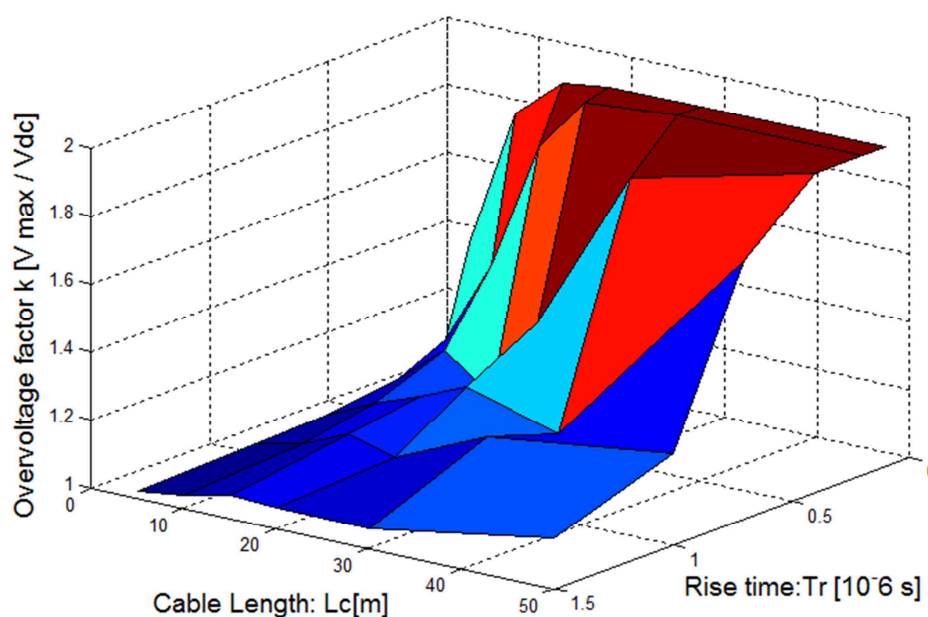


FIGURE 2.19 OVERVOLTAGE FACTOR AS A FUNCTION OF CABLE LENGTH AND RISE TIME

As the length of the cable increases beyond 15 meters and the rise time decreases under $0.4\mu\text{s}$, the overvoltage factor nearly reaches 2. The voltage almost double the DC-bus voltage, stressing the electrical insulation system of the machine every time a pulse occurs, and possibly causing severe damages to it.

To validate the construction of the Universal Motor model, experimental measurement has been derived and the comparison between the experimental data and the simulation data is presented. The induction motor is the one previously described. The cable is the 4-conductors PVC Flexible, 7.7m long described before and the inverter is the TOPVERT E1 manufactured by TOPTEK ELECTRONICS CORP. The measured impulse rise time tr at the inverter terminals is 150ns and the DC-Bus voltage is 312V. A simulation of the model with $tr = 150\text{ ns}$, $l_c = 7.7\text{m}$ and the proposed motor model is performed in order to compare the simulated results with the experimental one in the same condition.

The simulated and the experimental voltage measurements are presented in Figure 2.20 and Figure 2.21 respectively:

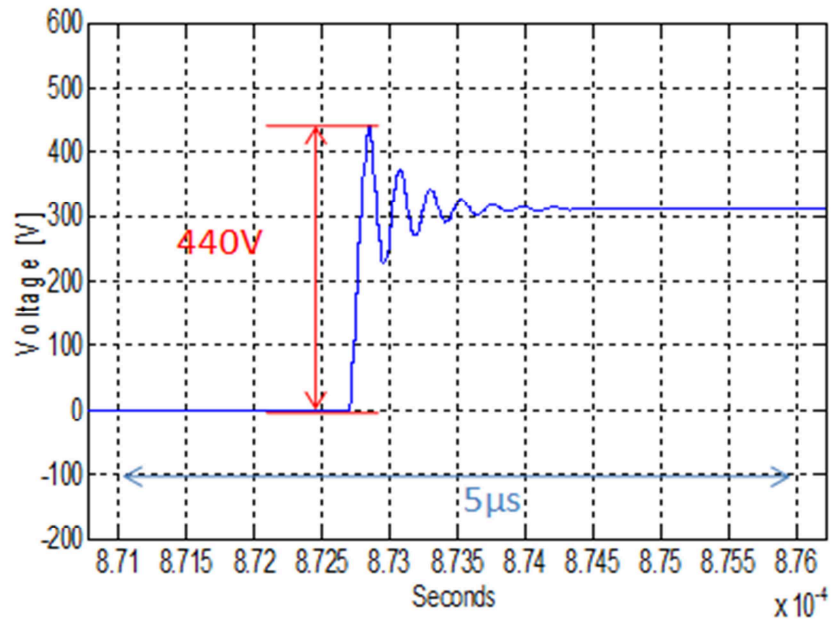


FIGURE 2.20 OVERVOLTAGE FROM SIMULATION

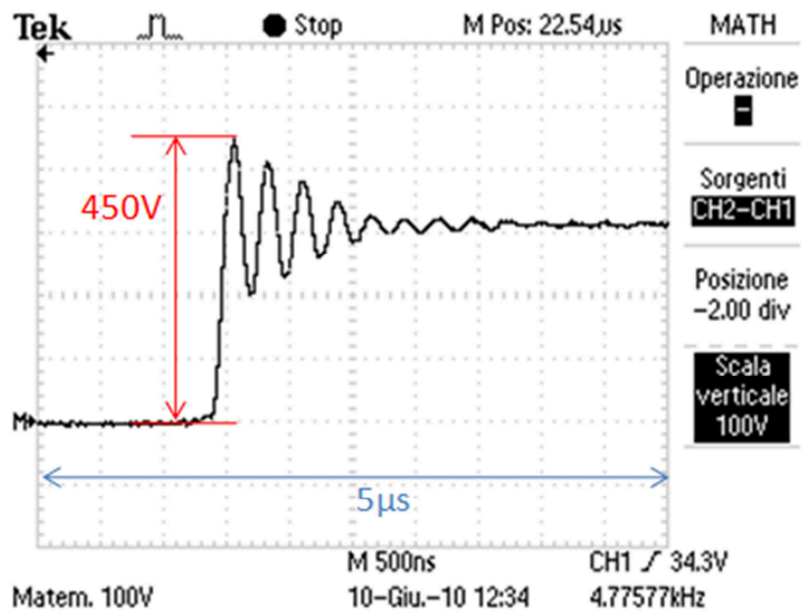


FIGURE 2.21 OVERVOLTAGE FROM MOTOR MEASUREMENT

As the measurements made on the cable and on the motor have to deal with high frequency phenomena, there are some differences in the attenuation of the two curves. The stray capacitances and leakage inductances are very difficult to model precisely and slight different values can lead to remarkable different response. Beyond this consideration, the two curves match quite well meaning that the motor model as well as the cable model well represent the physical system. The measured overvoltage is 450V and the simulated one is 440V, thus only the 2.2% less.

In conclusion the results obtained from the simulation of a power system composed by an inverter model, cable model, RC filter and motor model are presented. The results well respect the previous analysis made on

similar systems concerning the variation of overvoltage at motor terminals as a function of the cable length and of the voltage rise time at the inverter output. It means that the induction motor model applied in a simulation environment of a power system gives good results and can be used for overvoltage prediction and filter dimensioning of a given system.

The motor model is built not only from circuit analysis, but also from impedance measurements to best match the experimental data with the model response. This fact guarantees the reliability of the model results. The validation of the motor model is also presented through the comparison between simulated and measured voltage response in the same condition. Data has been valuated to be in good agreement meaning that the motor and the cable model presented, together constitute a realistic response of an inverter-fed induction motor.

REFERENCES

- [1] Castelli-Dezza, F.; Maglio, M.M.; Marchegiani, G.; Ortega, D.F.; Rosati, D.; , "Reduction of motor overvoltage fed by PWM AC drives using a universal model," *Electrical Machines (ICEM), 2010 XIX International Conference on* , vol., no., pp.1-6, 6-8 Sept. 2010.
- [2] Leggate, D.; Pankau, J.; Schlegel, D.W.; Kerkman, R.J.; Skibinski, G.L.; , "Reflected waves and their associated current [in IGBT VSIs]," *Industry Applications, IEEE Transactions on* , vol.35, no.6, pp.1383-1392, Nov/Dec 1999.
- [3] Cavallini, A.; Fabiani, D.; Montanari, G.C.; , "A novel method to diagnose PWM-fed induction motors," *Dielectrics and Electrical Insulation, IEEE Transactions on* , vol.15, no.5, pp.1313-1321, October 2008.
- [4] Skibinski, G.; Tallam, R.; Reese, R.; Buchholz, B.; Lukaszewski, R.; , "Common Mode and Differential Mode Analysis of Three Phase Cables for PWM AC Drives," *Industry Applications Conference, 2006. 41st IAS Annual Meeting. Conference Record of the 2006 IEEE* , vol.2, no., pp.880-888, 8-12 Oct. 2006.
- [5] von Jouanne, A.; Enjeti, P.N.; , "Design considerations for an inverter output filter to mitigate the effects of long motor leads in ASD applications," *Industry Applications, IEEE Transactions on* , vol.33, no.5, pp.1138-1145, Sep/Oct 1997.
- [6] Moreira, A.F.; Lipo, T.A.; Venkataramanan, G.; Bernet, S.; , "High-frequency modeling for cable and induction motor overvoltage studies in long cable drives," *Industry Applications, IEEE Transactions on* , vol.38, no.5, pp. 1297- 1306, Sep/Oct 2002.
- [7] Skibinski, G.; , "Design methodology of a cable terminator to reduce reflected voltage on AC motors," *Industry Applications Conference, 1996. Thirty-First IAS Annual Meeting, IAS '96., Conference Record of the 1996 IEEE* , vol.1, no., pp.153-161 vol.1, 6-10 Oct 1996.
- [8] Mirafzal, B.; Skibinski, G.L.; Tallam, R.M.; Schlegel, D.W.; Lukaszewski, R.A.; , "Universal Induction Motor Model With Low-to-High Frequency-Response Characteristics," *Industry Applications, IEEE Transactions on* , vol.43, no.5, pp.1233-1246, Sept.-oct. 2007.
- [9] Mirafzal, B.; Skibinski, G.L.; Tallam, R.M.; , "Determination of Parameters in the Universal Induction Motor Model," *Industry Applications, IEEE Transactions on* , vol.45, no.1, pp.142-151, Jan.-feb. 2009.
- [10] Kerkman, R.J.; Leggate, D.; Skibinski, G.L.; , "Interaction of drive modulation and cable parameters on AC motor transients," *Industry Applications, IEEE Transactions on* , vol.33, no.3, pp.722-731, May/Jun 1997.
- [11] *CEI, IEC Technical Specification TS 60034-18-41*, Qualification and type tests for Type I electrical insulation systems used in rotating electrical machines fed from voltage converters, *first edition 2006-10*.
- [12] Newtons4th Ltd. model PSM1735 Frequency Response Analyzer 10 μ Hz-35MHz. [Online]. Available: www.newtons4th.com
- [13] Adabi, J.; Zare, F.; Ghosh, A.; Lorenz, R.D.; , "Calculations of capacitive couplings in induction generators to analyze shaft voltage," *Power Electronics, IET* , vol.3, no.3, pp.379-390, May 2010.

- [14] Amarir, S.; Al-Haddad, K.; , "A Modeling Technique to Analyze the Impact of Inverter Supply Voltage and Cable Length on Industrial Motor-Drives," *Power Electronics, IEEE Transactions on* , vol.23, no.2, pp.753-762, March 2008.

3 VOLTAGE DISTRIBUTION INSIDE A COIL

This chapter comes from a research on the voltage propagation and can be seen as the natural consequence of the two topics introduced before as it summarizes and specifies some of the aspects of the previous topics. In particular it concerns with the insulation stress and the identification of the causes, and with the overvoltage due to square wave feeding.

Here the attention is focused on the propagation of the voltage inside a coil. An analytical model is derived which allows the computation of the voltage for every instant of time and through the whole coil. Some simplifying hypothesis are considered but the author believes that the final results can be meaningful. An important insulation design consideration is derived which somehow is in contrast with the common manufacturing technique of reinforcing small insulation parts for tooth coils and random windings machines.

The influence of the constructive parameter related to the insulation, as the capacitance across the turns and toward ground, will be show and will help to deeply understand the effect of the insulation modification on the voltage distribution. This study has been presented in the 2011 International Symposium on Diagnostics for Electric Machines, Power Electronics & Drives (SDEMPED) [1].

3.1 COIL MODEL AND VOLTAGE DISTRIBUTION

Some previous works have focused on the transmission line modeling and on the wave propagation theory applied to the voltage distribution inside a winding [2], [3], [4]. The motor, fed by a power converter, is considered as a very high impedance load in order to underline the impedance mismatch between the machine and the cable as explained in the previous chapter. Very good results are obtained, compared to experimental results, in order to predict the voltage level at the machine's terminals.

A complete vision of the physical phenomenon is explained in [5] where motor failure mechanism due to switching devices and inter-turn overvoltage is considered for a low voltage random-wound motor. Other works focused on the machine's model in order to deeply analyze the voltage propagation inside the windings [6], [7], [8]. Some authors used the lumped parameters model in order to analyze the voltage level at certain points along the winding when a surge is applied at the terminals.

A new approach to the voltage propagation theory has been presented in [9], where the concept of multiconductor transmission line has been applied to the series of the coil turns in the stator slots. This approach was also used in [10], [11] to take account of the core lamination of the stator in the inter-turn voltage prediction.

The same approach was deeply investigated in [12], [13] where the multiconductor transmission line is considered with losses, skin effects and all the physical system is taken into account. Based on this approach, the influence of coil parameters on voltage distribution is also investigated and some consideration about the insulation thickness are derived in [14].

The voltage distribution prediction, has some important diagnostic purpose concerning the maintenance and the winding construction. The voltage level can strongly affects the partial discharge activity inside the winding and so the reliability of the electrical machine [15], [16].

In this chapter the author refers to a simplified coil model where no series resistance is considered nor dielectric losses and therefore the results will be affected by this. So the aim of this study is not to derive a very precise model to predict the exact voltage distribution but to underline the influence of the insulation

manufacturing on the voltage distribution. So the effect on the voltage of changing the inter-turn capacitance or the capacitance to ground are investigated to give a guidance to better understand the insulation modification effects.

The electrical model for the coil winding is shown in Figure 3.1. It can be seen that only the inter-turns capacitance C_i , the ground-coupling capacitance C_g , and the turn inductance L are considered. The model is a distributed parameter model and so the parameters are reported as a function of the spatial variable dx . This way no coil section are defined and the accuracy of the solution is not a function of the number of section considered.

The theory of K.W. Wagner is proposed [17], [18] for the voltage analytical solution. In particular the voltage-to-ground at any point along the winding and at any time is presented. The solution is based on the assumption that a unit voltage ideal step is applied at the machine's terminal and all the voltage levels are referred to the unit value. Furthermore the winding is considered to have the neutral point grounded.

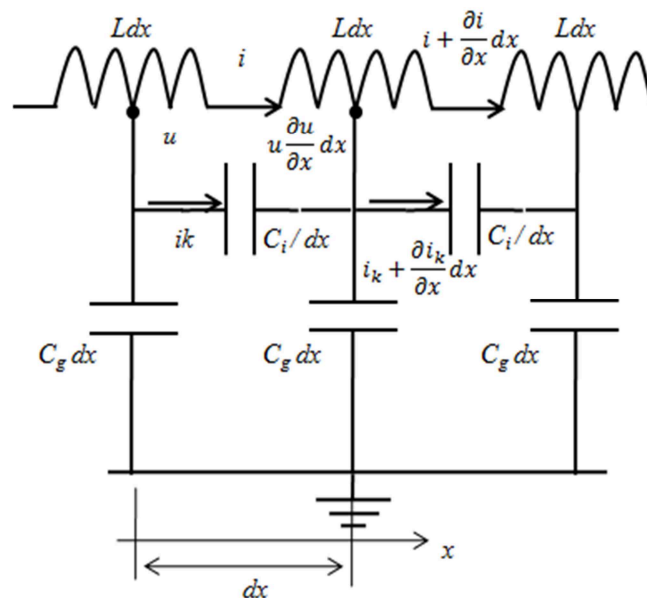


FIGURE 3.1 DISTRIBUTED PARAMETERS COIL MODEL

These two hypothesis, and in particular the first, do not correspond to the real in-service case of a machine's winding. The voltage step applied has always a finite derivative ramp, as shown in the previous chapters, and the end winding terminal is not at zero potential. This two consideration anyway introduce a simplification in the resolving procedure and allow to derive a quite simple solution. Furthermore the unit step ideal voltage can be seen as a much more severe test and so the results are somehow preventive than the one that can be really observed. As reported in [17], this model doesn't account for the mutual inductance between the turns, or the iron losses due to the eddy currents but the authors assume that this model can be quite useful to consider the effect of the variation of the coil parameters in order to better understand the role the insulation of the coil plays in the voltage distribution along the windings.

So considering the model, the relations are:

$$\frac{\partial(i + i_k)}{\partial x} = -C_g \frac{\partial u}{\partial t} \quad (3.1)$$

$$i_k = -C_i \frac{\partial^2 u}{\partial t \partial x} \quad (3.2)$$

$$\frac{\partial u}{\partial x} = -L \frac{\partial i}{\partial t} \quad (3.3)$$

where u is the voltage to ground, i and i_k the currents as in the Figure 3.1.

Differentiating the (3.2) and the (3.3) respect to x and substituting into (3.1), after little computation, the following is obtained for the voltage u :

$$\frac{\partial^2 u}{\partial x^2} - LC_g \frac{\partial^2 u}{\partial t^2} + LC_i \frac{\partial^4 u}{\partial x^2 \partial t^2} = 0 \quad (3.4)$$

This equation represents the voltage transient inside the coil.

The solution is taken in the form:

$$u = U e^{j\omega t} e^{j\alpha x} \quad (3.5)$$

where ω is the angular frequency of a standing wave and α is the periodicity of the wave in the 2π interval.

Substituting the expression (3.5) in the (3.4), the following relation between α and ω can be derived:

$$\alpha^2 - LC_g \omega^2 - LC_i \alpha^2 \omega^2 = 0 \quad (3.6)$$

and also:

$$\omega = \frac{\alpha}{\sqrt{\left[LC_g \left(1 + \frac{C_i}{C_g} \alpha^2\right)\right]}} \quad (3.7)$$

which gives the relation between the angular frequency and the spatial frequency.

The response of the coil to an impulse can be divided into three intervals in which different physical phenomena are considered. In the first one the voltage is established all along the coil few instant after the surge has come at the machine terminals. This distribution is almost entirely due only to the capacitance distribution in the coil and the proportion between the ground capacitance and the inter-turn capacitance. So, if the charging time of the capacitors can be neglected, this event can be separated in time from the others being the first and the fastest one.

During the second time interval the voltage oscillates with respect to the frequencies described in the (3.5) in order to reach the final value state in the third time interval.

So, if the elapsed time to charge the capacitance of the winding can be neglected (instantaneous initial voltage distribution in the winding), the differential equation describing the initial state is obtained considering only the capacitance in the proposed model of Figure 3.1, and thus resulting in the following relation:

$$\frac{\partial^2 u_0}{\partial x^2} = \frac{C_g}{C_i} u_0 \quad (3.8)$$

where u_0 is the initial voltage.

If the unit step surge applied at the machine terminals is considered and the coil end is grounded, the following apply:

$$x = 0, u_o = 1; \quad (3.9)$$

for the unit step at the coil beginning, and:

$$x = l, u_o = 0 \quad (3.10)$$

for the coil end zero voltage being l the coil length.

The solution of the (3.8) which satisfy the initial conditions is:

$$u_o = \frac{\sinh(\gamma \cdot (l - x))}{\sinh(\gamma l)} \quad (3.11)$$

where:

$$\gamma = \sqrt{\frac{C_g}{C_i}} \quad (3.12)$$

Now the final distribution is investigated. At the end of the oscillatory voltage behavior, the voltage is in steady-state condition. Hence, all the time derivative in the (3.4) are set to zero.

So the final voltage u_f is given by:

$$\frac{\partial^2 u_f}{\partial x^2} = 0 \quad (3.13)$$

with a solution in the form:

$$u_f = Ax + B \quad (3.14)$$

And after imposing the boundary condition (3.9), (3.10):

$$u_f = 1 - \frac{x}{l} \quad (3.15)$$

Once the initial and the final voltage expression have been derived, the general solution of equation (3.4), in term of the oscillatory part linking the initial and final state, can be analyzed. The expression is in the form:

$$u = \sum_n [(a_n \cos(\alpha_n x) + b_n \sin(\alpha_n x)) \cos(\omega_n t)] \quad (3.16)$$

and considering that the voltage oscillation at the machine's terminals is zero (unit step applied): $u(0, t) = 0$ and so $a_n = 0$.

If also the condition of the grounded neutral end is considered: $u(l, t) = 0$, and so $\alpha_n l$ must be equal to an integer multiple of π :

$$\alpha_n = n \frac{\pi}{l} \quad (3.17)$$

The resulting voltage as a function of the coil length and the time is:

$$u(x, t) = 1 - \frac{x}{l} + \sum_n [b_n \sin\left(\frac{n\pi}{l}x\right) \cos(\omega_n t)] \quad (3.18)$$

To determine the value of b_n , the voltage $u(x, t)$ must equal, in $t = 0$, the initial distribution given in (3.11) and after some calculation b_n is derived as follows:

$$b_n = -\frac{2}{n\pi} \frac{(\gamma l)^2}{(n\pi)^2 + (\gamma l)^2} \quad (3.19)$$

So the final expression for the voltage at any point and time is:

$$u(x, t) = 1 - \frac{x}{l} - 2 \sum_{n=1,2,3\dots} \left[\frac{1}{n\pi} \frac{(\gamma l)^2}{(n\pi)^2 + (\gamma l)^2} \sin\left(\frac{n\pi}{l}x\right) \cos(\omega_n t) \right] \quad (3.20)$$

This expression was first given in [18] and, despite of the elements neglected, is a valid statement in order to evaluate, on a quality level, the voltage distribution inside the coil.

This solution has been derived neglecting some important elements and phenomena as the iron-losses or the series resistance of the coil as underlined before. This fact leads to an inaccurate solution regarding the oscillation frequency and the voltage level. The author, anyway, believe that this simplified analysis can help in giving an insight look on the distribution of the voltage and can be used to better understand the variation of the distribution as a function of the constructive parameters. The voltage distribution derived, therefore, has the aim of identify and explore the effect of the parameter mutation as a guide for the insulation construction and modification.

3.2 SOLUTION ALGORITHM

A solution algorithm in order to solve the (3.20) is developed as reported in Figure 3.2. The algorithm allows to set the coil parameters (C_g, C_i, L, l) and the sampling time for the resolution. A time step $dt = 1 \cdot 10^{-4}$ s is chosen while the complete time window is set to 1 s. The (3.20) is computed recursively with the summation index $n = 100$. First the step on the variable x is done. Then keeping x constant, the time variable is run till the end of the time interval that is 1 second. After that the maximum voltage upon the time interval is registered. Then x is incremented of another step and the same procedure is run again obtaining the maximum voltage distribution along the coil. The algorithm is shown in Figure 3.2.

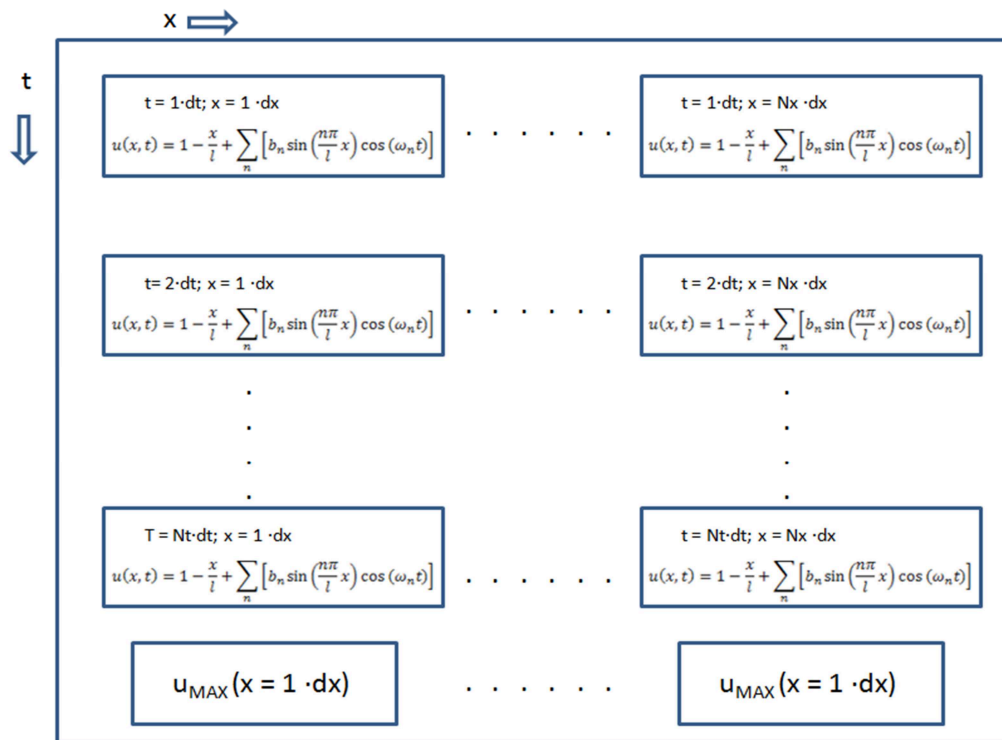


FIGURE 3.2 ALGORITHM FOR THE VOLTAGE DISTRIBUTION COMPUTATION

The number of elements in which the coil's length is divided is 100 so it's equivalent to 100 elements lumped parameter line but, thanks to the analytical solution, the computation time is shorter compared to an equivalent circuit run with a circuit modeler program.

The values used for the inductance and the capacitances are not taken from measurements or Finite Element Method analysis (FEM) but are somehow chosen to be reference parameter. The measured or simulated parameters differ a lot from one configuration to another. For example the coupling between the turns of a random wound winding is completely different from the coupling in a form wound winding. Furthermore also the capacitance to ground is very uneven between all the possible coil configurations. So the aim of this chapter is to underline the importance of the coil constructive parameter on the voltage distribution. The consideration derived are valid for all the kind of coils represented by the circuit of Figure 3.1. The reference values adopted for this simulation are reported in Table 10.

TABLE 10 COIL REFERENCE PARAMETERS

C_g [pF/m]	C_i [pF/m]	L [μ H/m]	l [m]
100	10	0.1	100

The simplifications introduced with this analytical method allows the computation of the maximum voltage without using software for electrical circuit design which, for one hundred circuital segments, would bring to difficult schematic drawing and very time consuming simulation.

3.3 SIMULATION RESULTS

After running the algorithm described in section 3.2, the results are displayed as maximum voltage registered in the time window distributed along the coil length. Using the so called reference parameter for the coil, the distribution of Figure 3.3 is obtained.

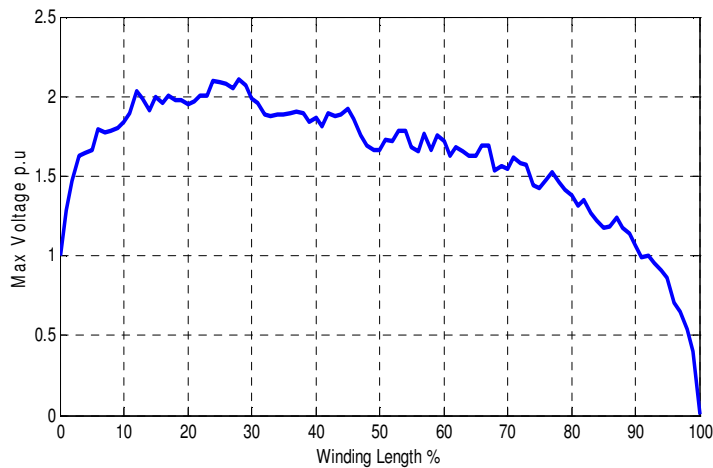


FIGURE 3.3 VOLTAGE PEAK DISTRIBUTION ALONG THE WINDING FOR $C_i=0.01nF$ AND $C_g=0.1nF$

The voltage is reported in per unit, being 1 the voltage level reached by the voltage step applied at the coil terminal. This is a severe situation, even if no overvoltage is simulated at the machine's terminals, because the unit step has an infinite derivative while the typical IGBT's voltage rise time are in the order of 100 ns ÷ 200 ns. It can be seen that the voltage-to-ground along the coil reaches more than two times the unit level applied, at a distance between 10% and 30% of all coil length. Now the voltage-to-ground distribution variation as a function of the inter-turn capacitance and the ground capacitance is investigated.

Increasing 10 times the inter-turn capacitance leads to the voltage peak to ground distribution reported in Figure 3.4.

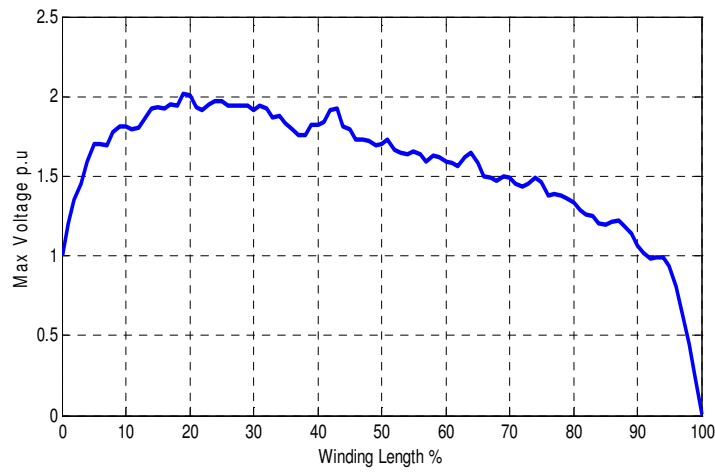


FIGURE 3.4 VOLTAGE PEAK DISTRIBUTION ALONG THE WINDING FOR $C_i=0.1nF$ AND $C_g=0.1nF$

Now the voltage distribution is more uniform and the peak level is 2 times the applied voltage step. The benefits of the inter-turn capacitance growth are more evident if its value is increased again to $C_i = 1nF$.

In this case the voltage distribution is shown in Figure 3.5.

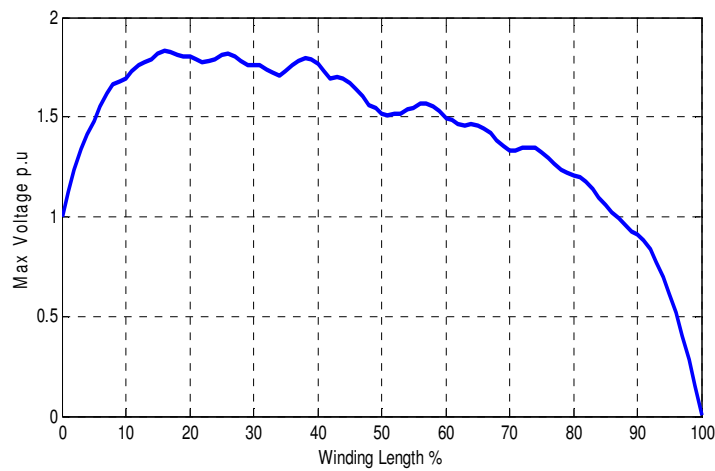


FIGURE 3.5 VOLTAGE PEAK DISTRIBUTION ALONG THE WINDING FOR $C_i=1nF$ AND $C_g=0.1nF$

Now the peak voltage is well below the 2 times value as expected from a more uniform voltage distribution inside the winding. A quite perfect equal distribution is obtained for a $\frac{C_i}{C_g}$ ratio of 1000 as reported in Figure 3.6.

This underlines the influence not only of the inter-turn capacitance alone, but also of the ratio, defined in (10), between the capacitance-to-ground and the inter-turn capacitance on the voltage distribution as the main influencing element.

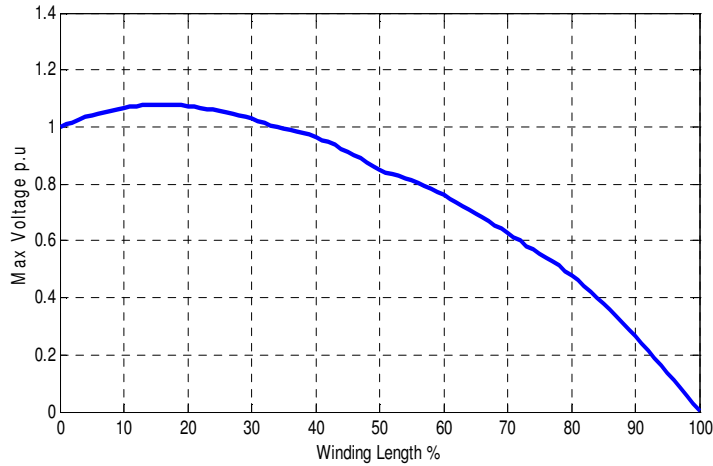


FIGURE 3.6 VOLTAGE PEAK DISTRIBUTION ALONG THE WINDING FOR $C_i=10\text{nF}$ AND $C_g=0.01\text{nF}$

The voltage distribution along the winding is quite uniform and the peak value reaches only 1.1 times the unit voltage step applied at the line end coil terminals. So the importance of the inter-turn capacitance with respect to the ground capacitance in the voltage distribution is proved.

The algorithm developed, even if it doesn't account of the eddy current losses or the mutual inductance between the turns, can be used to roughly predict the voltage-to-ground distribution of an insulation system where the first coil or some turns of this coil have a reinforced insulation layer in order to withstand the increased turn-to-turn or turn-to-ground voltage registered.

This is a quite common industrial solution applied for the electrical machines, like induction motors or synchronous generators, directly faced to electronic power converter which produces repetitive voltage pulses at the machine's terminals. This practical solution is adopted simply looking at the point where the maximum voltage insists that is believed to be the coil's terminal but it is not well supported by a deep analysis on the voltage distribution in case of a non-homogeneous insulation. As reported by other authors in [13], [18], this intervention on the insulation thickness can deform the voltage distribution and, eventually, can result in a higher stress level.

This consideration is also supported by the developed algorithm. The algorithm was properly modified in order to account for different capacitance from the coil terminal to a defined part of the winding. The voltage distribution is plotted, but in this case a homogeneous insulation layer toward a reinforced layer is compared as shown in Figure 3.7.

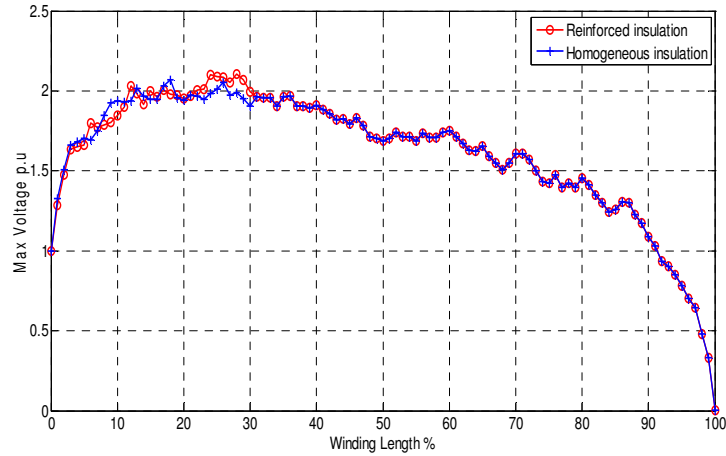


FIGURE 3.7 VOLTAGE PEAK DISTRIBUTION ALONG THE WINDING FOR REINFORCED INSULATION WINDING (30%, $C_i=0.01nF$ AND $C_g=0.1nF$) AND HOMOGENEOUS INSULATION WINDING WITH $C_i=0.1nF$ AND $C_g=1nF$

The Homogeneous insulation system (blue curve, plus markers) has been considered with constant turn-to-turn and turn-to-ground capacitance defined by $C_i = 0.1 nF$ and $C_g = 1 nF$ all along the coil while the reinforced insulation system (red curve, circle markers) has the first 30% of the winding with increased insulation thickness between turns and toward ground. This results in a decreasing of both turn-to-turn and turn-to-ground capacitance for which the values of $C_i = 0.01 nF$ and $C_g = 0.1 nF$ were considered, which means 1/10 of the previous ones.

As can be seen in Figure 3.7, the reinforced insulation system has also an increased voltage stress level, in particular in proximity of the reinforcement end (at 30% of the coil length) where the greater voltage rise due to impedance changing is expected. This fact can lead the non-reinforced winding part, to face an increased voltage level.

From 30% of the winding length till 100%, the maximum voltage level is the same, resulting in an equal stressing level. If the insulation thickness is increased more and so reinforced more, let's suppose until the capacitances decrease to $C_i = 1 pF$ and $C_g = 10 pF$, the non-uniform voltage distribution is more evident as reported in Figure 3.8.

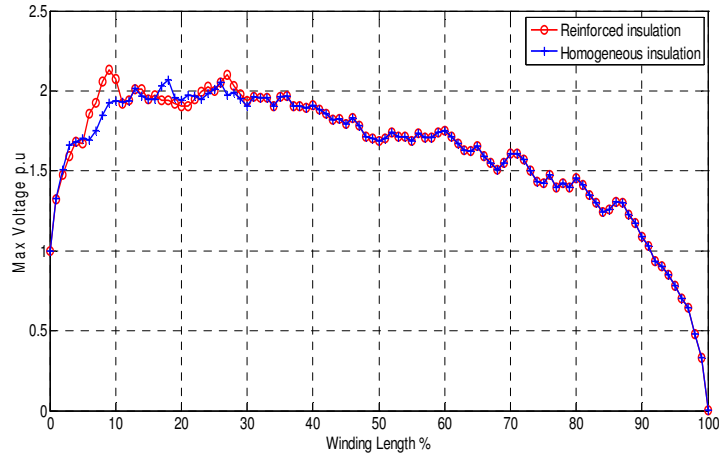


FIGURE 3.8 VOLTAGE PEAK DISTRIBUTION ALONG THE WINDING FOR REINFORCED INSULATION WINDING (30%, $C_i = 1\text{pF}$ AND $C_g = 10\text{pF}$) AND HOMOGENEOUS INSULATION WINDING WITH $C_i = 0.1\text{nF}$ AND $C_g = 1\text{nF}$.

The maximum voltage level is clearly increased in the 5% – 10% length range while, once again, the voltage stress level at the end of the reinforcement is higher.

The reinforcement of both the turn-to-turn and turn-to-ground insulation thickness results to be a counterproductive action, which, even if it increases the voltage withstanding of a coil part, it brings the peak voltage distribution to be less uniform; some winding part after the reinforcement can be affected by an increased voltage level.

As the last case, the decreasing of only the capacitance to ground is analyzed. This corresponds to an increased insulation thickness between the coil and the ground, leaving unchanged the turn-to-turn insulation and so the relative capacitance. This kind of insulation system is compared to an insulation with thinner layer and the result is presented in Figure 3.9.

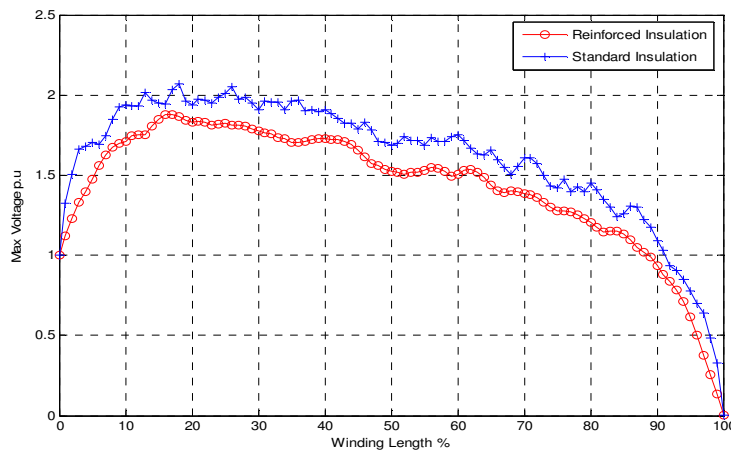


FIGURE 3.9 VOLTAGE PEAK DISTRIBUTION ALONG THE WINDING FOR REINFORCED GROUND INSULATION WINDING ($C_i = 0.1\text{nF}$ AND $C_g = 10\text{pF}$) AND HOMOGENEOUS INSULATION WINDING ($C_i = 0.1\text{nF}$ AND $C_g = 1\text{nF}$)

The benefits of the increased $\frac{C_i}{C_g}$ ratio in the reinforced winding is quite evident. The voltage peak is strongly reduced meaning that increasing the insulation thickness toward ground can bring benefits if the inter-turn

insulation remains unchanged. The important aspect to notice is that in this case all the insulation along the coil has been reinforced. A partial insulation reinforcement can lead to impedance discontinuity inside the coil and so to an hidden reflection effect inside the coil that can increase the voltage stress. This effect can cause the insulation wearing and a massive fault in an internal coil point not easy to detect.

In conclusion, despite of the simplified model considered, the results can be quite useful to deeply understand the problem of the maximum voltage stress level and its location. The influence of the coils parameters, like the turn-to-turn capacitance and the turn-to-ground capacitance on the voltage distribution is studied using a simple algorithm which can create the map of the peak voltage inside the winding.

These considerations are of general purpose and specific values for a certain machine have to be evaluated case by case.

REFERENCES

- [1] Castelli-Dezza, F.; Maglio, M.M.; , "A coil model for voltage distribution and electrical insulation analysis," *Diagnostics for Electric Machines, Power Electronics & Drives (SDEMPED), 2011 IEEE International Symposium on* , vol., no., pp.444-450, 5-8 Sept. 2011.
- [2] A. von Jouanne, P. N. Enjeti, "Design Considerations for a Inverter Output Filter to Mitigate the Effects of Long Motor Leads in ASD Applications,"*IEEE Trans. On Industry Applications*, vol. 33, pp. 1138-1145, Sep/Oct. 1997.
- [3] R. Kerkman, D. Leggate, D. Skibinski, "Interaction of Drive Modulation and Cable Parameters on AC Motor Transients," *IEEE Trans. On Industry Applications*, vol. 33, pp. 722-731, May/June 1997.
- [4] Amarir, S.; Al-Haddad, K.; , "A Modeling Technique to Analyze the Impact of Inverter Supply Voltage and Cable Length on Industrial Motor-Drives," *Power Electronics, IEEE Transactions on* , vol.23, no.2, pp.753-762, March 2008.
- [5] Melfi, M.; Sung, J.; Bell, S.; Skibinski, G.; , "Effect of surge voltage risetime on the insulation of low voltage machines fed by PWM converters," *Industry Applications Conference, 1997. Thirty-Second IAS Annual Meeting, IAS '97., Conference Record of the 1997 IEEE* , vol.1, no., pp.239-246 vol.1, 5-9 Oct 1997.
- [6] Clerici, D.; Della Torre, F.; Morando, A.P.; , "A Form-Wound Induction Machine Model for the Study of Three-Phase Surge Propagation," *Energy Conversion, IEEE Transactions on* , vol.25, no.1, pp.199-206, March 2010.
- [7] Adjaye, R.E.; Cornick, K.J.; , "Distribution of switching surges in the line-end coils of cable-connected motors," *Electric Power Applications, IEE Journal on* , vol.2, no.1, pp.11-21, February 1979.
- [8] Guardado, J.L.; Cornick, K.J.; , "Calculation of machine winding electrical parameters at high frequencies for switching transient studies," *Energy Conversion, IEEE Transactions on* , vol.11, no.1, pp.33-40, Mar 1996.
- [9] Wright, M.T.; Yang, S.J.; McLeay, K.; , "General theory of fast-fronted interturn voltage distribution in electrical machine windings," *Electric Power Applications, IEE Proceedings B* , vol.130, no.4, pp.245-256, July 1983.
- [10] Keerthipala, W.W.L.; McLaren, P.G.; , "Modeling of effects of laminations on steep fronted surge propagation in large AC motor coils," *Industry Applications, IEEE Transactions on* , vol.27, no.4, pp.640-644, Jul/Aug 1991.
- [11] Keerthipala, W.W.L.; McLaren, P.G.; , "A multiconductor transmission line model for surge propagation studies in large a.c. machine windings," *Circuits and Systems, 1990., Proceedings of the 33rd Midwest Symposium on* , vol., no., pp.629-632 vol.2, 12-14 Aug 1990.
- [12] Lupo, G.; Petrarca, C.; Vitelli, M.; Tucci, V.; , "Multiconductor transmission line analysis of steep-front surges in machine windings," *Dielectrics and Electrical Insulation, IEEE Transactions on* , vol.9, no.3, pp.467-478, Jun 2002.

- [13] Petrarca, C.; Maffucci, A.; Tucci, V.; Vitelli, M.; , "Analysis of the voltage distribution in a motor stator winding subjected to steep-fronted surge voltages by means of a multiconductor lossy transmission line model," *Energy Conversion, IEEE Transactions on* , vol.19, no.1, pp. 7- 17, March 2004.
- [14] Petrarca, C.; Lupo, G.; Tucci, V.; Vitelli, M.; , "The influence of coil parameters on the voltage distribution in a machine stator winding fed by a PWM inverter," *Electrical Insulation and Dielectric Phenomena, 2000 Annual Report Conference on* , vol.2, no., pp.490-493 vol.2, 2000.
- [15] Cavallini, A.; Fabiani, D.; Montanari, G.C.; , "A novel method to diagnose PWM-fed induction motors," *Dielectrics and Electrical Insulation, IEEE Transactions on* , vol.15, no.5, pp.1313-1321, October 2008.
- [16] Tozzi, M.; Montanari, G.C.; Fabiani, D.; Cavallini, A.; Gao, G.; , "Off-line and on-line pd measurements on induction motors fed by power electronic impulses," *Electrical Insulation Conference, 2009. EIC 2009. IEEE* , vol., no., pp.420-424, May 31 2009-June 3 2009.
- [17] B. Heller, A. Veverka, *Surge Phenomena in Electrical Machines*. London: London Ilife Books Ltd., 1968.
- [18] K. W. Wagner, "Das eindringeneiner elektromagnetischen welle ineinespulemitwindungskapazit"at," in *Elektrotechnik und Maschinenbau*, vol. 89, 1915, pp. 89–92.
- [19] Wright, M.T.; Yang, S.J.; McLeay, K.; , "The influence of coil and surge parameters on transient interturn voltage distribution in stator windings," *Electric Power Applications, IEE Proceedings B* , vol.130, no.4, pp.257-264, July 1983.

4 DIAGNOSTIC TOOLS FOR RAILWAY SYSTEMS – TELEMETRY AXLE POWER FEEDING

This part of the thesis is focused on the telemetry power feeding for a train axle. The train diagnostic and safety has always been an extremely important topic since modern trains were made. Nowadays, thanks to the improvement in sensors, data acquisition and wireless signal transferring systems, new chances arose for train diagnostic to increase the control of critical parts and vital components. The train axles are one of the most important and vital part in a train as they have to stand all the weight of the train and all the mechanical stress received during service. The rails are often irregular in particular in the railroad switches and joints and repetitive stress can cause light crack that can evolve in a massive breakdown of the axle. One of the most sensible part on a train axle is the connection between the axle and the wheel that is spliced on it. In Figure 4.1 the conjunction point between the axle and the wheel is shown.



FIGURE 4.1 TRAIN AXLE AND WHEEL DETAIL

So in the first chapter a brief analysis is made on the strain measurement techniques and tools, and on the relation with the mechanical stress. After that three power feeding system are analyzed based on very different concepts. The first is based on the high frequency magnetic field linkage. This kind of tool has been already developed and some good system are available on market. The author here focuses on the analytical study of the characteristic equations that describe the magnetic flux linkage and the power transmission without contacts in the presence of electrical and electronic components that form the power circuit in order to build a more efficient and reliable structure.

The second method deals with the wireless power transfer system based on antennas and electromagnetic wave propagation. A case study and FEM analysis lead to the antenna design and transferred power computation. The last system is based on an Permanent Magnet electrical machine which can transfer a sufficient amount of power on the rotating axle. Built on a bearing structure, this machine is analyzed with its characteristic equations including the external circuit analysis for the complete system power computation.

4.1 STRAIN MEASUREMENT

One of the most important aspect in the study of mechanics and materials is the relationship between the stress and the strain [1]. The strain is the deformation of a body when subjected to a force. The definition for strain is the deformation per unit length and is given by the symbol ϵ . The strain can be either positive (tensile) or negative (compressive) and can be computed as:

$$\varepsilon = \frac{\Delta L}{L} \quad (4.1)$$

where the equation terms are shown in Figure 4.2.

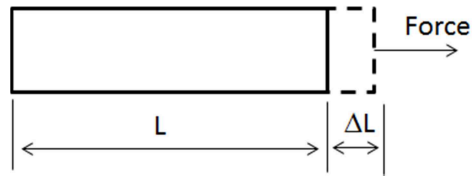


FIGURE 4.2 AXIAL FORCE APPLIED

Since usually strain values are very small, they are often expressed in micro-strain that is $\varepsilon \cdot 10^{-6}$ or $\mu\varepsilon$.

The force F is an uniaxial tensile force. If it is assumed to be equally distributed on the area A of the bar, then the average stress is perpendicular to the bar plane and can be expressed as:

$$\sigma = \frac{F}{A} \left[\frac{N}{m^2} \right] \quad (4.2)$$

The stress could also have a tangential component, not only a normal component, if the force F had a tangential component on the bar surface.

The Hooke's law describes the relationship between the stress and the strain and where the two have a linear relationship, the modulus of elasticity, or Young's modulus, E can be defined as:

$$E = \frac{\sigma}{\varepsilon} \quad (4.3)$$

Not every material shows a linear relationship in their stress-strain diagrams. It's very important to measure the maximum and the minimum strain in a material and so the proper orientation of the applied force has to be known or deduced by measurements.

There are various methods for measuring strain based on mechanical, optical, acoustical, pneumatic and electrical phenomena. Some of them doesn't provide a high measurement accuracy while others require too expensive or delicate instrumentations. The earliest methods used mechanical tools as a micrometer to measure strain with the resolution up to $10 \mu\varepsilon$. The addition of light beam and mirrors improved resolution to $2 \mu\varepsilon$ and gage length down to 6 mm. Another type of device is the photoelectric gage which is based on the combination of mechanical, optical and electrical amplification of the strain. All this devices tend to be bulky or too delicate and most of them are suitable only for static measurements.

The use of electrical phenomena to measure strain is so far the most practical and cheap way. Capacitance and inductance gages have been constructed but vibration sensitivity, mounting difficulties and circuit complexity make them difficult to apply and use in stress analysis work. Also piezoelectric sensors can be used to measure strain as, due to a material deformation, a quite high voltage is generated at its terminals but this sensors are fragile and not suitable for static measurements.

The most workable characteristic that varies with strain is the electric resistance. Different gages has been constructed to measure the resistance variation as the carbon-resistor gage and the semiconductor strain gages but with the disadvantage of an high sensitivity on temperature variations. The most diffused technology is the bonded resistance strain gage. It's made of a very thin wire, or metallic foil, bonded to a thin insulating

layer called carrier matrix. The electrical resistance of the sensor varies linearly with the strain. To measure the strain the matrix must be firmly bonded to the specimen with strong adhesive.

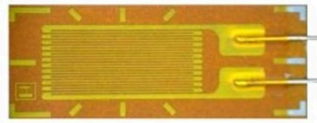


FIGURE 4.3 STRAIN GAGE

As can be seen in Figure 4.3 the strain gage is made of a thin conductor as a winding line in a grid placed on a layer and two external terminals for the resistance measurement. This strain gages are very cheap, only moderately affected by temperature changes and suitable for static and dynamic measurements. Thanks to the printed board technology it's possible to have very thin layer and foils and very compact gages with length between 0.2 mm to 100 mm available on market.

Gages resistance values are usually in the 30 Ω to 3000 Ω range with the 120 Ω and 350 Ω as the most used values.

The carrier matrix has two important function. To provide electrical insulation between the conductor and the specimen and to transmit the proper heat quantity to dissipate. So a proper selection of carrier material, grid alloy, adhesive and protecting coating is mandatory to obtain a reliable tool and good measures of strain.

The measure of the resistance change with strain is the gage factor (GF) defined as:

$$GF = \frac{\frac{\Delta R}{R_G}}{\frac{\Delta L}{L}} = \frac{\Delta R}{R_G} \cdot \frac{L}{\Delta L} \quad (4.4)$$

where ΔR is the change in the resistance, R_G is the resistance of the gage at no strain. It's a dimensionless quantity and the larger is the gage factor the higher is the strain sensitivity.

Also transverse undesired strain could be measured with the gage as the final loops of the winding has also small part in the normal length direction with respect to the grid conductor lines. To minimize this side effect, extra alloy material can be added to the final loops to reduce their resistivity and the grid lines are kept close together. Corrections can be made for the transverse strain in the data analysis phase.

Another source of error in the measure can be the temperature variation. Self-compensating strain gages can be obtained for some specific material as they are made with conductor alloy that compensate for the mismatch in the thermal expansion between the material and the gage.

In order to measure the very small resistance variation due to few strains, a micro ohmmeter must be used but not always this instrumentation is available nor convenient. A more sensitive way for measuring small changes in resistance is with the use of a Wheatstone bridge circuit as shown in Figure 4.4 where R_G is the strain gage resistance.

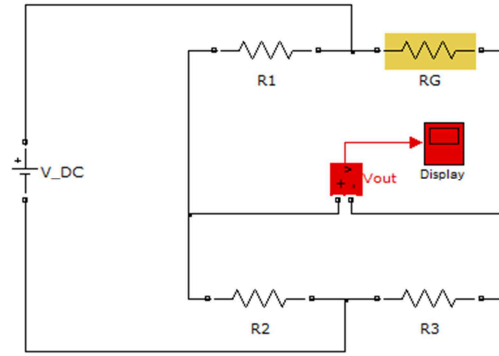


FIGURE 4.4 WHEATSTONE BRIDGE

The resistances R_1 , R_2 and R_3 have a fixed values while R_G , being the strain gage resistance, modifies its value. When the bridge is balanced, that is when $\frac{R_1}{R_2} = \frac{R_G}{R_3}$, the V_{out} is zero. If one resistor, for example R_2 , can be adjusted, the bridge can be balanced when the other resistances values are modified. The expression for V_{out} with unstrained resistance (US subscript) is:

$$V_{out_{US}} = V_{DC} \left[\frac{R_3}{R_3 + R_G} - \frac{R_2}{R_1 + R_2} \right] \quad (4.5)$$

And if the resistance R_g is modified due to the strain, the following stands:

$$V_{out_S} = V_{DC} \left[\frac{R_3}{R_3 + R_G + \Delta R} - \frac{R_2}{R_1 + R_2} \right] \quad (4.6)$$

The use of a Wheatstone bridge increases the measure accuracy and allows to use a computer data acquisition tool to monitor the output voltage. The computer can remove the necessity of balancing the bridge, can compensate the nonlinearities and handle data-storage in multichannel applications. The output voltage variation is related to the gage resistance variation and so a strain measure is obtained. The relationship between V_{out} and the strain is nonlinear but for strains up to few thousand micro-strain the error is usually small enough to be ignored.

Now considering that the unstrained bridge equation is the (4.5) and the strained equation is the (4.6) the following can be written:

$$V_m = \frac{V_{out_S}}{V_{DC}} - \frac{V_{out_{US}}}{V_{DC}} \quad (4.7)$$

and considering $R_3 = R_g$ the following stands:

$$\frac{\Delta R}{R_G} = \frac{-4V_m}{1 + 2V_m} \quad (4.8)$$

Thus remembering the (4.4) the strain can be computed as a function of the voltage difference V_m .

$$\varepsilon = \frac{-4V_m}{GF(1 + 2V_m)} \quad (4.9)$$

which relates the strain with the voltage difference measurable in the bridge before the strain applies and after the strain application.

There are other different techniques for resistance unbalancing measurement to derive the material strain and particular care must be done to multichannel system to avoid interference and to guarantee signal shielding in

the application where the power feeding of the bridge is quite far from it. Stray capacitance as well as common mode voltages can bring to measurement errors due to leakage current flowing into the resistances.

Care must be taken to the voltage feeding level as the higher is the voltage, the higher is the dissipated power in the gage resistance and so the temperature can increase and modify the measure. The grid surface area and the adhesive material must provide a sufficient heat transfer to maintain the grid in a limited temperature range. However bridge output voltage is proportional to the excitation voltage, so reducing V_{DC} means lower sensitivity. The more sensible is the output voltage reading, the lower can be the excitation voltage and so the dissipated power in the gage resistance.

As a conclusion, some considerations on the gage mounting are derived. The resistance of the gain must be measured after the gage is mounted on the specimen in order to detect any possible damage occurred during installation. Furthermore also the insulation resistance between the grid and the support where the gage has been mounted must be checked to verify that no insulation damage or contamination has occurred. Low resistance values (less than 500 M Ω) usually indicates some insulation defects.

Particular attention must be paid to the mounting zone in order to avoid electromagnetic interferences. High frequency integration measurement can reject magnetic interferences together with twisted wires forming minimum and equal loops. Sometimes magnetic and electric field shielding can be required.

Data acquisition and signal plotting is easy to be done nowadays where the storage and processor unit has increased a lot the computation power leading to a faster and efficient diagnostic tools. For the telemetry axle system on a train one of the most important quantity to measure, as said before, is the axle strain nearby the train wheel. The strain gage, as well as the data acquisition and storage electronic board, are obviously on a rotating shaft and so, in order to obtain a more reliable application, wireless data transfer and power feeding must be designed.

Data transfer is done thanks to a wireless radio proprietary protocol that transfer data to an on-board system for signal acquisition and data analysis. This way, selecting a proper radio frequency, data transmission interferences are avoid with other communication systems and with high frequency power feeding systems.

Without deeply analyze the signal acquisition and data transmission board features, the main object of the following chapter will be the analysis and development of wireless power feeding system for telemetry axle systems. Three different systems will be explored with their merits and their defects.

4.2 HIGH FREQUENCY INDUCTION POWER FEEDING

One of the most commonly used technology for wireless power transfer is the high frequency magnetic flux linkage. Thanks to the electromagnetic induction law a considerable amount of power can be transferred at small distances in the air. Some recent researches are pushing the transfer distance toward some meters but this systems are confined to some special applications and sometimes requires high dimensions and particular coil shape [2],[3].

The application the author wants to focus on is an induction power transfer system that can be seen as a transformer with a primary side on a static part (bogie or axle box) and a secondary side on the rotating axle. Between the primary and the secondary there is an air-gap which cannot be kept too low in order to avoid contacts and frictions with the rotating shaft. This fact reduces a lot the magnetic flux density making necessary

the use of a high frequency varying field to induce a proper voltage level at the secondary side. There are different system on the market for telemetry power feeding that rely on this concept. All of them use as a primary a ferrite structure that encloses the high frequency magnetic field generated and confines it to link the coil's turns on the secondary side.

A sketch of this kind of system is shown in Figure 4.5.

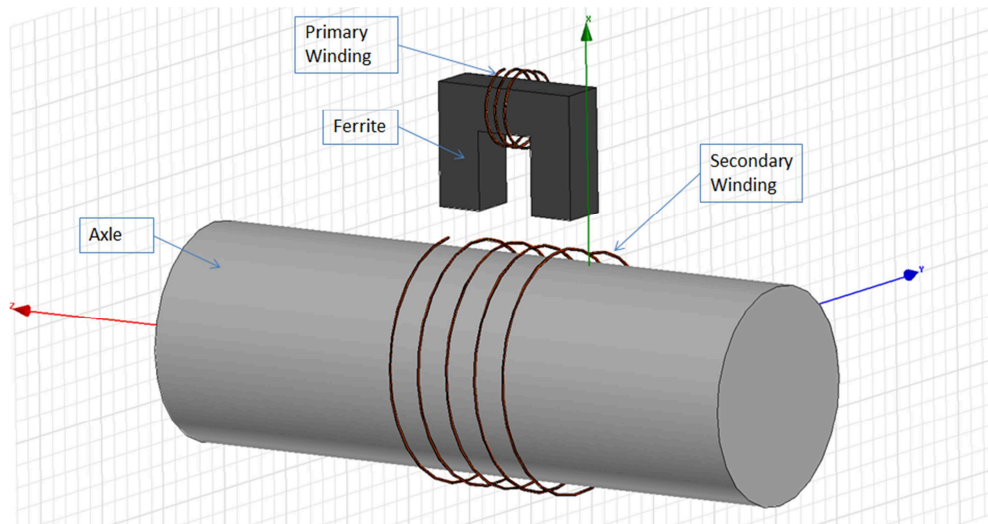


FIGURE 4.5 INDUCTION POWER TRANSFER SYSTEM

The primary winding is powered by a 30 KHz sinusoidal voltage and the magnetic flux generated is directed toward the secondary winding by the ferrite support. The flux linked with the secondary coil induces a voltage and so, when a load is connected, a certain amount of power can be transferred.

This commercially available system uses this principle not only for power transfer but also for the signal transfer device which, modulated at a different frequency, can use the same support, or a similar one, to bring back the gage conditioned signal onboard.

The disadvantages of this kind of technology is that the high frequency generated magnetic field needs a ferrite structure to be confined. So not only the primary winding needs a ferrite support, but also the secondary winding should be wound on a ferrite tape wrapped around the axle to place at a distance the coil from the axle itself. Ferrite material underneath the coil limits Eddy current on the axle surface thus improving the power transfer efficiency. This system has proved a poor magnetic linkage between the two coils and a small air-gap is necessary thus increasing the risk of contacts.

Another possible solution is to wound the secondary coil a little far from the axle on a non-magnetic structure (as a resin or plastic structure) avoiding the use of ferrite tape for the secondary winding (Figure 4.6). The ferrite structure of the primary winding, instead, is always necessary for the high frequency magnetic field generation.

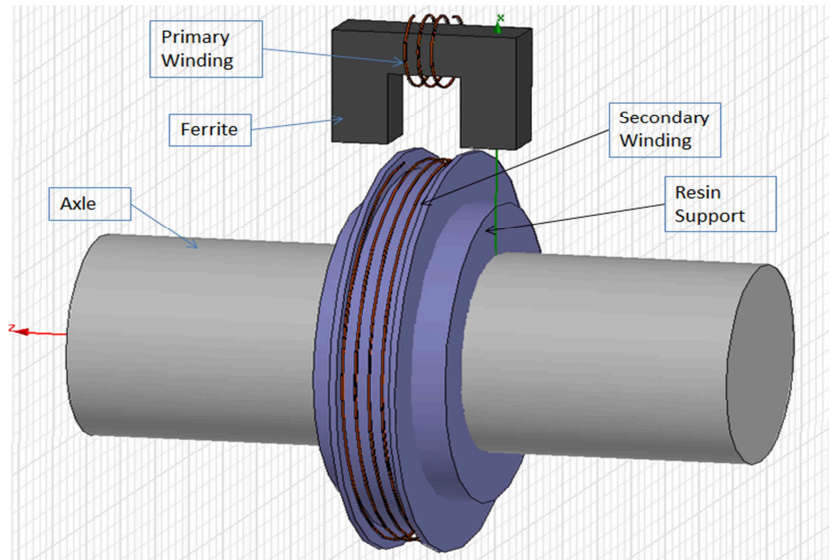


FIGURE 4.6 SECONDARY COIL WITH SUPPORTING STRUCTURE

The resin structure support for the secondary winding brings the coil far from the axle steel thus reducing its interference with the magnetic field linking the coil. This power transfer system has proved experience on-board and a considerable amount of power can be transferred. The disadvantage is that the primary ferrite has to be very near to the rotating support and also that the support has to be composed by two parts in order to be mounted on the axle. So the secondary coil must be wound by hand and all the structure need a protection cover to obtain a more reliable system.

Here below are some photo of the tests performed in the laboratory to verify the power level transferred and the minimum distance required.

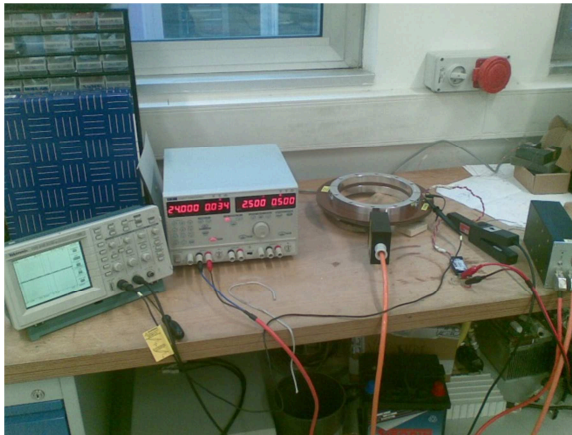


FIGURE 4.7 LABORATORY TEST SETUP

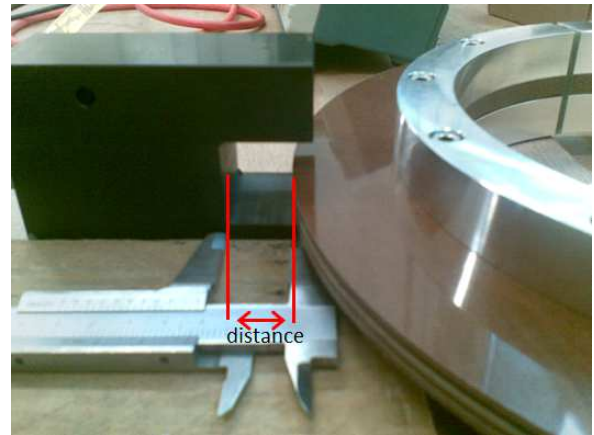


FIGURE 4.8 TEST AT DIFFERENT DISTANCES

TABLE 11 INDUCED VOLTAGE RESULTS

Distance [mm]	RMS AC 32kHz Voltage [V]
150	0.487
100	1.04
75	1.71

50	3.52
40	4.78
30	7.55
20	11.5
10	16.5
5	18.54
0	20.5

In Table 11 the AC induced voltage on the secondary side is displayed as a function of the distance between the primary structure and the secondary structure as highlighted in Figure 4.8. Test on the transferred power revealed that , after a DC conversion unit, the power level of 5 W can be transferred to a resistor load only from 20mm to below. The test was conducted to verify the specimen operation before mounting on a train axle. Other tests were made mounting this unit and all the strain measuring units on a rotating steel cylinder to verify the power and data transmission during operation. This system, as said before, is a commercially available solution and the test made had the aim only to verify its functionality and the distance required for the telemetry power feeding.

The need of a supporting structure for the secondary winding and a framework to keep the primary structure near the rotating axle are the two weak points of this solution.

Another kind of wireless transfer system geometry has been investigated to find a device with better magnetic coupling and without the disadvantages of the previous.

This system is made of two concentric coils. The first, the primary side, relies on a static support while the secondary is more like the winding in Figure 4.5 and rotates with the axle. The system is shown in Figure 4.9 and Figure 4.10.

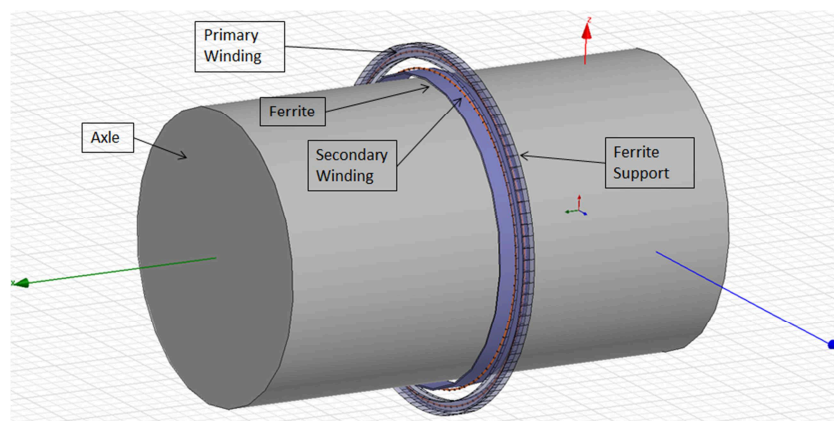


FIGURE 4.9 CONCENTRIC COILS SYSTEM MODEL

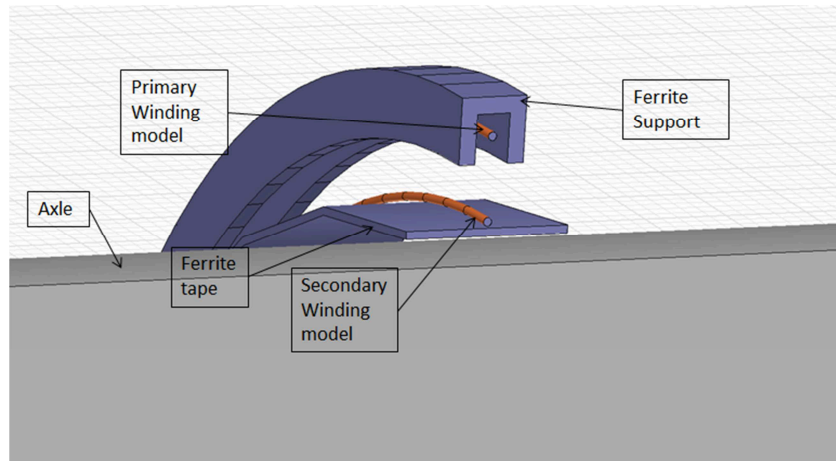


FIGURE 4.10 CONCENTRIC COILS MODEL SECTION

The model in Figure 4.10 has only one coil for the windings because this setup has been used to compute for the magnetic parameters and the winding has been considered ideally concentrated.

This two-concentric coils system has the advantage of having a much higher magnetic coupling coefficient, as will be seen later, and so it needs a less number of turns to generate a sufficient induced voltage level. Furthermore, the compact primary structure can be built in the axle external box where the system is mechanically more stable and protected. The secondary coil can be just made binding the coils around the axle with a ferrite tape support to improve the coupling. The axle protective resin can be used to cover also the winding and the tape thus resulting in a more reliable and robust system.

Figure 4.11 shows the lab setup used for the coils winding. Instead of the air-gap, an adhesive tape is used to separate the primary from the secondary. Obviously this specimen does not allow the relative motion between the two coils which, anyway, remains in the same relative geometrical position of the rotating designed system. The primary coil has been later covered with another ferrite tape to better enclose the magnetic field. So the primary structure is not properly like the one of Figure 4.10 but the built structure can be used to preliminarily investigate on the power transfer capability.

The secondary coil, being under the adhesive tape, is not visible while the primary winding is above the tape.

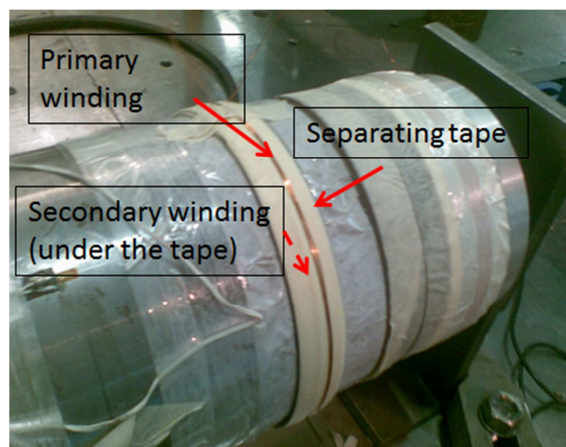


FIGURE 4.11 AXLE WINDINGS SETUP

In Figure 4.12 there is another lab experimental setup used for the coil power transmission tests. The axle is substituted with a more practical iron tube which thickness is 5mm. The Iron skin depth at 30 kHz used for the voltage feeding is 0.014 mm and so far smaller than the tube thickness. The primary and secondary coils are made as in the previous setup and the DC load shown in Figure 4.13 is made of a diode bridge and a 4.7Ω resistance. Test on this system have been performed to evaluate the transferred power between the primary coil and the secondary coil with an air-gap of 3mm.

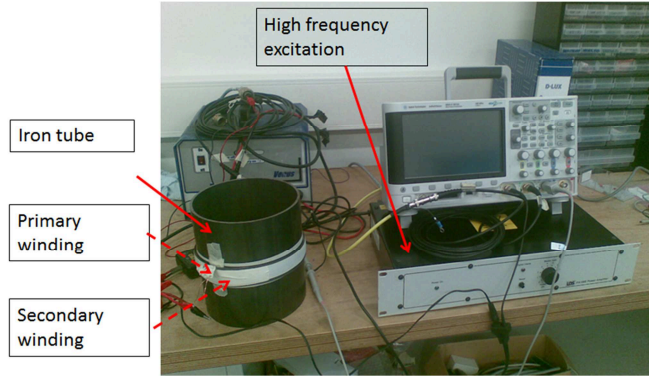


FIGURE 4.12 LABORATORY TEST SYSTEM

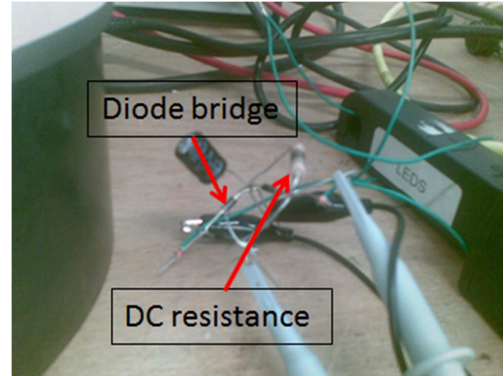


FIGURE 4.13 DC LOAD

- System Equations and FEM Analysis

The whole system can be seen as a mutual inductor as shown in Figure 4.14:

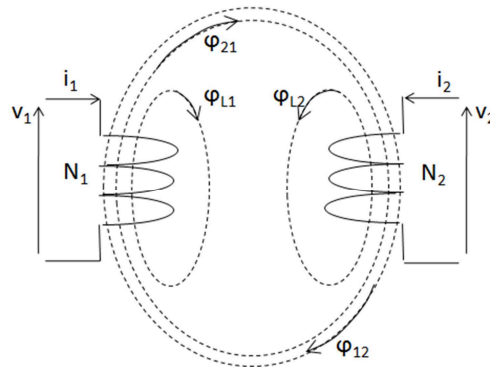


FIGURE 4.14 MUTUAL INDUCTOR MODEL

which equation are the well-known:

$$v_1 = N_1 \frac{d\varphi_1}{dt} = N_1 \frac{d(\varphi_{L1} + \varphi_{21} + \varphi_{12})}{dt} = L_{11} \frac{di_1}{dt} + L_m \frac{di_2}{dt} \quad (4.10)$$

$$v_2 = N_2 \frac{d\varphi_2}{dt} = N_2 \frac{d(\varphi_{L2} + \varphi_{21} + \varphi_{12})}{dt} = L_{22} \frac{di_2}{dt} + L_m \frac{di_1}{dt} \quad (4.11)$$

assuming that the two magnetic permeances associated with the fluxes φ_{21} and φ_{12} are the same and equal to λ_m .

Now if the open circuit secondary voltage is computed, the following is obtained:

$$\left. \frac{v_2}{v_1} \right|_{i_2=0} = \frac{L_m}{L_{11}} \quad (4.12)$$

Then, remembering that $L_m = N_1 N_2 \lambda_m$ and $L_{11} = N_1^2 \lambda_1 = N_1^2 (\lambda_m + \lambda_{L1})$ with λ_{L1} as the magnetic permeance related to the flux φ_{L1} , the following is derived:

$$\left. \frac{v_2}{v_1} \right|_{i_2=0} = \frac{N_2}{N_1} \frac{\lambda_m}{\lambda_m + \lambda_{L1}} \quad (4.13)$$

The (4.13) has a very important meaning as, in a normal transformer with iron core, the ratio $\frac{\lambda_m}{\lambda_m + \lambda_{L1}}$ can be approximated to 1 as the leakage permeance is very small in comparison with the mutual permeance. In this case, since the mutual coupling between the primary coil and the secondary coil is not so good as in the classic transformer, this simplification cannot be introduced and the ratio can be considered as a magnetic coupling index.

The cross section and the dimensions of the system considered are reported in Figure 4.15.

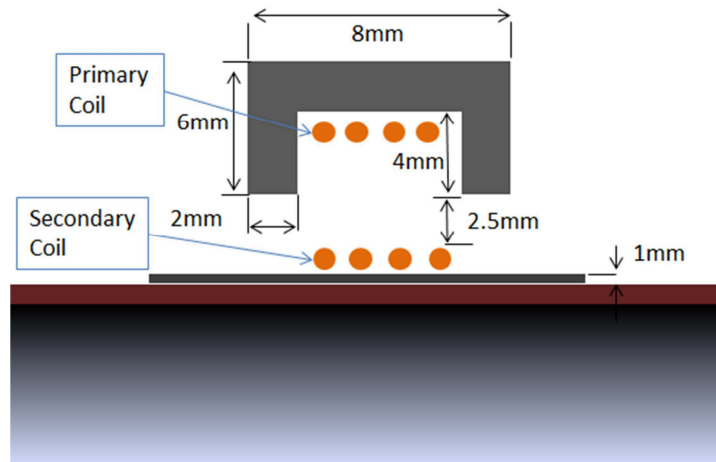


FIGURE 4.15 CROSS SECTION OF THE POWER SUPPLY SYSTEM

From the FEM analysis the parameters in Table 12 have been derived.

TABLE 12 MAGNETIC AND ELECTRIC DATA FROM FEM ANALYSIS

$\lambda_1 [H]$	$\lambda_m [H]$	$\lambda_2 [H]$	$k_1 = \frac{\lambda_m}{\lambda_m + \lambda_{L1}}$	$\lambda_{d1} = \lambda_1 - \lambda_m$ Primary leakage inductance [H]	$\lambda_{d2} = \lambda_2 - \lambda_m$ Secondary leakage inductance [H]
$1.91 \cdot 10^{-6}$	$1.02 \cdot 10^{-6}$	$1.29 \cdot 10^{-6}$	0.534	$8.9 \cdot 10^{-7}$	$2.7 \cdot 10^{-7}$

- Electric Circuit Model

An equivalent electric circuit model based on the layout of Figure 4.14 and data of Table 12 is here derived.

As the mutual inductor model behaves like a transformer with an air core, the latter model will be used for the system representation.

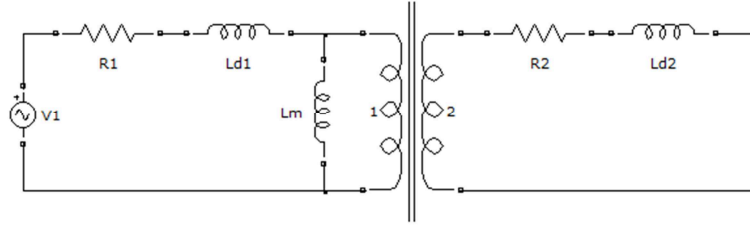


FIGURE 4.16 AIR CORE TRANSFORMER MODEL

In Figure 4.16 the model is shown. V_1 is the AC High frequency voltage feeding of the primary side, R_1 is the primary winding resistance, L_{d1} is the primary leakage inductance, L_m is the magnetizing inductance, R_2 is the secondary winding resistance and L_{d2} is the secondary leakage inductance. The relations for the inductances computation are reported below:

$$L_{d1} = N_1^2 \cdot (\lambda_1 - \lambda_m) = N_1^2 \cdot \lambda_{d1} \quad (4.14)$$

$$L_{d2} = N_2^2 \cdot (\lambda_2 - \lambda_m) = N_1^2 \cdot \lambda_{d2} \quad (4.15)$$

$$L_m = N_1^2 \cdot \lambda_m \quad (4.16)$$

So, thanks to the parameter of Table 12 and the equation (4.14)–(4.16), it's possible to set up an electric circuit model which represents the induction transfer power system. One important thing to notice is that, in comparison with the traditional iron core transformer models, the magnetizing inductance here is very low as the air-gap is quite large. Another thing to notice is that at high frequency the leakage inductance of the primary and secondary winding can bring to high voltage drop making ineffective the power transmission on the load.

The compensation of the leakage inductance can be done with the use of a series capacitor which impedance, at the selected frequency, is equal but opposite in sign to the inductive impedance. The sum of the inductance and the capacitance impedance will be equal to zero and the voltage drop will be caused only by the series resistance. This relation is given in the equation (4.17) which allows to compute, given the value of the frequency and the leakage inductance, the resonant capacitance value.

$$\frac{1}{j\omega C_s} + j\omega L_d = 0 \quad (4.17)$$

This is the well-known principle of the series LC filter used in different application like power filtering and power factor correction. The series resonant converters are used to reduce the harmonic content in the power line and to obtain a good power factor correction. Furthermore the sinusoidal variation of voltages and currents due to a resonant filter element, gives the chance of using a zero-current or zero-voltage switching process which drastically reduces the commutation losses [4]-[7].

One of the application of a series resonant filter is in the Induction Heating where the resonance is used to generate sinusoidal variation of current that creates the high frequency magnetic field for the induction heating and allows the soft switching operation. Resonant conversion is a very wide topic and there are a lot of fields that can take advantage from this principle; induction heating, power factor regulation, input current

shaping and fine voltage control are some of them and, in this case, the resonant principle is used for its voltage drop cancelling feature.

4.2.1 RESONANT WINDING

As briefly said before, the telemetry system, which the wireless power transfer device is designed for, needs a DC power conversion stage in order to work. This is because the electronic circuits and signal analysis units are DC fed together with the gage measuring bridge whose input voltage, the more stable it is, the more accurate is the strain measure.

In order to study the power circuit with a unique representation, some considerations must be derived. Basing on the system model of Figure 4.16, if a series compensating capacitor is adopted for the primary side, the series impedance is drastically reduced in comparison with the magnetizing impedance. The series inductance could be completely cancelled if only the system was driven by a purely sinusoidal current. This case the diode bridge at the secondary side brings to harmonics in the current content and so the effect of the capacitance on the leakage inductance is not complete. To count for this situation, the capacitance and inductance are not cancelled and the complete analytical solution will be derived which comprehends for inductance, capacitance resistance and DC diode voltage imposition. Furthermore to allow the consideration of a unique circuit involving the primary and the secondary side, the position changing of the magnetizing inductance directly in parallel with the primary voltage excitation is here considered valid. This because the magnetizing impedance results to be much higher than the series impedance thanks to the compensation effect of the capacitor and to the fact that the primary resistance is small as few turns are adopted and made of Litz wire. Furthermore the magnetizing inductance can be considered excited only by the first current harmonic and so for the higher harmonics is negligible. Thanks to this principle, the open circuit secondary voltage is no more affected by the low magnetizing inductance and so by the coupling coefficient $k1$. The disadvantage is that the primary current will be only limited by the magnetizing inductance but in this case, being its value the 53.4% of the total series inductance, a proper primary turns number can limit the open circuit current to a reasonable value. Also for the secondary coil the series capacitor compensation is adopted in order to reduce the voltage drop and obtain a more efficient power transfer system. This leads to the system representation with the series resonant capacitances of Figure 4.17.

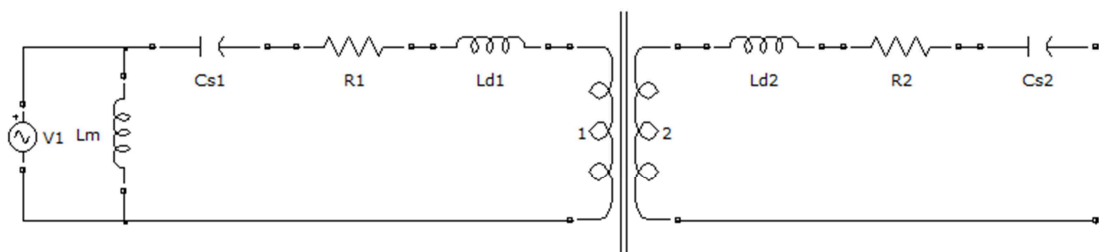


FIGURE 4.17 EQUIVALENT CIRCUIT MODEL WITH SERIES CAPACITORS

As said before the magnetizing inductance can be moved directly in parallel with the voltage source. The primary side parameters can be then moved to the secondary side through the turns ratio $\left(\frac{N_2}{N_1}\right)^2$ to unite the two circuits.

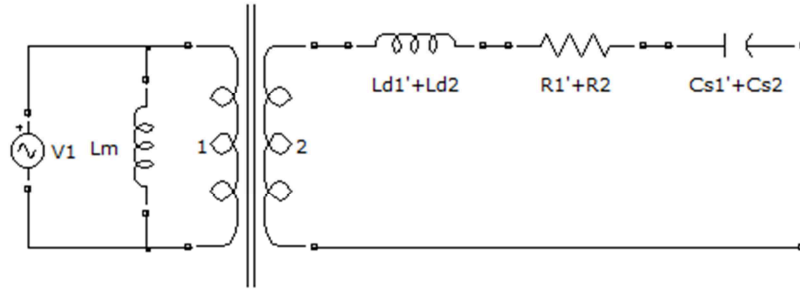


FIGURE 4.18 EQUIVALENT SECONDARY CIRCUIT

The excitation voltage V_1 is directly applied to the magnetizing inductance and hence to the secondary coil through the turn ratio. The open circuit voltage V_{20} can be computed simply as:

$$V_{20} = \frac{N_2}{N_1} V_1 \quad (4.18)$$

So the induced voltage is increased by a factor $\frac{1}{k_1}$.

The complete electrical circuit model must comprise an AC/DC diode rectifier and a DC load that represents the power transferred for the telemetry. The model is shown in Figure 4.19.

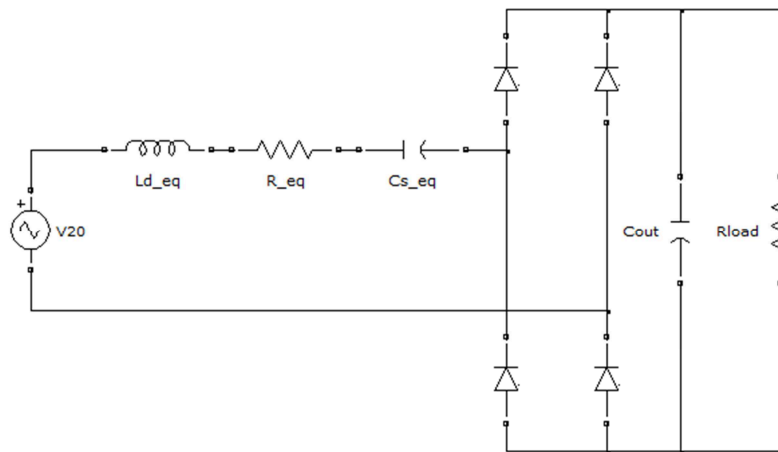


FIGURE 4.19 MODEL WITH SERIES CAPACITOR AND DC RECTIFIER

The secondary coil equivalent parameters count for the primary side parameters multiplied by the squared turns ratio plus the secondary side parameter.

Some previous works [8]-[11] use the simplification hypothesis of a narrow band LC series filter thus completely eliminating the harmonic influence on the voltage and current. This case is slightly different as the leakage inductance is small and so the LC series filter is not very selective.

This complete electric circuit model will be used to verify the analytical study of the equations that regulate the system. This way a comparison between the numerical solution results and the analytical results can be performed. The great advantages of the analytical study is that the performance of the system can be evaluated in a few meaningful graphs that include a large quantity of parameter variation. The same results could be obtained only with a large number of simulations that not only are time consuming, but also hide the complete vision of the system behavior when some parameters are changed.

The diodes voltage drops and their real characteristic are not considered but could be taken into account with an increased DC Bus voltage level and an increased AC series resistance.

The secondary voltage and system parameters design are all related to the geometric structure of the transformer, to the number of turns for the primary and secondary winding and to the DC Bus voltage level.

- Design Equations and Analytical Study

As the magnetizing inductance L_m is considered in parallel with the voltage source, the magnetizing current in the primary winding (no-load condition) is only given by:

$$I_1 = \frac{V_1}{\omega L_m} = \frac{V_1}{\omega N_1^2 \lambda_m} \quad (4.19)$$

Where I_1 is the primary winding current, V_1 the RMS value of the primary excitation voltage and λ_m the magnetizing permeance.

Fixing the primary voltage and the current level, both based on the power feeding device available, from the equation (4.19) it's possible to deduce the number of coil's turn of the primary winding and so:

$$N_1 = \sqrt{\frac{V_1}{\omega I_1 \lambda_m}} \quad (4.20)$$

This consideration does not include the load current which should be included after the load current computation in a iterative process.

Now a simplified model for the secondary winding design is derived. The load is made of a DC rectifier bridge and a constant DC voltage is considered which corresponds to a high DC-Bus capacitance. The circuit is represented in Figure 4.20.

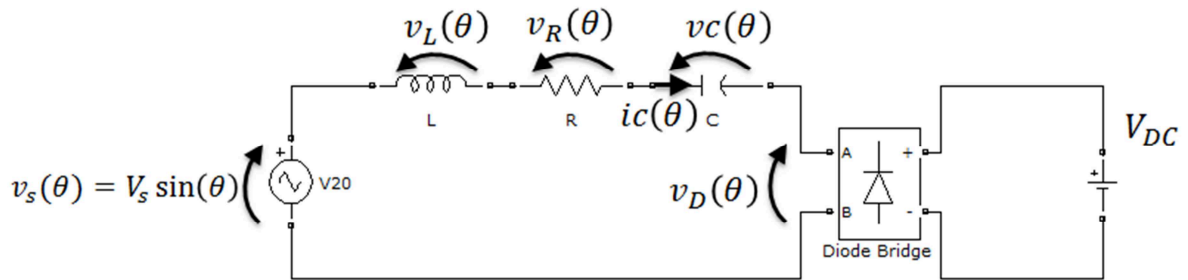


FIGURE 4.20 SECONDARY WINDING MODEL

The sinusoidal voltage excitation is $v_s(\theta)$ which amplitude is V_s ; $v_L(\theta)$, $v_R(\theta)$ and $v_c(\theta)$ are the voltage drops on the series elements among which $v_c(\theta)$ is the state variable. The voltage $v_D(\theta)$ is a square wave because V_{DC} is a constant voltage and, when the diode bridge conducts continuously, it switches from $+V_{DC}$ when the AC current is positive, to $-V_{DC}$ when the AC current becomes negative.

Starting from the model of Figure 4.20 and considering a positive current interval, the equations are:

$$V_s \sin(\theta) - v_R(\theta) - v_L(\theta) - v_c(\theta) - V_{DC} = 0 \quad (4.21)$$

which is the Kirchoff voltage law and:

$$i_c(\theta) = \omega C \frac{dv_c(\theta)}{d\theta} \quad (4.22)$$

$$v_L(\theta) = \omega L \frac{di_c(\theta)}{d\theta} \quad (4.23)$$

which are the element characteristic laws. Thus substituting the (4.22) and (4.23) in the (4.21) leads to:

$$V_s \sin(\theta) - \omega RC \frac{dv_c(\theta)}{d\theta} - \omega^2 LC \frac{d^2v_c(\theta)}{d\theta^2} - v_c(\theta) - V_{DC} = 0 \quad (4.24)$$

In the unique state variable $v_c(\theta)$.

The solution for this equation can be better managed if the equation is written in per unit values (p.u.) where the reference (base) values are: $V_b = V_s$; $I_b = \omega CV_s$; $P_b = \omega CV_s^2$. Considering the relations: $M = \frac{V_{DC}}{V_b}$ for the DC voltage in p.u.; $\xi = \frac{R}{2L\omega}$; $\theta = \omega t$ and $\alpha = \sqrt{1 - \xi^2}$ for the (4.24) solution expression, the following is obtained for the canonical form of the ODE in resonant condition:

$$\frac{d^2\tilde{v}_c(\theta)}{d\theta^2} + 2\xi \frac{d\tilde{v}_c(\theta)}{d\theta} + \tilde{v}_c(\theta) = \sin(\theta) - M \quad (4.25)$$

being $\tilde{v}_c(\theta)$ the capacitor voltage divided by the reference base value V_s . All the terms expressed in the (4.25) are divided by the base values and now on the "tilde" notation will be omitted. The solution of the (4.25) can be written in the following form:

$$v_c(\theta) = (A \cos(\alpha\theta) + B \sin(\alpha\theta))e^{-\xi\theta} - M - \frac{\cos(\theta)}{2\xi} \quad (4.26)$$

And with the (4.22) the current results in:

$$i_c(\theta) = (-A\alpha \cdot \sin(\alpha\theta) + B\alpha \cdot \cos(\alpha\theta))e^{-\xi\theta} - (A \cos(\alpha\theta) + B \sin(\alpha\theta)) \cdot \xi e^{-\xi\theta} + \frac{\sin(\theta)}{2\xi} \quad (4.27)$$

Now it is necessary to distinguish from two working condition of the diode bridge: the continuous conduction mode (CCM) and the discontinuous conduction mode (DCM). The word "conduction" refers to the AC current that can or cannot be continuous during operation. In the latter case the current becomes and remains zero before a new conduction period occurs. The limit and the feature of this two working conditions have been widely explored in literature as the diode bridges started to be used. Anyway this situation is mostly analyzed with only the series inductance or the inductance plus the resonant series capacitor [9]-[11] at the AC side and the analytical solution is derived just for these cases. Here the series resistance, the inductance and the resonant capacitance are considered all part of the circuit as these elements at the secondary winding side are of great importance for a precise solution expression and none of them can be neglected.

- Continuous Conduction Mode (CCM)

In CCM there's no null period in the current $i_c(\theta)$. Considering a generic phase shift δ in the current expression in comparison with the voltage excitation $v_s(\theta)$, the following can be derived:

$$i_c(\delta) = 0 \quad (4.28)$$

which counts for the zero crossing of the current at the angle δ ,

$$i_c(\delta + \pi) = 0 \quad (4.29)$$

which expresses the periodicity of the current in the π interval and

$$v_c(\delta) = -v_c(\delta + \pi) \quad (4.30)$$

which comes from the symmetry of the AC current in the positive and negative period.

Now if the (4.28), (4.29) and (4.30) are solved in the variables A , B and δ these three parameters can be obtained only as a functions of ξ and M .

For the sake of simplicity the expressions are not here reported but the command line of the Maple® program used for the computation can be found in the Appendix A.

This way also the voltage $v_c(\theta)$ and the current $i_c(\theta)$ can be expressed as a function only of ξ , M and obviously of the integration variable θ .

Now that the expression of the current is derived, it's possible to compute for the DC power in p.u. transferred to the DC-Bus simply calculating the average current in a semi-period and multiplying it for M thus obtaining:

$$I_o(\xi, M) = \frac{1}{\pi} \int_{\delta(\xi, M)}^{\delta(\xi, M) + \pi} i_c(\theta) d\theta \quad (4.31)$$

for the mean value of the current and:

$$P_o(\xi, M) = I_o(\xi, M) \cdot M \quad (4.32)$$

for the DC power expressed in p.u. The DC power expressed in Watt [W] will be simply the power P_o multiplied by the reference value $P_b = \omega CV_s^2$.

P_o can be evaluated for every desired power level, varying the two parameters ξ and M to obtain different iso-power curves. As an example the Figure 4.21 represents some DC power levels in a ξ - M plot.

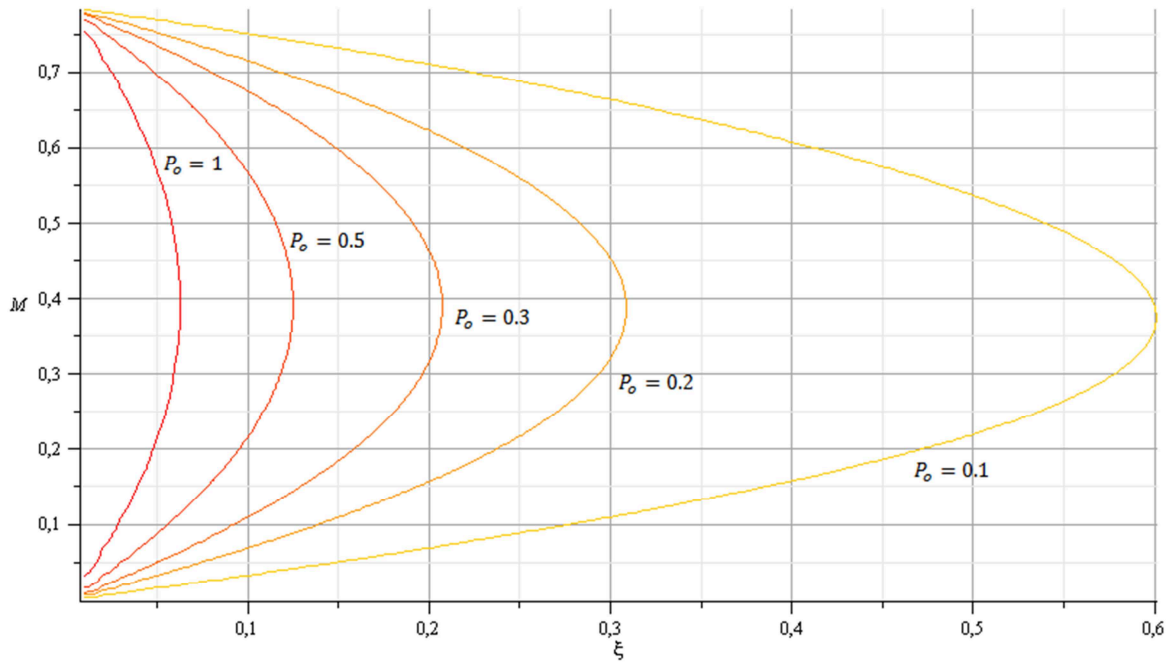


FIGURE 4.21 EXAMPLES OF P_o LEVELS AS A FUNCTION OF ξ AND M

The value of ξ is related to the excitation frequency ω and to the winding constructive parameter (resistance and inductance) hence to the coil's turns N_2 , while M is related to the DC-Bus and excitation voltage levels.

Also the current $i_c(\theta)$ can be computed from (4.27) and an example for a single conduction period is given in Figure 4.22 computed with a small phase shift δ . The diode bridge is in CCM noticeable from the fact that the conduction period angle is equal to π . The same current wave is repeated in the next time interval with negative and positive alternative periods.

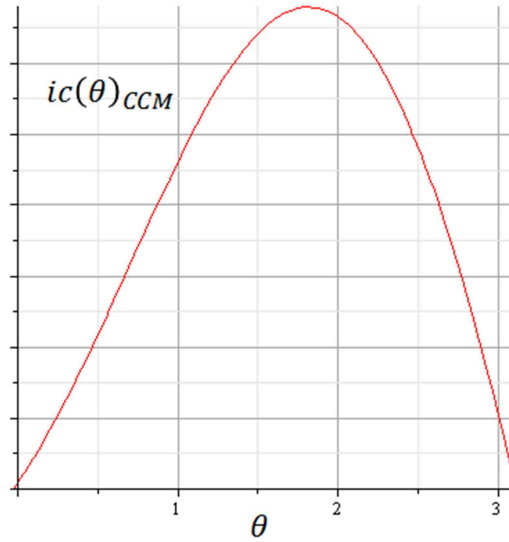


FIGURE 4.22 CCM CURRENT EXAMPLE $i_c(\theta)$

- **Continuous Conduction Mode / Discontinuous Conduction Mode Boundary**

An important boundary for the diode rectifier bridge working condition is the continuous conduction mode/discontinuous conduction mode boundary. In the latter the current is equal and remains to zero till the beginning of the next conduction interval. This boundary has been well described for the cases of only an inductance on the AC circuit side or an inductance with series resonant capacitor [9]-[11]. In this work, as said before, a more complete model, in which also the series resistance is considered, has been taken into account and so the current conduction limits are different.

The discontinuous conduction mode begins for $\theta = \delta$, not only when the AC current is zero as for the condition (4.28), but also when its derivative with respect to the angle is zero which means this additional condition:

$$\left. \frac{di_c(\theta)}{d\theta} \right|_{\theta=\delta} = 0 \quad (4.33)$$

This leads to consider the voltage drop on the series inductance and on the resistance equal to zero and the Kirchhoff voltage law for the circuit is:

$$V_s \sin(\delta) - v_c(\delta) - V_{DC} = 0 \quad (4.34)$$

which in p.u. values becomes:

$$\sin(\delta) - v_c(\delta) - M = 0 \quad (4.35)$$

Forcing this condition to be respected, the AC current crosses the zero axes in δ with a zero derivative, suggesting the beginning of the discontinuous conduction mode.

As δ is a unique function of ξ and M , the CCM/DCM boundary condition expressed by the (4.34) can be introduced in a ξ - M plot as the one of the Figure 4.21 resulting in the Figure 4.23.

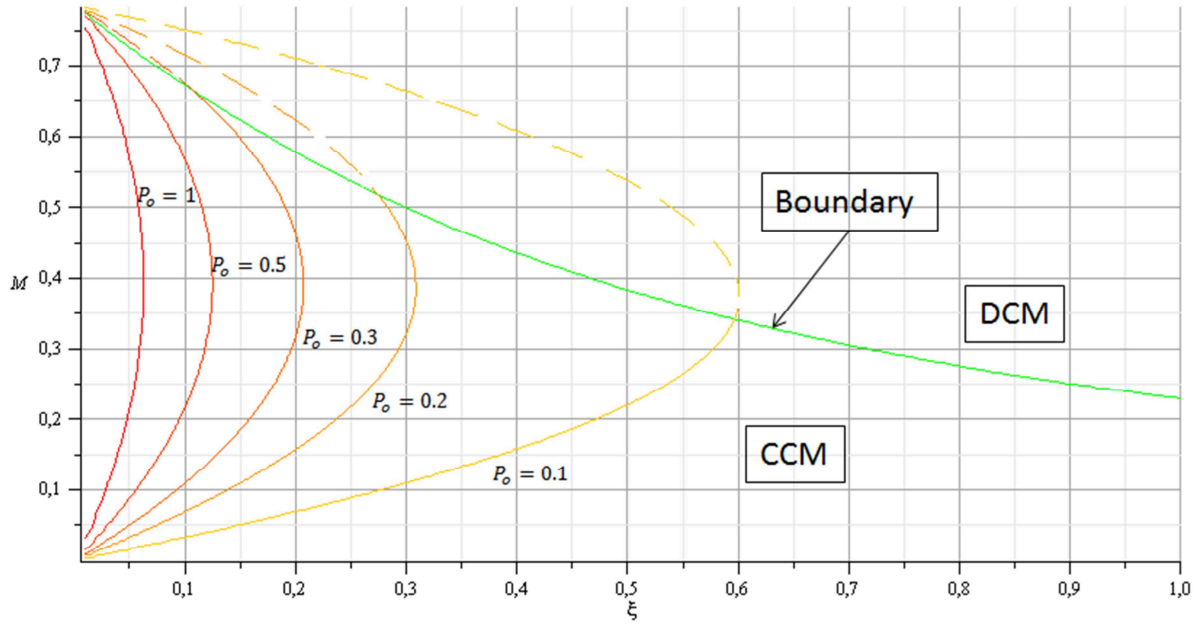


FIGURE 4.23 EXAMPLES OF P_o LEVELS AND CCM/DCM BOUNDARY

The boundary delimits the validity of the power curves and the equations till now used considered for the CCM mode. So above the limit, in the DCM zone, the expression of the power is no more valid and the power computation in the DCM must be performed.

- **Discontinuous Conduction Mode (DCM)**

In discontinuous conduction mode the current is no more a continuous function of time. It means that the AC conduction period is reduced and is no more a π interval as expressed before by the equations (4.28) and (4.29).

So the AC current in a period starts from zero at a generic angle θ_1 and returns to zero at the angle θ_2 being $0 < \theta_1 < \frac{\pi}{2}$ and $\frac{\pi}{2} < \theta_2 < \pi$. The solution equations of capacitor voltage and current, (4.26) and (4.27) respectively, still stands but in DCM other conditions apply.

In DCM not only the current is zero at the angle θ_1 but, being its derivative equal to zero too (null period), the following conditions can be stated:

$$i_c(\theta_1) = 0 \tag{4.36}$$

$$\sin(\theta_1) - v_c(\theta_1) - M = 0 \tag{4.37}$$

Which express that the current and the inductor voltage are equal to zero in θ_1 .

Equations (4.36) and (4.37) solved together, give the expression of the unknowns A and B in the capacitor voltage and current as a function of the angle θ_1 and of the damping factor ξ . Now the DC power in p.u. can be computed as before starting from the mean current:

$$I_o(\xi, \theta_1) = \frac{1}{\pi} \int_0^\pi i_c(\theta) d\theta \tag{4.38}$$

which leads to:

$$P_o(\xi, M, \theta_1) = I_o(\xi, \theta_1) \cdot M \quad (4.39)$$

The difference from the CCM is that in the DCM the current is constantly zero until the conduction interval begins at the angle θ_1 and ends at the generic angle θ_2 . So the current returns to zero in θ_2 and remains zero till the end of the period in π . So, in order to find the correct angles θ_1 and θ_2 the following additional conditions must be applied:

$$i_c(\theta_2) = 0 \quad (4.40)$$

and

$$v_c(\theta_1) = -v_c(\theta_2) \quad (4.41)$$

that counts for the conduction current symmetry for positive and negative peaks.

The solution for (4.40) and (4.41) leads to the values of θ_1 and θ_2 . The two cannot be solved analytically as the expressions are implicit equations in the variables θ_1 and θ_2 . So a numerical solution is performed and the results are used to compute for the DC power and the current expression. The equations and computations are reported in the Appendix B.

An example of a DCM current is shown in Figure 4.24:

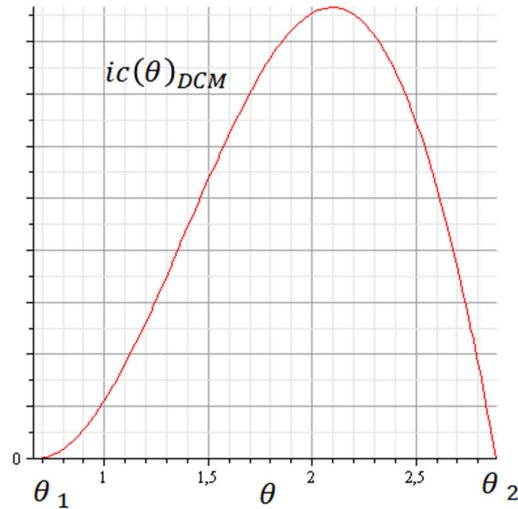


FIGURE 4.24 DCM CURRENT EXAMPLE $i_c(\theta)$

As can be noticed, the current starts in θ_1 and the conduction period finishes in θ_2 before the π interval completion as expected for the DCM.

As the equation in DCM must be solved numerically, the power level evaluation must be performed starting from the winding data that can be derived from the CCM operation. So the winding design can start from the CCM zone and then, thanks to the CCM/DCM boundary, the DCM zone can be explored to find the power transferred and the winding current obtained. In order to have a complete system view, a coil characteristic as a function of ξ and M must be obtained too.

- Coil Characteristic and Winding Data

In this section the winding characteristic curve as a function of ξ and M is derived. Crossing this curve with the power curves and the boundary line allow to design and evaluate the system performance.

The primary and secondary winding are inserted in a magnetic structure as shown in Figure 4.15 and hereafter reported.

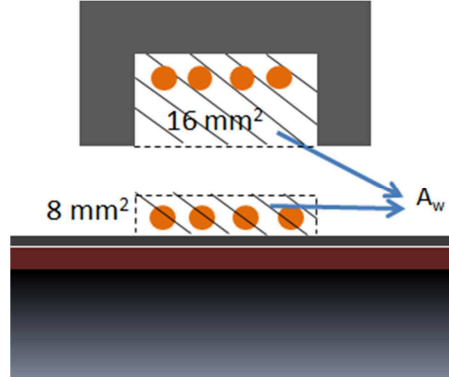


FIGURE 4.25 MAGNETIC STRUCTURE AREA

The area A_w that can be used for the windings construction is based on the structure dimensions reported in Figure 4.15. The values come not only from electro-magnetic considerations but also from mechanical and construction stability considerations always considering that the rotating part can reach the 300 Hz rotational frequency and the static part can be subjected to vibrations and mechanical stress.

Thus basing on the structure considered, the winding area is equal to 24 mm^2 and the copper net area coefficient α_{CU} can be evaluated equal to $\frac{1}{10}$. This is because resin cover and fastening tapes must be considered to obtain a reliable and long lasting structure and a first estimate can count on this coefficient. So the net area of the copper in the secondary coil is 0.8 mm^2

The coil secondary equivalent resistance can be obtained as follow:

$$R = R_1 \frac{N_2^2}{N_1^2} + R_2 = N_1 \rho \frac{l_c}{A_{c1}} \frac{N_2^2}{N_1^2} + N_2 \rho \frac{l_c}{A_{c2}} \quad (4.42)$$

where ρ is the copper resistivity ($1.7 \cdot 10^{-8}$ at 20°C), l_c is the coil average length, A_{c1} and A_{c2} are the conductor primary and secondary cross section area respectively.

If $\frac{2}{3}$ of the area A_w are assigned to the primary winding and $\frac{1}{3}$ of area is assigned to the secondary coil (as in the case here considered is 16 mm^2 against 8 mm^2) the primary and secondary cross section conductors area can be expressed as $\frac{2 A_w}{3 N_1}$ and $\frac{1 A_w}{3 N_2}$ respectively, meaning that all the available area can be occupied by the windings ; thus remembering the (4.42):

$$R = N_1 \rho \frac{l_c}{\frac{2 A_w}{3 N_1}} \frac{N_2^2}{N_1^2} + N_2 \rho \frac{l_c}{\frac{1 A_w}{3 N_2}} = \frac{9}{2} N_2^2 \rho \frac{l_c}{\alpha_{CU} A_w} \quad (4.43)$$

which expresses the conductors cross section area as a function of the winding area available for the secondary coil and for the primary one reported to the secondary side.

Thanks to this expression, the damping factor ξ can be expressed as:

$$\xi = \frac{R}{2L\omega} = \frac{\frac{9}{2} N_2^2 \rho l_c}{2 \omega N_2^2 (\lambda_{d1} + \lambda_{d2}) \alpha_{CU} A_w} = \frac{9 \rho D}{8 f (\lambda_{d1} + \lambda_{d2}) \alpha_{CU} A_w} = \xi_2 \quad (4.44)$$

D is the average diameter between the primary and secondary coils ($D = 195 \text{ mm}$), f is the excitation frequency and $(\lambda_{d1} + \lambda_{d2})$ is the leakage equivalent permeance reported on the secondary coil. As can be

noticed the damping factor is independent on the coil turn's number and so in a ξ - M plane the winding curve is represented with a vertical line which x-axis position is a constant value here called ξ_2 .

A more complete phenomenon description must compute for the skin and proximity effects that occur in the coil's turns. Here a precise computation is not derived as it would involve the evaluation of the leakage flux that intersects the secondary conductors and, due to the open-air magnetic structure of the secondary coil, is not a straight computation. Anyway the DC resistance per turn have been corrected with the skin-effect coefficient $k_a = 1.1$ that comes from the approximated formula in [12] when the wire diameter is less than 0.5 mm.

In order to proceed with the winding design, some parameters must be set. The desired primary voltage excitation level is $V_1 = 5 V$ while the desired maximum open circuit current is 2 A. So, basing on the (4.20) and on the permeance parameter of Table 12, with an excitation frequency of 30 kHz, the minimum primary coil turn's number is $N_1 = 4$ which yields to a primary open circuit current of 1.63 A thus respecting the limit imposed.

The damping factor, from the (4.44) and with the skin-effect coefficient k_a is $\xi_2 = 0.05$. Now a complete graph comprehensive of the power levels in p.u, the boundary line and the winding characteristic curve can be obtained as shown in Figure 4.26.

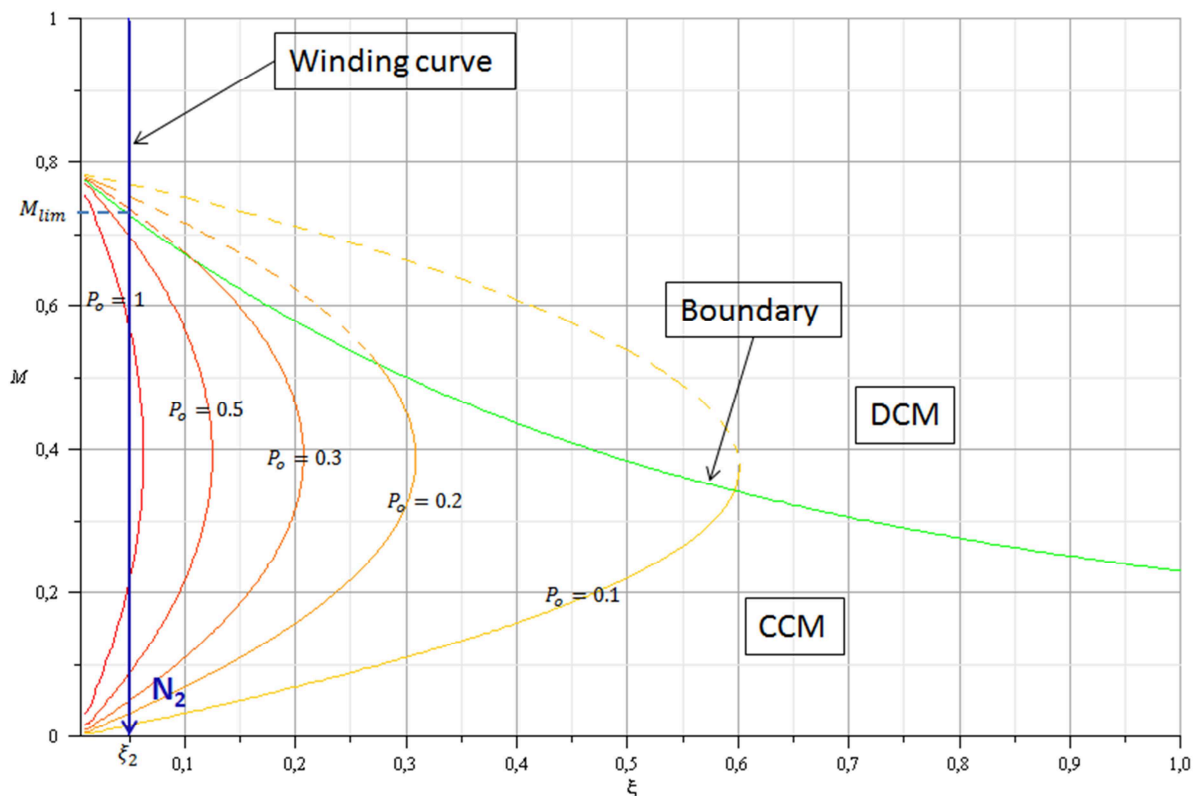


FIGURE 4.26 POWER, BOUNDARY AND WINDING GRAPH

The winding characteristic curve intersects different power curves and, basing on the coil turn's number N_2 , the system lays on the DCM zone or the CCM zone. As N_2 is increased, the value of M decreases as the two are inversely proportional as stated in the (4.45).

$$M = \frac{V_{DC}}{V_s} = \frac{V_{DC} N_1}{N_2 V_1} \quad (4.45)$$

As ξ_2 is an independent variable on the turn's number N_2 , the intersection between the winding curve and the boundary line gives the limit value of M for the CCM operation; as N_2 is increased, the working condition fall into the CCM zone.

Basing on this principle, the limit value of M for CCM operation can be called M_{lim} and for the system here considered turns out to be 0.73. The value of M_{lim} allows to compute for the turn's limit number for the CCM operation. So thanks to the (4.45) and fixing a desired DC-Bus voltage level $V_{DC} = 4$ V, the following is derived:

$$N_{2lim} = \frac{V_{DC} N_1}{M_{lim} V_1} = 4.4 \quad (4.46)$$

Thanks to the (4.46) the winding turn's number can be chosen as the next integer value ($N_2 = 5$) to fall into the CCM operation.

Once the secondary turn's number is fixed, all the other parameters can be evaluated as a consequence as reported in Table 13.

TABLE 13 SECONDARY WINDING PARAMETER

N_2	5
$L = N_2^2 (\lambda_{d1} + \lambda_{d2})$	$2.88 \cdot 10^{-5}$ H
$R = 2 \omega L \xi_2$	0.542 Ω
$C = \frac{1}{\omega^2 L}$	$9.76 \cdot 10^{-7}$ F
$V_s = \frac{N_2 V_1}{N_1}$	6.25 V
δ	-0.02
$M = \frac{V_{DC}}{V_s}$	0.64
$P_{DC} = P_b \cdot P_o$	5.42 W
$I_{DC} = I_b \cdot I_o$	1.36 A

Notice that the phase angle δ is small and negative and so a small phase shift toward the negative angle axis is expected.

Thanks to the geometric dimensions of the system and the pre-defined desired value, it's possible to compute the DC current and so the DC power given a secondary turn's number. Once ξ and M are defined, the expression reported in (4.27) allows the computation of the AC current $i_c(\theta)$ as shown in Figure 4.27

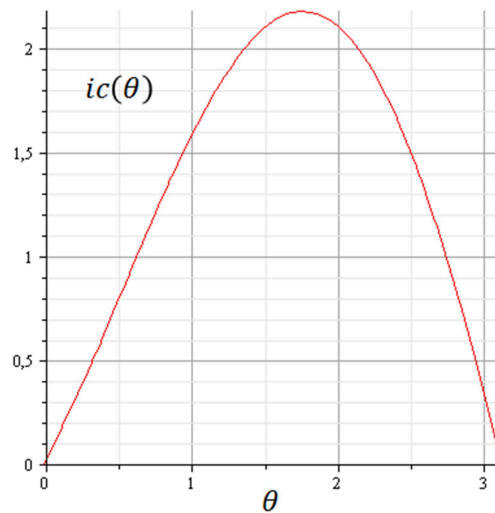


FIGURE 4.27 $i_c(\theta)$ FOR $N_2 = 5$

Another interesting result for the CCM operation is the computation of the transferred power as a function of the winding turn's number. The primary turn's number, as said before, is fixed to limit the open circuit current, while the transferred power level as a function of the secondary turn's number can be an interesting result useful for the system design.

The lower limit for the computation in CCM is given in the (4.46). Below that limit the all computations are no more valid as the system works in DCM zone and the numerical evaluation must be performed with the DCM equations. Figure 4.28 shows the transferred power as a continuous function of N_2 for CCM operation where the integer turn's number are marked.

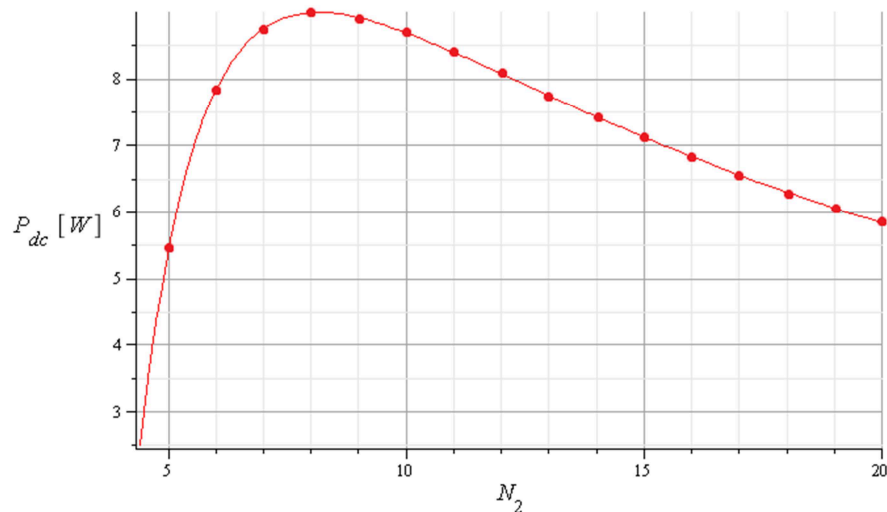


FIGURE 4.28 DC POWER VS. SECONDARY TURN'S NUMBER

As can be noticed, the DC transferred power function has a maximum for $N_2 = 8$ and then starts to decrease for higher turn's number. So, thanks to the analytical solution of the problem in CCM, it's possible to design the secondary coil looking at the turn's number limit and the DC transferred power. This way the efficiency of the power transmission system is clearly defined and the user, that design the windings based on this criteria, has an immediate feedback on the system performance.

The same computation can be extended to the DCM zone but in this case, as remembered before, the power should be computed numerically. So it's not possible to obtain the power as a continuous function of the turn's number. Instead, through the DCM computation procedure, the DC power is obtained for the integer turn's number. The winding geometric data as well as the primary data are the same. But in the DCM case the secondary turn's number is reduced in order to stay in the DCM zone.

The results from the DCM computation are reported in Table 14.

TABLE 14 DCM PARAMETER AND POWER COMPUTATION

$N_2 = 4$
$V_s = 5 \text{ V}$
$M = 0.8$
$L = 1.84 \cdot 10^{-5} \text{ H}$
$R = 0.347 \Omega$
$C = 1.53 \cdot 10^{-6} \text{ F}$
$\theta_1 = 0.651$
$\theta_2 = 2.915$
$P_{DC} = 0.71 \text{ W}$
$I_{DC} = 0.18 \text{ A}$

The DC power becomes zero near $N_2 = 3.21$, as can be computed with the algorithm for DCM operation, and so the data for $N_2 = 3$ cannot be obtained and the DC power as well as the rectified current are zero.

Thus completing the graph of Figure 4.28 with the DCM results, the Figure 4.29 is obtained:

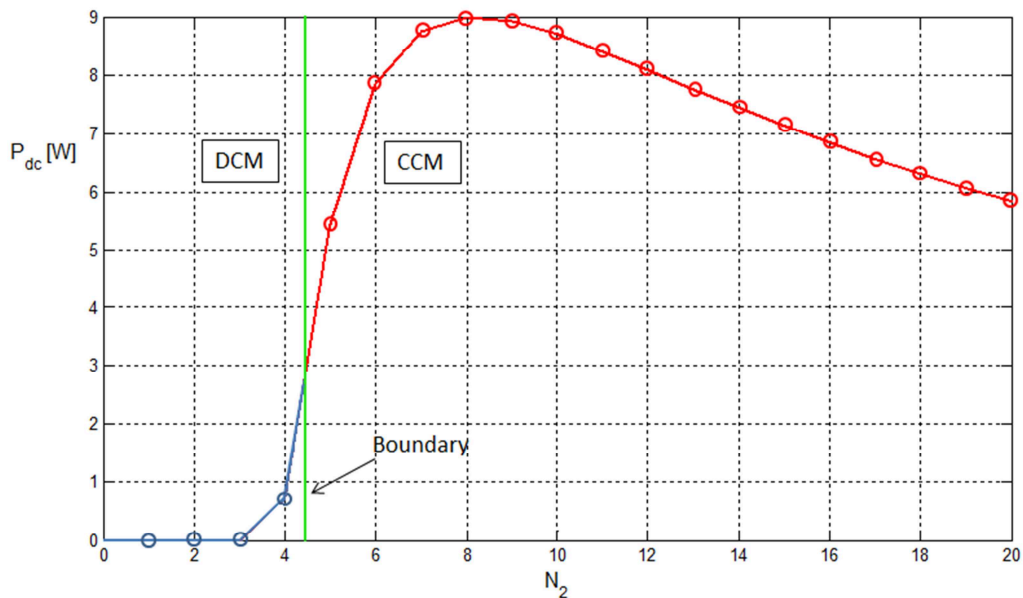


FIGURE 4.29 DC POWER FOR DCM/CCM OPERATION

The DCM/CCM boundary is outlined and, as the turn's number increases, the working condition fall into the CCM zone. Thanks to the numerical and analytical solution this meaningful result allows to evaluate the system efficiency given its geometrical dimensions and magnetic features.

4.2.2 NON-RESONANT WINDING

In this section the solution for the winding circuits is derived without the use of the series resonant capacitors. The geometrical dimension of the system are the same as well as the magnetic data but here the influence of the series capacitors on the power transfer efficiency is explored. The simplifying hypothesis of moving the magnetizing inductance and the primary series parameter at the secondary side is still considered to compare the two different solutions; the resonant one and the one without the series capacitors. Thus a comparison between the previous results and the new transferred power level without the secondary resonant capacitor is here performed.

Removing the capacitor on the secondary side, the circuit becomes as follows:

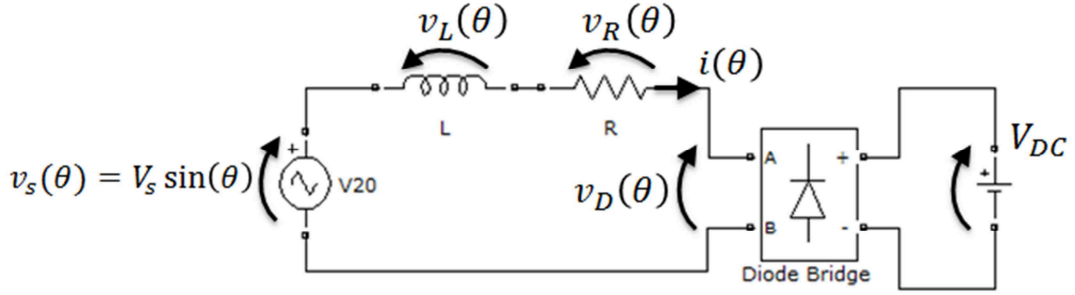


FIGURE 4.30 NON RESONANT SECONDARY WINDING

The components in the circuit assume the same meaning as for the circuit of Figure 4.20. The winding equivalent resistance and leakage inductance are outlined and the DC load is assumed to have a constant DC voltage.

The system's equation, always considering the positive current interval, now becomes:

$$V_s \sin(\theta) - v_R(\theta) - v_L(\theta) - V_{DC} = 0 \quad (4.47)$$

And for the voltage on the inductance:

$$v_L(\theta) = \omega L \frac{di(\theta)}{d\theta} \quad (4.48)$$

Now the (4.47) and (4.48) lead to:

$$V_s \sin(\theta) - Ri(\theta) - \omega L \frac{di(\theta)}{d\theta} - V_{DC} = 0 \quad (4.49)$$

As before the equation can be expressed in p.u. values. The base value here used are: $V_b = V_s$; $I_b = \frac{V_s}{R} 2\xi$;

$$P_b = \frac{V_s^2}{\omega L}$$

Always considering $M = \frac{V_{DC}}{V_b}$ and $\xi = \frac{R}{2L\omega}$ the system equation becomes:

$$\frac{d\tilde{i}(\theta)}{d\theta} + 2\xi\tilde{i}(\theta) = \sin(\theta) - M \quad (4.50)$$

Which is expressed in the same p.u. form as before. The general solution of the (4.50) is:

$$i(\theta) = A e^{-2\xi\theta} + \frac{1}{4\xi^2 + 1} (2\xi\sin(\theta) - \cos(\theta)) - \frac{M}{2\xi} \quad (4.51)$$

omitting the "tilde" notation.

The solution must distinguish between the CCM working condition and the DCM working condition.

- **Continuous Conduction Mode (CCM)**

As said before, the CCM condition to be imposed is:

$$i_c(\delta) = 0 \quad (4.52)$$

which counts for the zero crossing of the current at the angle δ .

Thanks to the (4.52) the constant A can be expressed as a function of δ , ξ and M :

$$A = e^{2\xi\delta} \left(\frac{1}{4\xi^2 + 1} (\cos(\delta) - 2\xi \sin(\delta)) + \frac{M}{2\xi} \right) \quad (4.53)$$

Now applying also the second CCM condition that is :

$$i_c(\delta + \pi) = 0 \quad (4.54)$$

the angle δ can be expressed as a unique function of ξ and M . The expressions are reported in the Appendix C.

Now, as before, it's possible to compute for the DC power in p.u. transferred to the DC Bus simply calculating the average current in a semi-period and multiplying it for M thus obtaining:

$$I_o(\xi, M) = \frac{1}{\pi} \int_{\delta(\xi, M)}^{\delta(\xi, M) + \pi} i(\theta) d\theta \quad (4.55)$$

for the average current and:

$$P_o(\xi, M) = I_o(\xi, M) \cdot M \quad (4.56)$$

for the DC power expressed in p.u. The DC power expressed in Watt [W] will be simply the power P_o multiplied by the reference value $P_b = \frac{V_s^2}{\omega L}$.

Also in this case it's possible to derive iso-power curves in the $\xi - M$ plane.

- **Continuous Conduction Mode / Discontinuous Conduction Mode Boundary**

As previously analyzed, the CCM/DCM boundary condition is the zero current value and the zero current derivative value for $\theta = \delta$. Referring to the (4.50) it leads to the following condition:

$$\sin(\delta) - M = 0 \quad (4.57)$$

being δ a function of ξ and M , the boundary condition can be represented in the $\xi - M$ plane too.

- **Discontinuous Conduction Mode (DCM)**

The solution for the DCM is the same of the (4.51) but here different conditions apply. As the conduction interval begins in a generic angle θ_1 and finish in a generic angle θ_2 , the following are stated:

$$i(\theta_1) = 0 \quad (4.58)$$

From which it's possible to derive the expression of the constant A as a function of θ_1 , ξ and M .

$$A = e^{2\xi\theta_1} \left(\frac{1}{4\xi^2 + 1} (\cos(\theta_1) - 2\xi \sin(\delta\theta_1)) + \frac{M}{2\xi} \right) \quad (4.59)$$

Also in θ_2 the current must be zero. So the following applies:

$$i(\theta_2) = 0 \quad (4.60)$$

For the zero derivative initial condition of the DCM, the equation is:

$$\sin(\theta_1) - M = 0 \quad (4.61)$$

The expressions (4.60) and (4.61) cannot be solved analytically and so, as before for the DCM, a numerical evaluation is performed and is reported in the Appendix D.

- **Coil Characteristic and Winding Data**

The coil characteristic as well as the dimensional data remain the same like the resonant case so that the current, the power level and the performance of the two systems can be directly compared. The value of ξ_2 , being a function of the geometric and magnetic data, remains the same as before. This way the winding curve in the $\xi - M$ plane is still a vertical line at $\xi_2 = 0.05$.

The primary winding data used for the resonant winding case are used also for this analysis and they are summarized in Table 15.

TABLE 15 WINDING DATA

V_1	5 V
N_1	4
λ_{d1}	$8.9 \cdot 10^{-7}$ H
λ_{d2}	$2.7 \cdot 10^{-7}$ H
A_w	24 mm ²
D	0.195 mm
α_{CU}	0.1
ξ_2	0.05
V_{DC}	4 V

The power curves, the boundary line and the coil characteristic curve are shown in Figure 4.31.

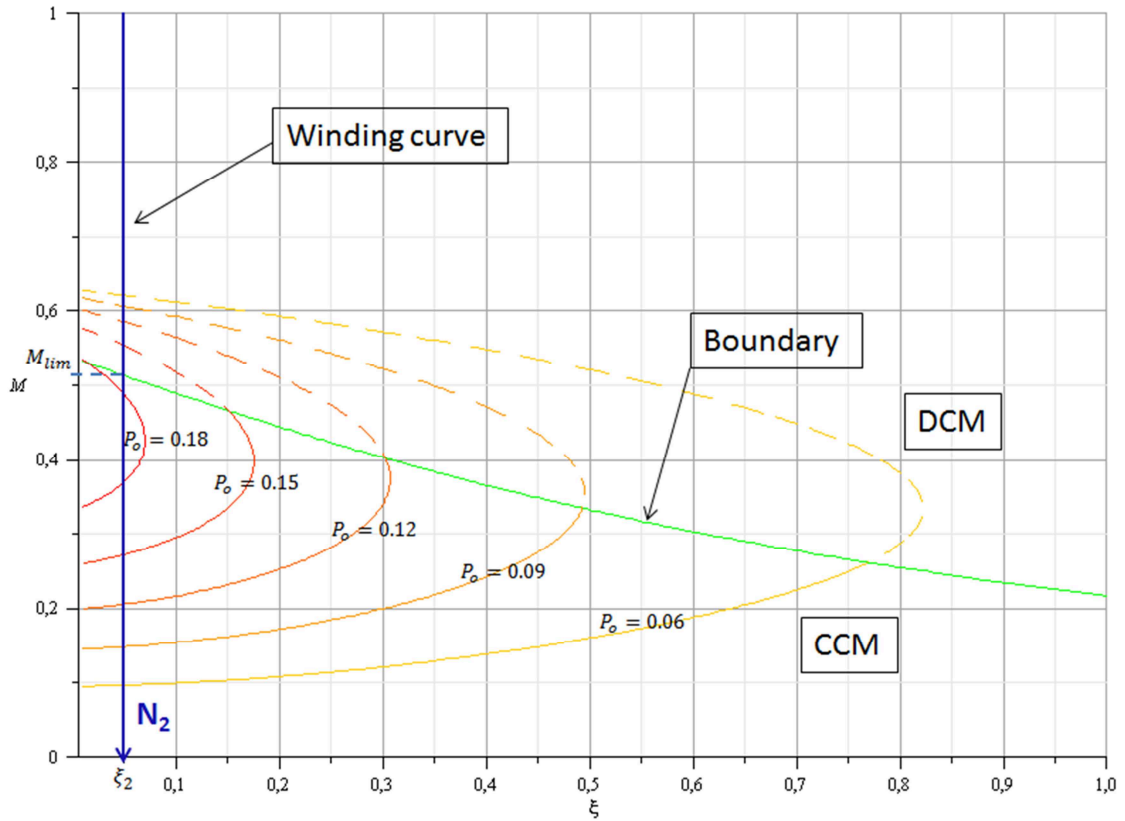


FIGURE 4.31 POWER, BOUNDARY AND WINDING GRAPH FOR NON-RESONANT CASE

As before the upper limit M_{lim} is computed which corresponds to a minimum turn's number N_{2lim} , as in the (4.46), to bring the working condition in CCM. In the non-resonant winding, M_{lim} is equal to 0.51 and so N_{2lim} is 6.27. Thus the integer number of turns to be in the CCM is 7.

To compare the two systems, the expression of the power as a function of the turn's number for the non-resonant winding, considering the CCM/DCM boundary, is derived as before and is shown in Figure 4.32.

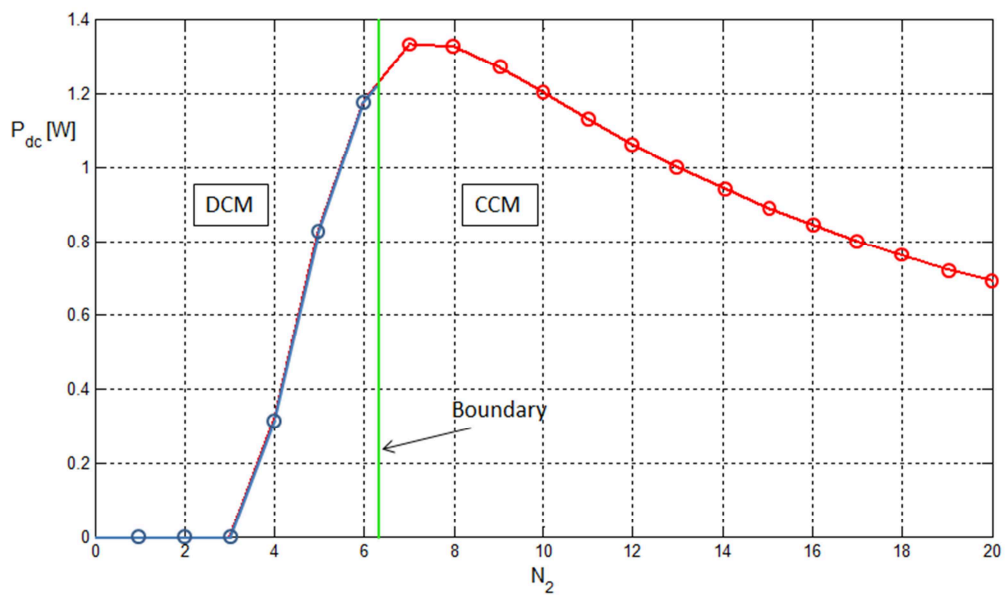


FIGURE 4.32 DC POWER FOR CCM/DCM NON-RESONANT WINDING

As can be noticed, the DC power level is far below the transferred power in the resonant winding case. Not only there's the need of more turns to fall into the CCM zone (7 against 5), but also the maximum power is 1.33 W against 9 W so the 85.2% less.

The efficiency of the resonant secondary winding is quite evident in comparison with the R-L winding. More power can be obtained with less coil's turns thanks to the series resonant capacitor.

- **Simulation Results**

The results obtained with the analytical computation (for CCM) and numerical evaluation (for DCM) have been verified through the Matlab Simulink® SimPowerSystem tool.

A circuit like the one of Figure 4.33 has been simulated and the AC current and DC power are obtained. To compute for the non-resonant condition, the capacitor is removed and the circuit is directly linked to the diode bridge.

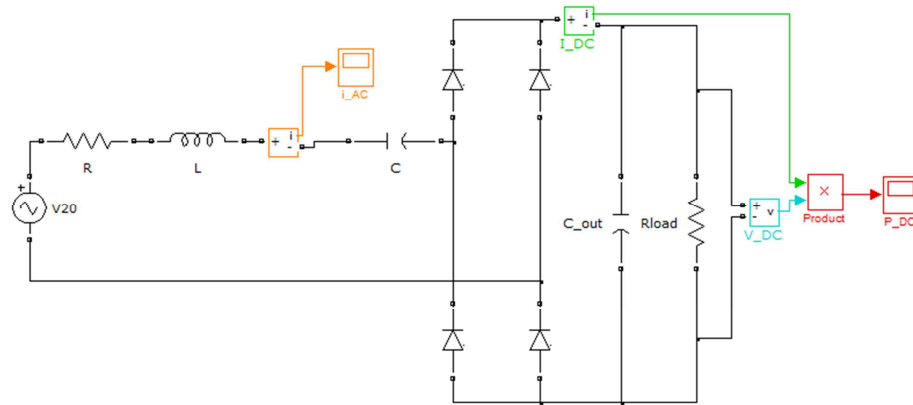


FIGURE 4.33 SIMULATED CIRCUIT

The DC side of the diode bridge is composed by a high value DC-Bus capacitance (0.1m F) in order to have a very small voltage ripple and a load resistance. The resistance value is derived from the desired DC voltage level ($V_{DC} = 4 V$) and the computed DC power transferred as stated in (4.62).

$$R_{load} = \frac{V_{DC}^2}{P_{DC}} \tag{4.62}$$

First the secondary turn's number has been chosen equal to 7 to obtain the CCM working condition for both the resonant and non-resonant circuits. The winding data are reported in Table 16 :

TABLE 16 SIMULATED WINDING DATA

$N_2 = 7$
$V_s = 8.75 V$
$M = 0.46$
$\xi_2 = 0.05$
$L = 5.65 \cdot 10^{-5} H$
$R = 1.063 \Omega$
$C = 4.98 \cdot 10^{-7} F$ (for resonant winding)

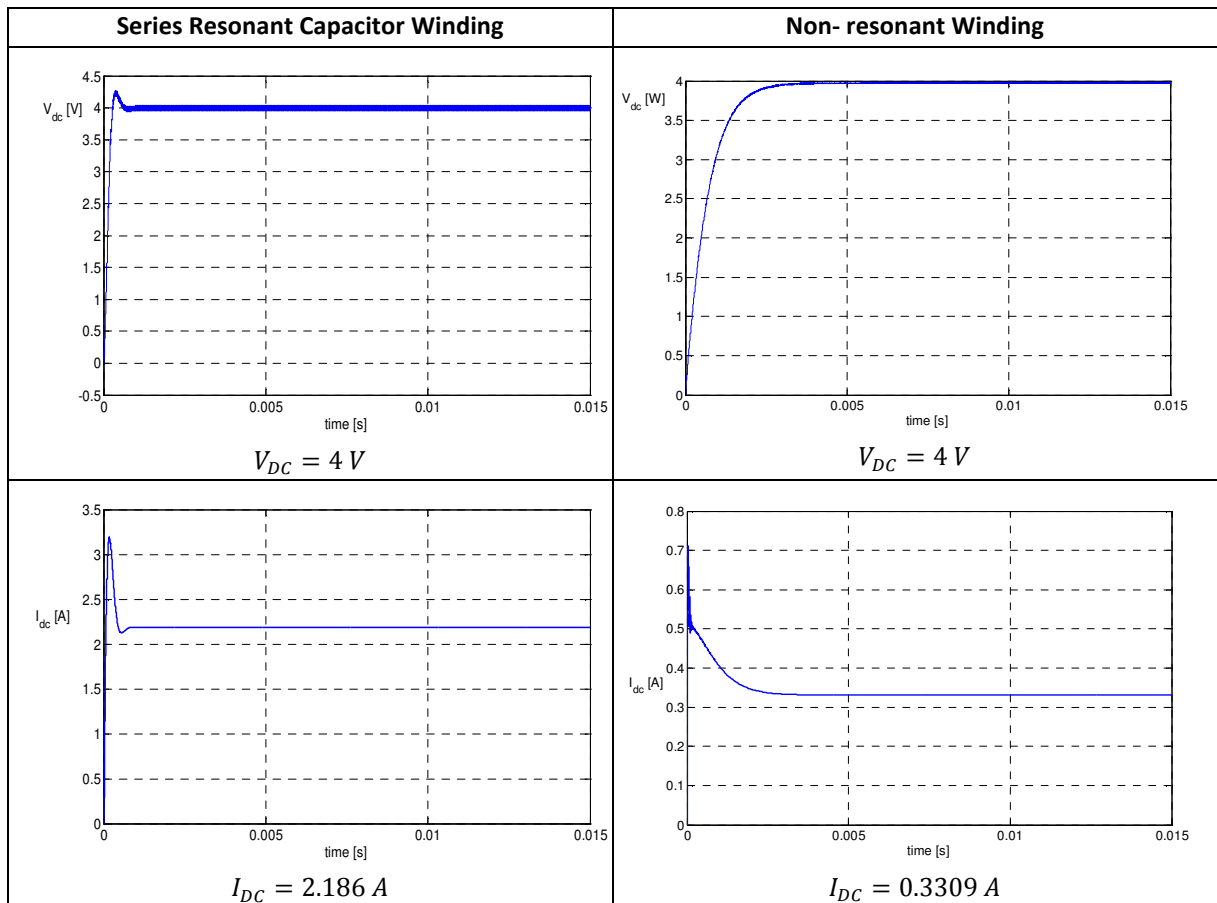
Then the DC current and the DC power are computed for the resonant and the non-resonant circuits thanks to the analytical and numerical expressions with the procedure described above. The results are reported in Table 17.

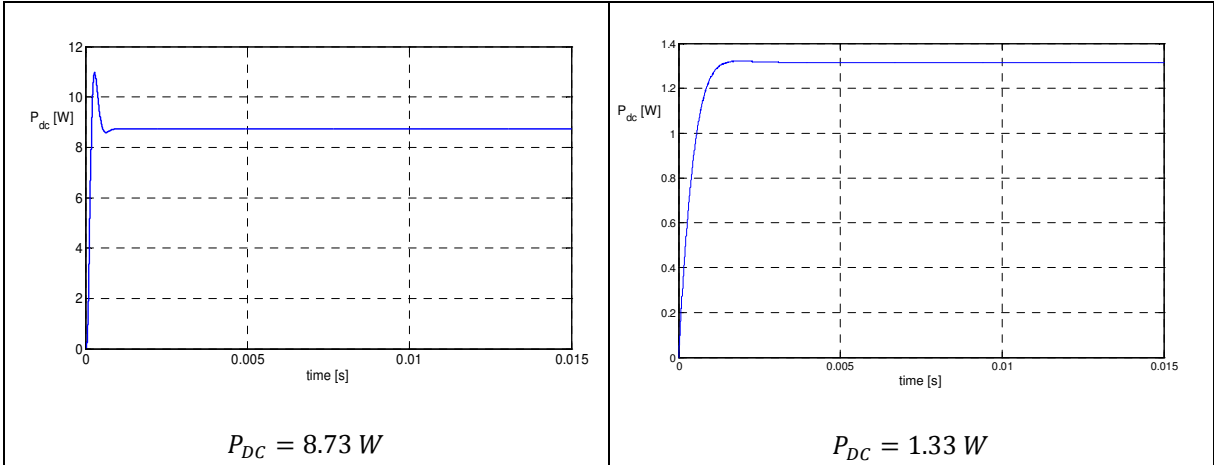
TABLE 17 DC POWER AND CURRENT FROM ANALYTICAL COMPUTATION

Series Resonant Capacitor Winding	Non- resonant Winding
$I_{DC} = 2.19 \text{ A}$	$I_{DC} = 0.33 \text{ A}$
$P_{DC} = 8.75 \text{ W}$	$P_{DC} = 1.33 \text{ W}$

The values derived from the analytical computation are now compared with the simulation result as shown in Table 18.

TABLE 18 SIMULATION RESULTS

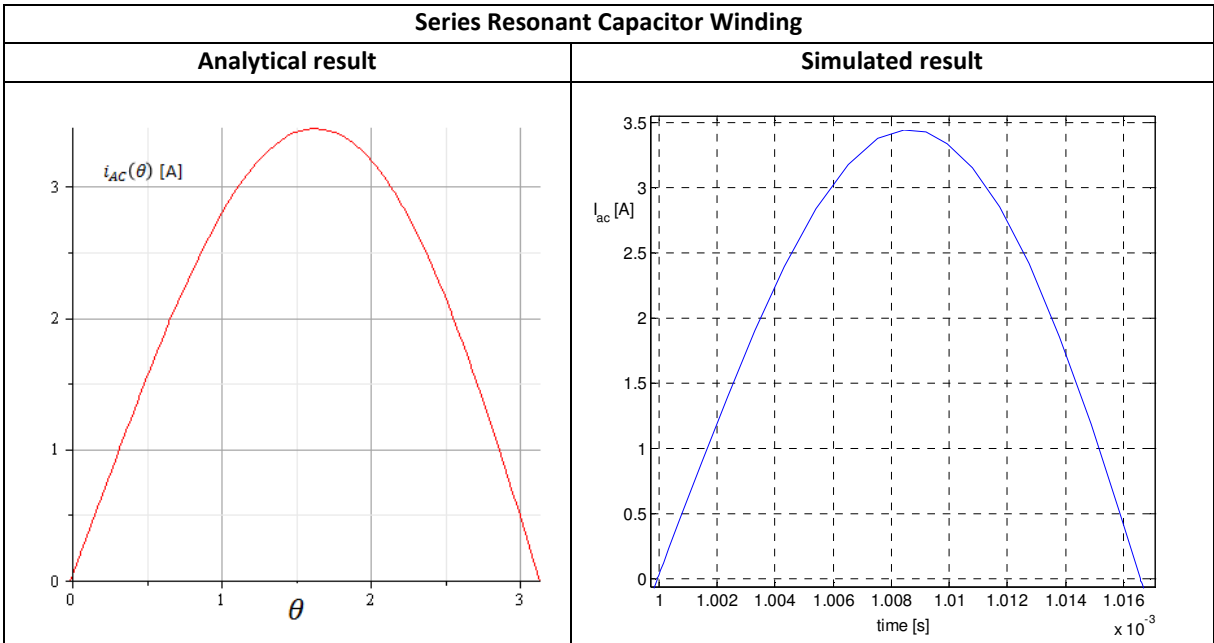




As can be noticed, the SimPowerSystem simulation steady state values display negligible errors in comparison with the analytical results derived from the system equations solution. The initial transients are due to the DC-Bus capacitor charge, then the steady state is reached. The diode considered in the simulation are ideal, with no series voltage drop and with negligible influence of the snubber circuits.

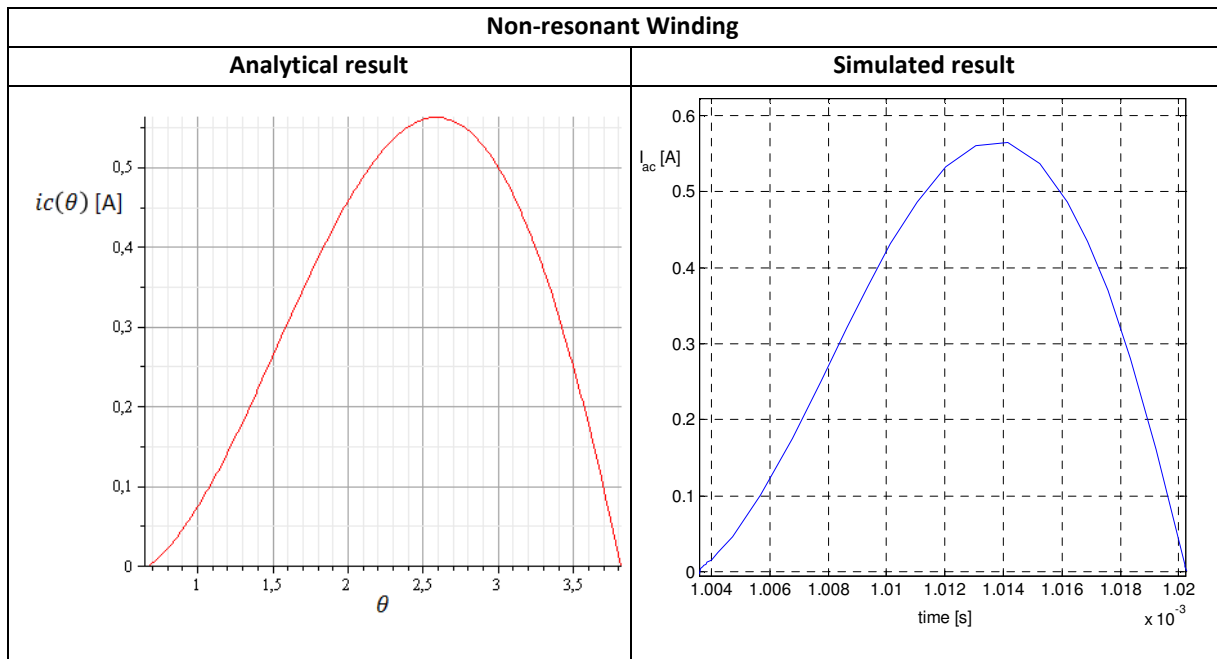
As a further investigation the AC current computed with the equations is compared with the simulated current. The results are presented in Table 19 and Table 20.

TABLE 19 ANALYTICAL AND SIMULATED RESULTS FOR RESONANT WINDING



The two results are in very good agreement. The one from analytical computation is expressed as a function of the angle θ , while in the simulation environment the x-variable is time and a half period (from 1ms to 1.016ms) is shown. The same comparison is done for the non-resonant winding thus obtaining:

TABLE 20 NUMERICAL AND SIMULATED RESULTS FOR NON-RESONANT WINDING



Also for the non-resonant winding, the results are in very good agreement.

For the DCM working condition, as said before, the analytical expressions of the current and the power is not achievable and a numerical solution is performed to find the start and finish conduction angles and so the transmitted power as shown in Table 14 and in Figure 4.29.

As a conclusion of this section, the analytical study of the electric circuit for the telemetry system power feeding can be a very comprehensive tool that allows the detection of CCM/DCM boundary condition and the expression of the transferred power as a function of the secondary turn's number.

This study relies on some simplifications and FEM computation to derive the magnetic data necessary for the winding design. As the telemetry axle power unit has a precise place inside the axle box, the geometry of the system is subjected to the mechanical dimensions of the train and to the system parts constrains. This way the geometry of the power unit can be evaluated quite well and so the magnetic data for the primary and secondary winding design can be derived. A high frequency induction power feeding for axle telemetry system is a new feature that, at the time this work has been written, is going to be adopted to enhance the security on the new generation of high speed trains.

4.3 CONTACTLESS ENERGY TRANSFER USING RECTIFYING ANTENNAS

In this section the solution of a contactless energy transfer using antennas and radio frequency electromagnetic waves will be briefly explored. This study is a part of the work presented in the 2012 Symposium on Electromagnetic Compatibility (APEMC) [13], and comes from a different solution considered in order to power the telemetry system without contacts and to keep a relative high distance from the rotating axle. So the merits of an antenna power system are the distance that can be adopted between the receiving antenna and the emitting antenna and the embedding possibility for the receiving antenna in the resin cover of the axle due to the small antenna's dimensions. Obviously the disadvantage of this solution is the low power level that can be collected from a radio frequency transmission system.

Thus the base concept of this system is a couple of antennas, one on the static part of the bogie and the other fastened on the rotating axle. The first antenna emits some power through electromagnetic waves at high frequency and the second antenna, being excited by this waves, converts the radio frequency power into DC power. This kind of antennas are called rectifying antennas or rectennas.

There are a lot of studies in literature regarding the rectennas and their application for the energy harvesting [14]-[16]. This topic has become wide spread since the energy gathering in the surrounding environment, without extra energy consumption, was explored. The chance of collecting energy from the environment in particular contexts, as the cities, is nowadays widely explored mainly in the context of the green energy and the energy efficiency [19], [20].

Another field of interest for the energy harvesting is the distributed sensors power feeding [17], [18]. The new improvements in the technology brought the sensor dimensions and power consumption smaller and smaller. So not only it is possible to put a dedicated sensor very near to the measured apparatus or in some cases directly inside it (tires, concrete, engines, turbines, generators, ..), but also the power consumption for the measure, acquisition and data transmission is quite small. In some cases wireless energy feeding and data reading are necessary as the position of the sensor is not approachable. This, as for many other situations, is the case of the axle telemetry system and data transmission here considered. As said in the previous chapters, the strain gage and the measuring apparatus rotate with the axle and the data must be acquired onboard.

The challenge of this solution is that all the environment considered for a train axle telemetry system is very severe as all the components surrounding the antennas are iron and steel made. So the consideration for the transmission system design in the free space are here not valid and the reflection phenomenon can affects the power transmission. Another important aspect is that the receiving antenna is placed on a rotating axle. Thus not only there is a metal ground plain near below it but also, more important, a single antenna faces the static antenna just for a small period of time throughout a complete axle rotation.

The case considered for the system analysis is an iron cylinder on which is placed an antenna in order to receive energy from the static emitter system.

The iron surface of the shaft and two iron surfaces, one of the train wheel and the other of the brake disk, delimit the space of the antenna and form a sort of cavity in which the receiver antenna should work. The layout is displayed in Figure 4.34.

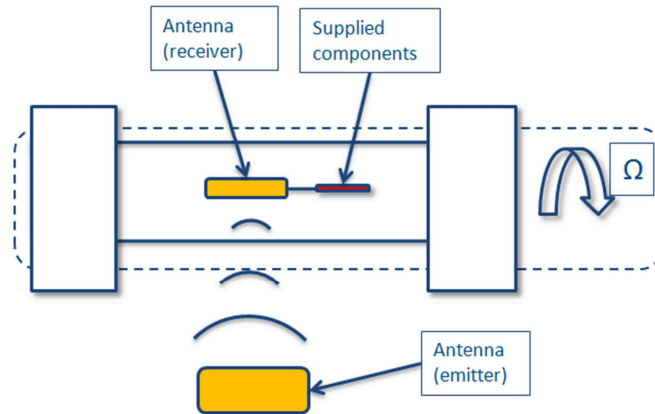


FIGURE 4.34 ANTENNA TRANSMISSION SYSTEM

The emitting antenna is placed on a static reference system nearby the shaft and can be placed at least at 0.5m downside the train coach. The receiving antenna has the purpose of catching the electromagnetic waves and converting them in a supply voltage for the rotating components in order to properly power the telemetry system. Both the receiving antenna and the electrical components are placed on the shaft surface and so they rotate with it.

The particular adverse environment here considered put some serious constraints regarding the wave propagation modeling and the antennas design. A 3D simulator can help in predicting the antenna gain in different situations and the energy transfer efficiency.

As the emitted waves are converted to DC power for supplying the rotating components, a rectifying antenna system should be used in this case. The principle of these antennas is to capture wide frequency band electromagnetic waves and to convert them directly to DC level. More than one antenna can be used combined together to enhance the power collected. This turns out to be very useful in this case since placing the antennas all around the shaft can help in having a continuous power delivery to the rotating system avoiding the shadowing of the iron. As shown in Figure 4.35, the combination of more than one antenna can be used to charge a small energy storage system (battery, capacitors) and then to power the strain gages and communication system on demand.

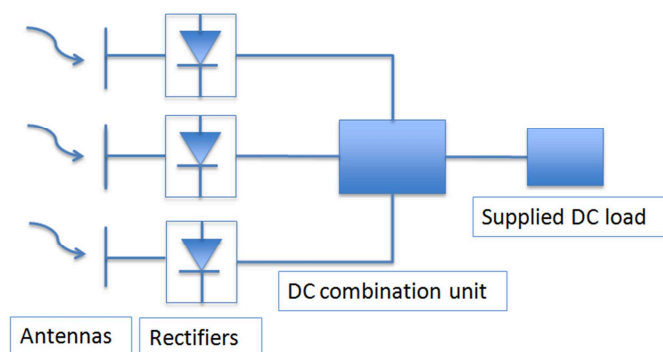


FIGURE 4.35 PRINCIPLE OF OPERATION OF RECTIFYING ANTENNA.

Rectennas directly converts the induced RF voltage from the external antenna to a DC voltage supply. Usually very low direct voltage drop diodes are used to rectify the induced voltage without losing too much energy and

they are set across the antenna conductor and the ground plane. A DC combination unit allows to collect the different inputs and to regulate the DC voltage for the supplied load [7].

Let's suppose that every single antenna can transfer the DC Power P_1 . Using multiple antennas placed around the shaft results in the situation of Figure 4.36.

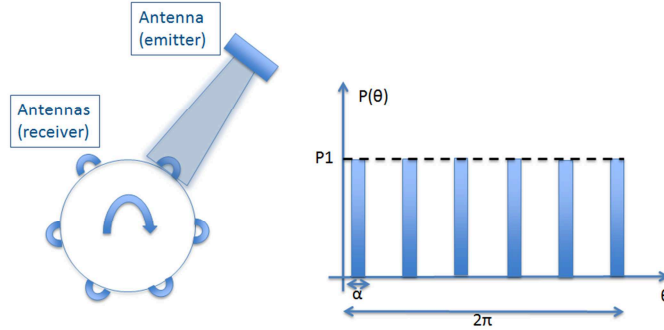


FIGURE 4.36 ANTENNAS DISTRIBUTION AND POWER DELIVERY.

The delivered power from each antenna on the rotating shaft is added at the load resulting in an average power P_{avg} for every turn:

$$P_{avg} = \frac{1}{2\pi} \int_0^{2\pi} P(\theta) d\theta = N \cdot \frac{\alpha}{2\pi} \cdot P_1 = N \cdot \frac{w}{\pi D} \cdot P_1 \quad (4.63)$$

where N is the number of distributed antennas along the surface of the shaft, α is the portion of the periphery occupied by each receiving antenna, w the width of each antenna and D the diameter of the shaft. This system design requires a high directivity for the emitting antenna and multiple receiving antennas combined together to enhance the average power collected to the load.

Considering P_1 the maximum power delivered for each antenna, P_{inc} the RF incident power equal to $5\text{mW}/\text{cm}^2$, A_{eff} the effective area for each antenna equal to 10 cm^2 , η the DC conversion efficiency equal to 0.5 (preventive low value), the following can be written:

$$N = \frac{P_1}{P_{inc} \cdot A_{eff} \cdot \eta} \quad (4.64)$$

If a certain average power is desired, called P_{avg} , combining the (1) and (2) lead to the maximum power P_1 :

$$P_1 = \sqrt{P_{avg} \cdot P_{inc} \cdot A_{eff} \cdot \eta \frac{\pi D}{w}} \quad (4.65)$$

Let's suppose a desired average power equal to 200mW . With the antenna width $l = 1\text{cm}$ and $D = 190\text{mm}$, the maximum power delivered results $P_1 = 0.55\text{W}$ and so the number of the antennas on the shaft (next integer number) $N = 22$.

The data here considered should be compared with the simulation data in order to fit the desired average power with the correct antenna's number.

As said before, a DC power storage unit can be used to collect the proper amount of energy before making a measurement. This technique can be used if the delivered power for each antenna is small and a certain amount of time is needed to reach the desired energy level. The measurement process would be discontinuous

but for the case here considered is not a problem since the measurement campaigns can be as long as a train travel on the railway.

The rectifying stage is built using diodes for converting the RF sine wave induced in the antenna into DC voltage. One of the main characteristics of the diodes is the Bias voltage necessary for their operation. When the voltage level of the induced RF sine wave is much higher than the bias voltage, this is not a problem but in the case of low incident power the voltage drop in the diodes can be predominant. The choice of a Schottky diode is convenient for their low threshold and their low junction capacitance.

Another important aspect to consider when designing a rectenna is the working frequency. At low frequencies, below 1 GHz, a high gain antenna tends to be quite large. On the other hand the available power at a certain distance from the emitting antenna in the free space decreases with the increasing of the frequency. A frequency range between 1GHz and 5GHz gives a good compromise between dimension and attenuation of the power.

A High Frequency filter between the receiving antenna and the rectifier ensures the matching of impedance between the two components for optimal power transfer capacity. The output DC filter levels the voltage waveform by attenuating the high frequency harmonics coming from the RF signal and from the diode rectifier. As the structure considered and the phenomenon involved are quite complicated, the analysis will be performed thanks to a 3D Finite Element (FEM) analysis simulation and the power received from the shaft antenna will be computed.

So, firstly, a 3D simulation was performed to model the shaft structure and one antenna placed on it. The antenna chosen is a patch antenna designed for 2.4GHz frequency with edge feeding. The geometric data of the antenna selected are displayed in Figure 4.37 and reported in Table 21.

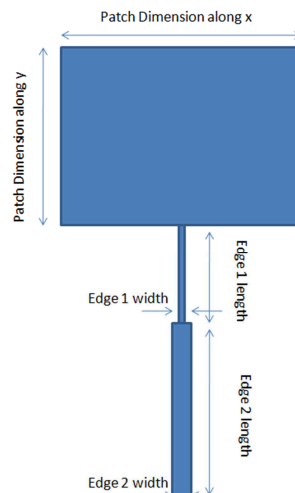


FIGURE 4.37 PATCH ANTENNA DESIGN

TABLE 21 ANTENNA DATA

Patch Dim. along x	49.41mm
Patch Dim. along y	41.36mm
Substrate thickness	62mil
Edge 1 width	1.89mm
Edge 1 length	23.42mm
Edge 2 width	4.85mm
Edge 2 length	38.07mm

The whole system modeled is shown in Figure 4.38. The shaft and the two side boundaries are well displayed. The patch antenna is placed above the shaft.

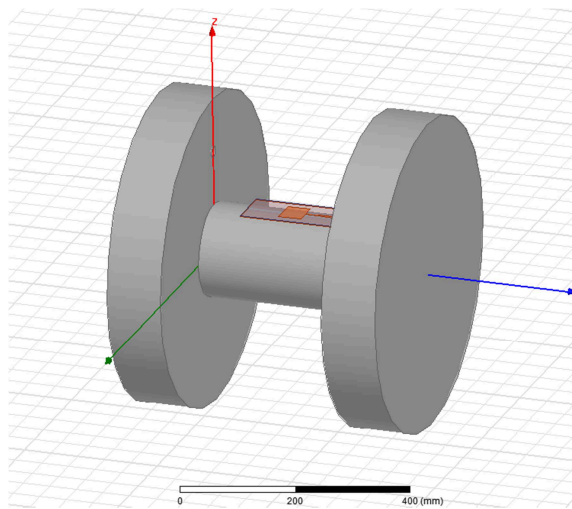


FIGURE 4.38 SHAFT AND ANTENNA SIMULATION MODEL

A frequency sweep analysis has been performed starting from 1.2 GHz till 3.6GHz and different plots are derived. In Figure 4.39 the scattering parameter S11 clearly shows the main features of the patch antenna selected that is high directivity and narrow bandwidth.

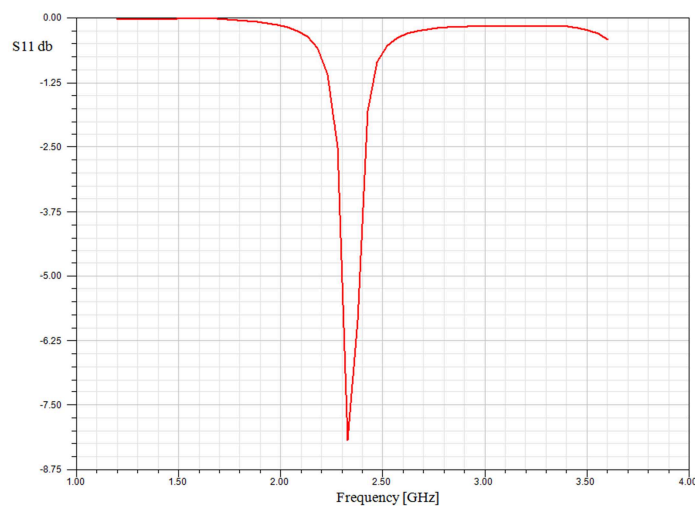


FIGURE 4.39 S11 ANTENNA RESULT

In Figure 4.40 two 3D-plots of the antenna gain are shown. The 4.40a) refers to the environment described in Figure 4.38 so with the iron shaft and the side boundaries. The second one, 4.40b), is the 3D gain of solely the patch antenna in the free space. Is evident the gain modification due to the adverse environment. However at the same time the gain in the z-axis direction is a little bit increased (darker red) leading to a better gain in the emitting antenna direction.

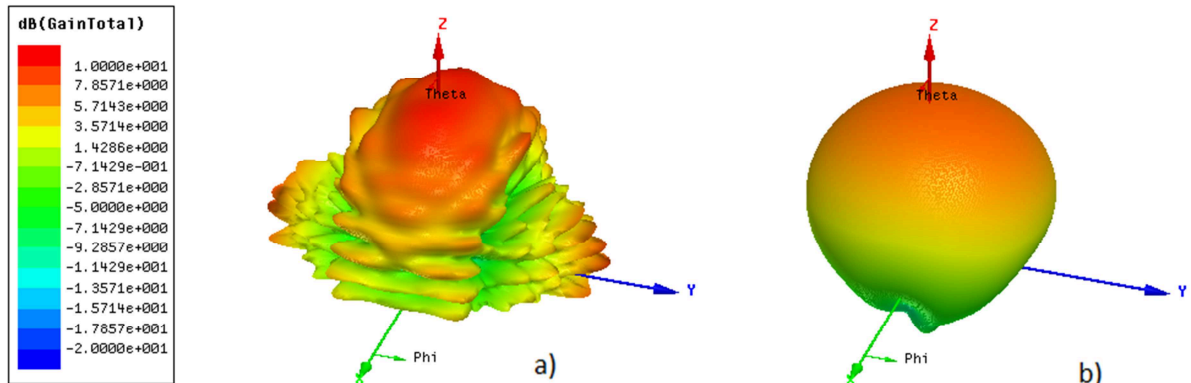


FIGURE 4.40 3D GAIN OF THE ANTENNA IN DIFFERENT ENVIRONMENTS

The gain distortion due to the iron shaft can also be seen in Figure 4.41 where the gain is plotted as a function of Theta, for Phi equal to 0 deg and 90 deg.

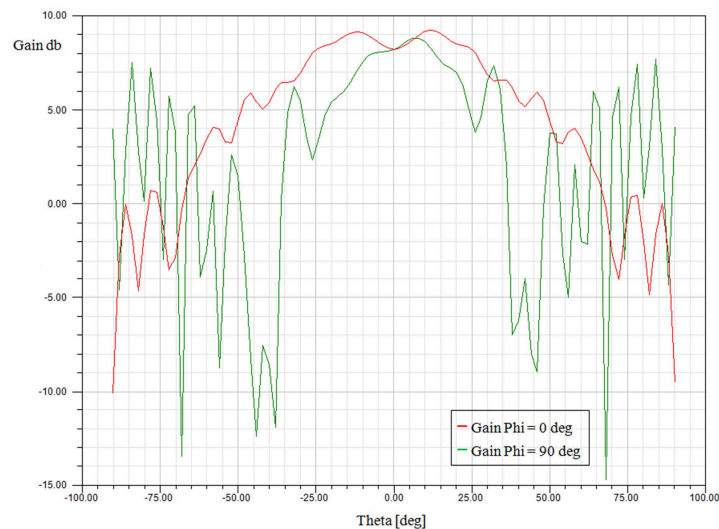


FIGURE 4.41 ANTENNA GAIN AS A FUNCTION OF THETA FOR Phi = 0 deg, AND 90 deg.

The strong gain ripple for Phi=90 deg. is actually due to the reflective iron surface of the two supports which form a boundary for the antenna emission path.

Now the simulation is modified to include also the emitting antenna. Another patch antenna, like the first one, has been placed 0.5m above it and the S_{12} parameter computed. In this way an emitting-receiving two ports system is modeled. The result is shown in Figure 4.42.

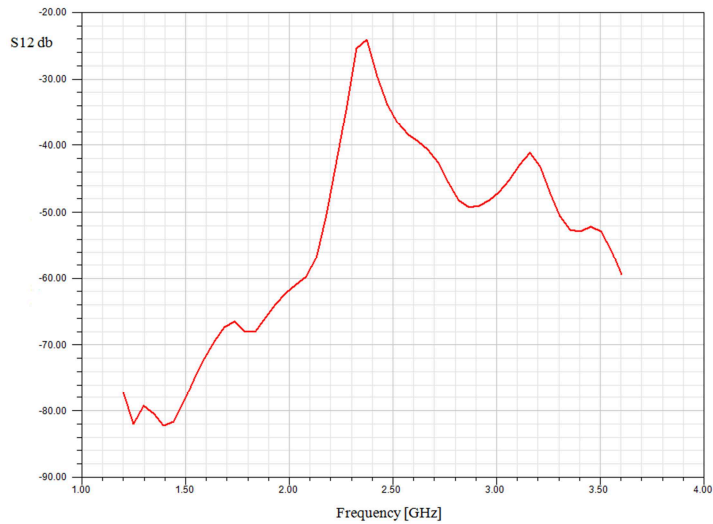


FIGURE 4.42 S12 PARAMETER OF THE TWO PORTS SYSTEM

The power entering the emitting antenna through the port has been computed applying a 10 V incident voltage and it's been evaluated to be 0.518 W. Considering S12 parameter equal to -24db as resulting from the simulation, the received power is equal to 8.21 μ W. So a very small amount of power can be collected from this two ports antenna design. Further analysis are required to improve the system efficiency.

Another two ports transmission system has been tested and it's made of a horn antenna on the static part and a 5.8 GHz patch antenna on the shaft resulting in smaller antenna dimensions. The horn antenna has a high directivity and a better gain and directly enlighten the patch antenna. This solution is shown in Figure 4.43.

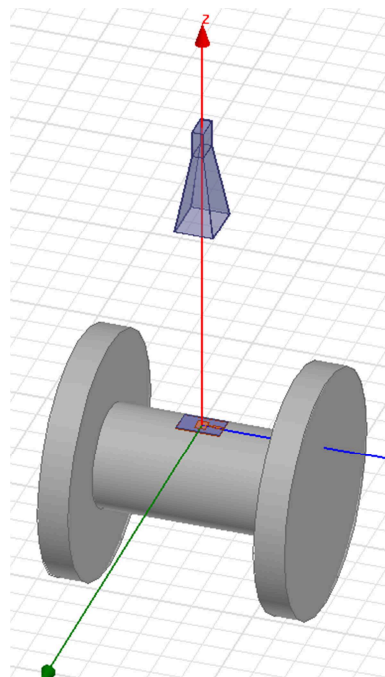


FIGURE 4.43 HORN AND PATCH ANTENNAS

As before, the S12 parameter is computed. Its maximum value is higher than before and mostly important it shows a wide band feature between 5.5 GHz and 6 GHz.

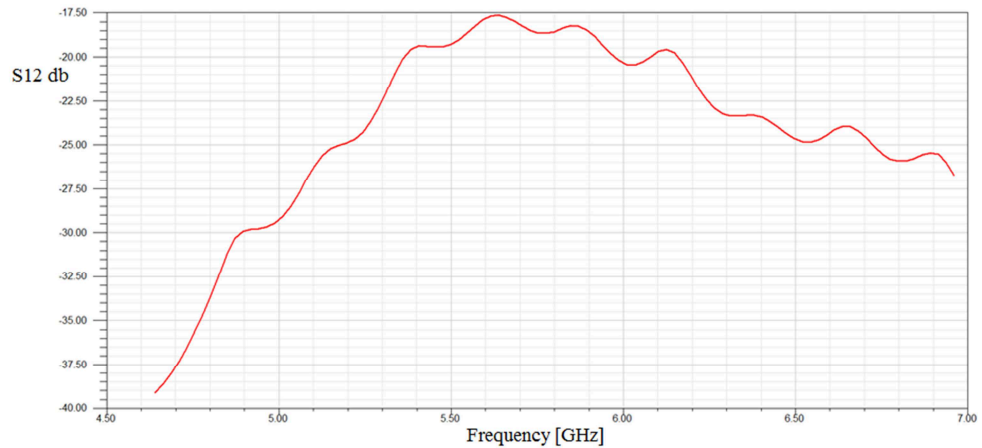


FIGURE 4.44 HORN AND PATCH ANTENNAS S12

As the maximum value results equal to -17.5 dB, always considering 0.518 W for the radiated power, the received power is equal to 0.164 mW. Thus a very small amount of power can be transferred through a two port antenna system in comparison with the other energy transmission techniques. More antennas should be placed on the shaft to enhance the transferred power and different antenna design can be explored to improve the transmission efficiency.

The analysis here presented is far from being an exhaustive analysis of the electromagnetic waves propagation and the antenna design which is an important and wide field of the electrical engineering.

The consideration here derived are used to roughly evaluate and compare the antenna transmission system with the other solutions analyzed. The final conclusion is that a two port antenna system can be considered as an energy transfer system for many cases even if an energy storage device and a discontinuous measurement procedure are expected and a sufficient time for energy recharging is needed.

- **Laboratory Tests on an Energy Harvesting System**

A wireless energy harvesting system was tested in the laboratory to measure the RF transferred power between two antennas. The radio waves are generated at 950 MHz and a receiving patch antenna rectifies and gather energy for a measuring board equipped with temperature, light and humidity sensors. The communication between sensors and the access point is at 2.4 GHz using 802.15.4-compliant radios.

The working principle is the same described before. A transmitter antenna with a receiving antenna and a DC conversion stage for micro-controller power feeding. The measured signals from the sensors are acquired and transferred wirelessly to the access point.

The transmitter is a 3W, 8dBi, 915MHz antenna while the receiver is a 6 dBi gain directional patch antenna.

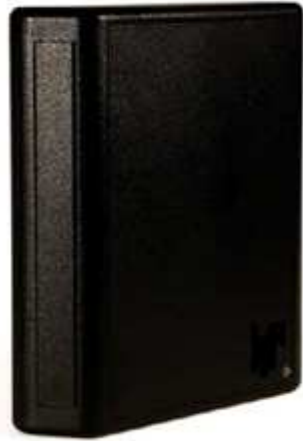


FIGURE 4.45 TRANSMITTER ANTENNA



FIGURE 4.46 PATCH RECEIVER ANTENNA

Although the omnidirectional feature can be useful for the axle application, the directional antenna has a higher gain and is more compact so it can be better fasten upon the shaft. So the directional antenna is tested placing the receiver antenna nearby a metal cylinder at the distance of 20 mm and the transmitter antenna at different distances. The DC load is made of a 100 Ω resistance and a LED. The DC storage unit controller enable the power transmission on the load when the DC voltage on the DC storage capacitor has reached a pre-defined threshold and interrupt the load excitation when the voltage goes below a lower limit. The transferred power is computed measuring the average current in the load.

The influence of the rotation angle on the power transmission is also investigated turning the antenna and the metal cylinder into 4 angular position with respect to the transmitter. The position 0 corresponds to the patch antenna facing directly the transmitting antenna.

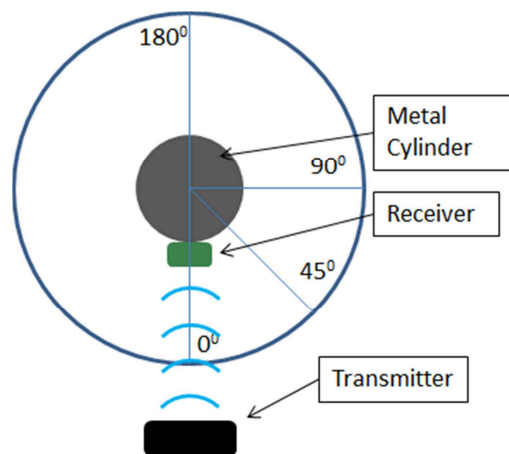


FIGURE 4.47 ANGULAR POSITION TESTS

In the first case analyzed the distance between the two antennas is 100 mm. The data are reported in Table 22.

TABLE 22 TRANSFERRED POWER AT 100mm

Current [A]	Angle[deg]	Power [W]
$3.60 \cdot 10^{-3}$	0	$1.296 \cdot 10^{-3}$
$1.90 \cdot 10^{-3}$	45	$3.61 \cdot 10^{-4}$
$1.40 \cdot 10^{-4}$	90	$1.96 \cdot 10^{-4}$
0	135	0
0	180	0

The power that can be transferred is significant for the zero degree position where the antenna is directly pointed toward the transmitting system. As the antenna is rotated, the power drastically decreases as expected for this directional antenna.

In the second case, the distance has been increased to 200mm and the data are reported in Table 23.

TABLE 23 TRANSFERRED POWER AT 200mm

Current [A]	Angle[deg]	Power [W]
$3.80 \cdot 10^{-3}$	0	$1.44 \cdot 10^{-3}$
$2.0 \cdot 10^{-3}$	45	$4 \cdot 10^{-4}$
0	90	0
0	135	0
0	180	0

As can be noticed, the transferred power for the first two position is a little increased meaning that at that distance the storing unit can work regularly and feed the load. The reflected waves upon the iron shaft less disturb the antenna transmission. At the other angular positions, the received power is zero.

In the last case the distance between the iron cylinder and the transmitter is set to 300mm and the experimental data are reported in Table 24,

TABLE 24 TRANSFERRED POWER AT 300mm

Current [A]	Angle[deg]	Power [W]
$1.2 \cdot 10^{-3}$	0	$1.4 \cdot 10^{-4}$
$9.0 \cdot 10^{-4}$	45	$8.1 \cdot 10^{-5}$
0	90	0
0	135	0
0	180	0

Increasing so far the distance, the delivered power at the load becomes smaller as expected. At 300mm the power for the zero angle position is near to the one computed in the simulation with the horn and patch antennas. In that case the distance considered was higher (500mm) but the transmitting antenna was supported by a horn structure that better concentrate the electromagnetic waves toward the shaft antenna.

This results confirm the prediction made, thanks to the simulation tool, that through the RF antennas the transferred power is very small and an energy storage system should be used to collect enough energy for measuring and acquire the desired signals.

4.4 ENERGY TRANSFER ON ROTATING SHAFTS USING PM PRINTED-WINDING MACHINE

This chapter investigates the energy transfer amount of an alternative solution consisting in a small Permanent Magnet Synchronous Generator (PMSG) which is directly mounted on the train shaft. This new solution has been presented during the XXth International Conference on Electrical Machines (ICEM) [21]. In particular, the winding is linked to the shaft whereas the permanent magnet array is arranged on a rolling bearing. A suitable counter-weight prevents the revolution of the PM array during the shaft rotation. This way, the whole system can be encapsulated on the shaft without requiring any external mechanical connections nor constraints. However the small available space makes the design of such a PMSG a challenging task. The maximum power that can be delivered through this solution will be analyzed considering also the rectifying stage for the DC telemetry system powering.

The system consists of a PMSG built within a bearing structure mounted on the shaft. A small part of the energy involved in the shaft rotation is transferred through the PMSG to the electrical components mounted on the shaft like the windings, the DC conversion unit and all the components involved in the strain measurement. This solution allows to transfer the energy directly on the rotating parts without using external-linked devices nearby the shaft. A sketch of the whole structure is shown in Figure 4.48.

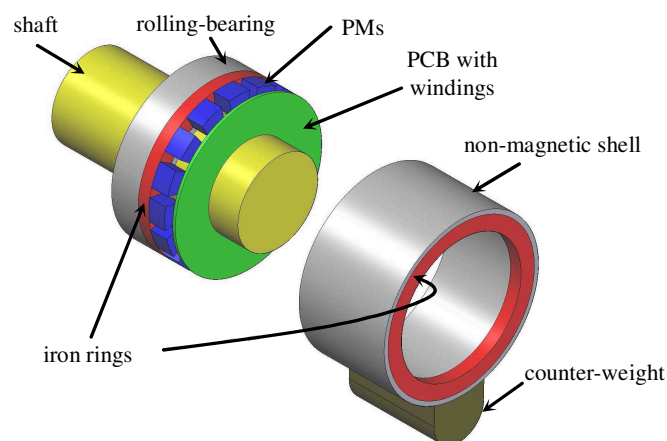


FIGURE 4.48 EXPLODED SCHEME OF THE PMSG MOUNTED ON THE SHAFT

The whole machine is built based on a bearing that can be placed in the middle of the train axle, between the braking disks. As the axle rotates, the bearing internal track rotates with it. A very thin disk, made of resin, can be fastened to the internal track in order to have a solid structure.

Thanks to the Printed Circuit Board (PCB) technology, it is possible to realize a very compact winding on this disk mounted on the shaft. This disk rotates with the axle and so do the machine's windings. Being the windings the rotating part, the permanent magnet should be kept still. The magnet array is linked to an iron ring placed upon the bearing external track. In order to avoid the external track rotation, due to the internal frictions, a counter-weight should be added on the external covering shell. This way the gravity force tends to keep the weight below and as a consequence the magnet array is still with respect to the rotating windings.

The two iron rings provide a better magnetic flux enclosure behind the magnets from one side and behind the PCB disk to the other side and the whole structure is closed by a non-magnetic shell.

The features of the selected bearing are chosen considering a 160mm diameter train axle and are reported in Table 25 and in Figure 4.49.

TABLE 25 BEARING FEATURES

D[mm]	240
D ₁ [mm]	213
d[mm]	160
d ₁ [mm]	186

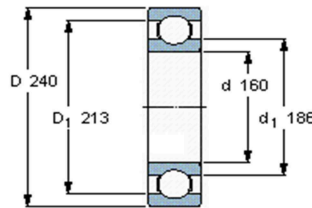


FIGURE 4.49 BEARING CONSIDERED IN THIS CASE STUDY.

A schematic radial section of the machine is shown in Figure 4.50: the PMs only fill the ring defined by the bearing external track, and the printed winding is located on a PCB in the area facing the PMs. The external track height is 13 mm. Consequently the area for the printed-winding construction should be restricted to this region.

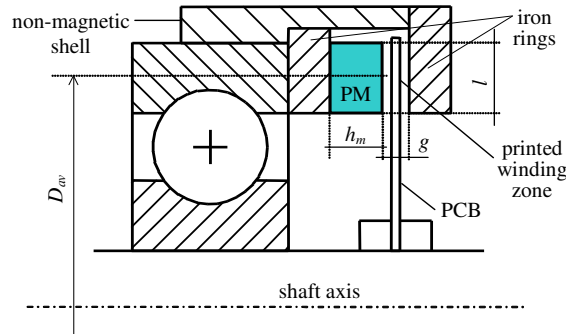


FIGURE 4.50 SCHEMATIC RADIAL SECTION OF THE MACHINE

The external track of the bearing supports the PM array through a suited back-iron ring. The closure of the magnetic path is through a second iron ring which is connected to the external track by a non-magnetic shell. The printed winding technology allows to have a very robust winding construction in a very small space. The main advantage of this solution is that the machine's rotor is iron-less and so it's very light. As a consequence the winding structure is not affected by the high centrifugal force. The drawback is that an iron-less construction means a small flux density in the air-gap and so a reduced electromotive force. A noticeable PM height in order to achieve a proper flux density level in the air-gap is then required.

Printed windings are frequently used in hard-disk drives as the slot-less armature coil reduces the cogging torque as well as the inertia [26]-[28]. Another drawback of printed windings is that they are characterized by a low volume of copper and then also by a high resistance. A scheme of the stator windings is shown in Figure 4.51: the diamond-like shape [26] of the coil's turns and the double layer disposition allow to place the active

conductors close each other, without overlapping. In fact, the left and the right side of each coil are placed on the top and on the bottom layer respectively. Figure 4.51 shows, as an example, the detail of a single coil: suited “vias” at each internal and external corner establish the electrical connection between the two conductor of a coil as well as between two adjacent coils. Three groups of q coils are placed in each pole pitch with a suitable shift, in order to obtain a three phase winding. Thus this could be considered as an ordinary three-phase double layer winding with just one conductor per layer and per slot. However, in this case, the “slot” is a purely fictitious (positional) notion. By considering this analogy, it is useful to indicate with the symbol q the number of coils per pole-phase. In order to maximize the Electromotive Force (EMF), a full-pitch winding is considered.

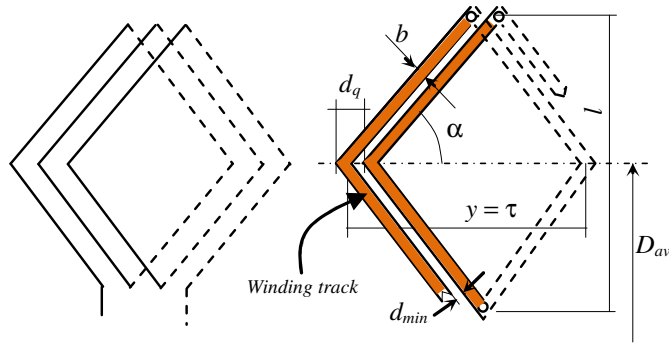


FIGURE 4.51 WINDING DETAIL AND RELATED GEOMETRICAL DIMENSIONS.

Focusing on the winding construction, two distances d_q and d_{min} can be defined: d_q is measured between the external corners of two adjacent parallel strips, whereas d_{min} is the minimum distance between two adjacent strips. Due to the low voltage levels, the value of d_{min} is mainly related to the PCB manufacturing process. Since the main geometrical dimensions l and D_{av} are chosen according to the shaft diameter and to the available space, the stator winding is completely defined by the number of poles p and the coils per pole-phase q . The strip width b can be related to p and q by considering that the total number of turns of the three phase winding must exactly fill the perimeter of the average circumference, i.e.:

$$3pq \frac{b + d_{min}}{\sin \alpha} = \pi D_{av} \Rightarrow b = \frac{\pi D_{av}}{3pq} \sin \alpha - d_{min} \quad (4.66)$$

Moreover, the angle α is given by:

$$\alpha = \text{atan} \left(\frac{pl}{\pi D_{av}} \right) \quad (4.67)$$

From (4.66) and (4.67) the following expression of b arises:

$$b(p, q) = \frac{\pi D_{av}}{3pq} \sin \left(\text{atan} \left(\frac{pl}{\pi D_{av}} \right) \right) - d_{min} \quad (4.68)$$

The higher are p and q , the smaller is the width b and the higher will be the winding resistance. The thermal exchange efficiency limits the current density in the strip and then put a constraint on the minimum value of b . Some indicative values for b in PCBs can be found in specific Nomographs [27]. However for an accurate evaluation, a thermal model of the machine should be developed. In any case, b cannot be reduced below a minimum value depending on the PCB manufacturing technology.

The PMSG is represented by its steady state equivalent circuit in Figure 4.52. E is the rms value of the EMF, R and L are the phase resistance and the synchronous inductance, $\omega = 2\pi f_m \cdot p/2$ is the electrical circular frequency.

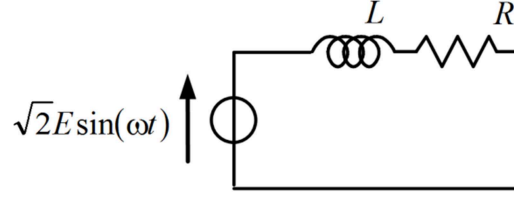


FIGURE 4.52 PHASE EQUIVALENT CIRCUIT OF THE PMSG

In order to estimate the EMF, the axial flux machine can be handled as a linear machine by considering the circumference at the average diameter D_{av} [29]. The distribution of the magnetic induction in the air-gap of such equivalent 2D arrangement can be analytically evaluated by formulating the related field problem in terms of vector potential and by using the variable separation technique [30]. The fundamental (p poles) amplitude of the magnetic flux density in the middle of the air-gap can be written as:

$$B_1 = \frac{\frac{4}{\pi} B_r \sin\left(a_m \frac{\pi}{2}\right) \cosh\left(\frac{\pi}{\tau} \frac{g}{2}\right) \tanh\left(\frac{\pi}{\tau} h_m\right)}{\frac{\mu_{rev}}{\mu_0} \sinh\left(\frac{\pi}{\tau} g\right) + \cosh\left(\frac{\pi}{\tau} g\right) \tanh\left(\frac{\pi}{\tau} h_m\right)} \quad (4.69)$$

where B_r and m_{rev} are the residual flux density and the reversible permeability of the permanent magnet material, g is the sum of the mechanical air-gap and the PCB thickness, b_m is the magnet width, τ is the pole arc pitch defined as: $\tau = \pi D_{av}/p$ and a_m is defined as $a_m = b_m/\tau$.

The computation of the EMF must consider that the flux density distribution crosses a rhombic coil area resulting in the scheme displayed in Figure 4.53. Considering the geometry of the winding and the reference axes x and z as in Figure 4.53, the fundamental amplitude of the magnetic flux linked with a single turn is given by:

$$\varphi = 4 \int_0^{\tau/2} \int_0^{lx/\tau} B_1 \sin\left(\frac{\pi}{\tau} x\right) dz dx = \frac{4}{\pi^2} B_1 l \tau \quad (4.70)$$

hence the coefficient $4/\pi^2$ counts for the winding shape.

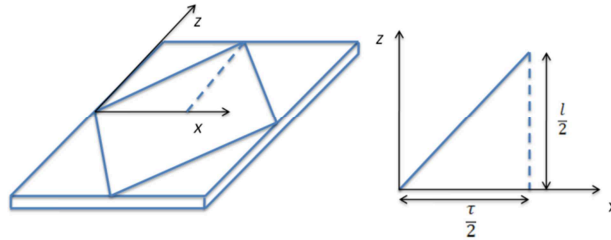


FIGURE 4.53 WINDING TURN REPRESENTATION FOR THE FLUX COMPUTATION

The field fringing at the external and internal circumference boundaries can be taken into account by a reduction coefficient. The rms value of the phase EMF E is calculated as in an ordinary distributed winding by considering that here the number of turns N_{ph} in series per phase is $N_{ph}=2 \cdot q \cdot p$. In fact, in order to increase the EMF at very low speed, no parallel paths are used. Thus:

$$E = \sqrt{2}\pi f N_{ph} k_w \Phi = \sqrt{2}\pi f_m p^2 q k_w \Phi \quad (4.71)$$

where k_w is the winding factor for the main harmonic (p poles), f is the electrical frequency and f_m the mechanical frequency ($f = f_m \cdot p/2$). Since here a full pitch winding is considered, k_w reduces to the distribution factor:

$$k_w = \frac{1}{2q \sin(\pi/6q)} \quad (4.72)$$

The average length of a winding turn is:

$$l_{turn} = \frac{l}{\sin \alpha} = l \left(\sin \left(\operatorname{atan} \left(\frac{pl}{\pi D_{av}} \right) \right) \right)^{-1} \quad (4.73)$$

Hence, the phase winding resistance is given by:

$$R = \rho_{cu} \frac{2pq}{sb} l_{turn} \quad (4.74)$$

where s is the copper strip thickness.

Finally, a rough estimation of the synchronous inductance L can be achieved by considering the air-gap permeance related to an equivalent distributed winding with the same p , q and with straight coil sides along l . In this case, the permeance must be halved in order to take into account the rhombic shape of the actual coils.

Thus:

$$L \cong \frac{1}{2} \frac{3\mu_0}{\pi^2} k_w^2 \frac{(2pq)^2}{p} \frac{\tau l}{g_{eq}} \quad (4.75)$$

being:

$$g_{eq} = g + \frac{\mu_0}{\mu_{rec}} h_m \quad (4.76)$$

A more accurate computation calls for the solution of the magnetic field in the air-gap according to the stator current distribution [31]. This aspect is not considered in this work because the low copper volume in the machine produces a resistance which is remarkably higher than the synchronous reactance. Thus the interaction of the generator with the electronic converter interface will be predominantly affected by the stator resistance.

Figure 4.54a) shows the electronic converter interface: the machine is connected to a three-phase diode rectifier whose capacitive DC-bus feeds a switching dc-dc converter.

As previously mentioned, a low machine EMF at low speed and a significant winding resistance are expected. On the other hand, the DC/DC converter cannot properly operate if the input voltage decreases below a minimum value around few volts. For these reasons, using an accurate steady state equivalent model of the diode rectifier, including the diode voltage drops, is mandatory in order to evaluate the actual power which can be extracted from the PMSG. Such a model is here deduced.

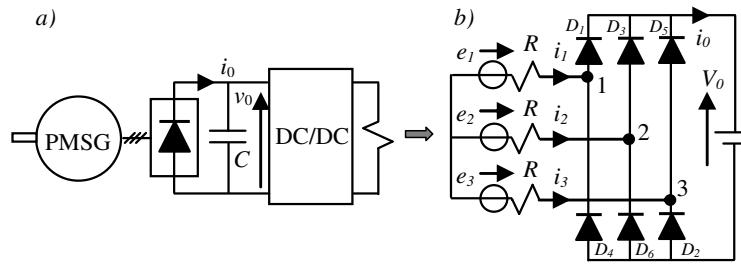


FIGURE 4.54 a): ELECTRONIC CONVERTER INTERFACE, b) SIMPLIFIED EQUIVALENT MODEL

The DC capacitance is considered to be high enough to maintain a rather constant DC voltage V_0 , so that the DC-bus can be modeled by a voltage generator. However, even under the assumption of an infinite DC-bus capacitance, diode rectifiers are quite difficult to model by a purely analytical approach. A three phase diode rectifier feeding a constant voltage dc-bus exhibits four modes of operation. They are often defined with the number of diodes which are simultaneously conducting in the switching patterns, i.e.: 2/0, 2/3/2/0, 2/3, 3/3 [32], [33]. Steady state analytical models in an explicit form have been formulated only for modes 2/0 and 3/3 [34], [35]. The range of existence of mode 2/3/2/0 is very small [32]. Moreover, even if it should be the most desirable due to the low harmonic content of the ac currents, the operation in mode 3/3 requires a high AC inductance [34]-[35], whereas the AC impedance of the considered machine is dominated by the stator resistance, especially at low speed. Thus in this application, due to the low value of the machine inductance, only the modes 2/0 and 2/3 are expected. This suggests to neglect the machine inductance in order to deduce a simplified steady state model of the rectifier. The resulting equivalent circuit of the whole system is shown in Figure 4.54b). The diode voltage drops are taken into account by a threshold forward voltage V_D and, if the case, by adding a differential resistance R_D to the phase resistance R .

- **Mode 2/0.**

An example of the switching pattern in mode 2/0 is shown in Figure 4.55 together with some current and voltage waveforms.

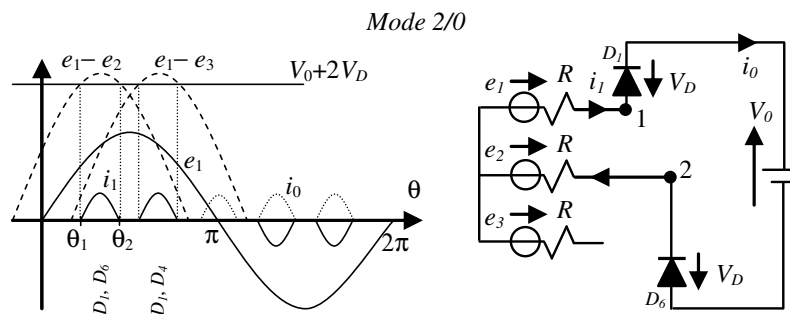


FIGURE 4.55 WAVEFORM AND A CONDUCTING DIODE PATTERN IN MODE 2/0

For instance, the diode D_1 firstly switches on when the voltage across it overcomes the threshold voltage V_D . This occurs at the angle θ_1 given by:

$$\theta_1 = \beta - \frac{\pi}{6} \quad (4.77)$$

where

$$\beta = \arcsin\left(\frac{(V_0 + 2V_D)}{\sqrt{6E}}\right) \quad (4.78)$$

Due to the symmetry of the switching pattern, the first pulse of the current i_1 extinguishes at the angle $\theta_2 = \frac{5}{6}\pi - \beta$. Since the AC inductance L has been neglected, the current i_1 in the interval $[\theta_1, \theta_2]$ is simply the steady state current which is forced by the line-to-line voltage $(e_1 - e_2) - (V_0 + 2V_D)$:

$$i_1^{(2/0)}(\theta) = \frac{1}{2R} \left(\sqrt{6E} \sin\left(\theta + \frac{\pi}{6}\right) - V_0 - 2V_D \right) \quad \theta \in [\theta_1, \theta_2] \quad (4.79)$$

The DC current i_0 consists of the superposition of current pulses like (4.79) progressively shifted by $\pi/3$. The angular period of i_0 is $\pi/3$, so that the average DC current $I_0^{(2/0)}$ is:

$$I_0^{(2/0)} = \frac{3}{\pi} \int_{\theta_1}^{\theta_2} i_1^{(2/0)}(\theta) d\theta = \frac{3}{\pi R} \left(\sqrt{6E} \cos \beta - (V_0 + 2V_D) \left(\frac{\pi}{2} - \beta \right) \right) \quad (4.80)$$

- **Mode 2/3.**

Mode 2/3 occurs if the phase voltage E increases enough to bring the angle θ_1 in (4.77) below $\pi/6$, so that the two positive current pulses of the phase 1 overlap each other. Thus, defining E_B the EMF value which defines the boundary between modes 2/0 and 2/3, it can be deduced starting from (4.78) with $\beta = \pi/3$:

$$\arcsin\left(\frac{(V_0 + 2V_D)}{\sqrt{6E_B}}\right) = \frac{\pi}{3} \quad (4.81)$$

And so the voltage E_B :

$$E_B = \frac{\sqrt{2}}{3} (V_0 + 2V_D) \quad (4.82)$$

Figure 4.56 shows three diode conducting patterns in the mode 2/3 and the current and voltage waveforms.

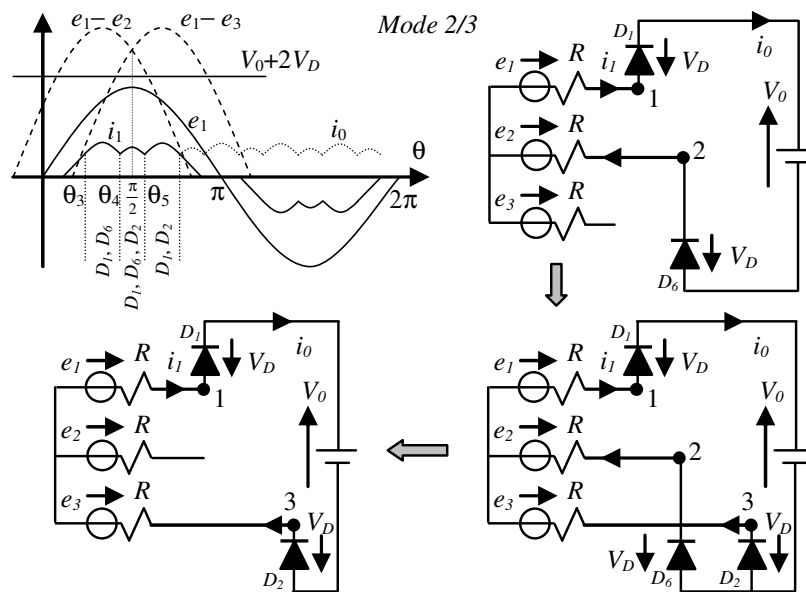


FIGURE 4.56 WAVEFORMS AND CONDUCTING DIODE PATTERNS IN MODE 2/3.

The switching angle θ_4 depicts the boundary between the patterns (D_1, D_6) and (D_1, D_6, D_2) . For θ which belongs to the interval $[\theta_3, \theta_4]$ the expression of the current (4.79) still holds, and at $\theta = \theta_4$ the voltage across D_2 equals V_D so that D_2 switches on. This remark allows to deduce the following expression of θ_4 :

$$\theta_4 = \arcsin\left(\frac{V_0 + 2V_D}{3\sqrt{2E}}\right) + \frac{\pi}{3} \quad (4.83)$$

Furthermore, the symmetry of the switching intervals with respect to $\pi/2$ period and the $\pi/3$ period of the current i_0 allows to calculate the angles θ_5 and θ_3 :

$$\theta_5 = \pi - \theta_4, \quad \theta_3 = \theta_5 - \pi/3 \quad (4.84)$$

Finally, the current related to diode pattern (D_1, D_6, D_2) can be calculated by solving the network in Figure 4.56 right-bottom corner.

$$i_1^{(2/3)}(\theta) = \frac{1}{R} \left(\sqrt{2E} \sin \theta - \frac{2}{3}(V_0 + 2V_D) \right), \quad \theta \in [\theta_4, \theta_5] \quad (4.85)$$

From (4.79) and (4.85) the average DC current $I_0^{(2/3)}$ results:

$$I_0^{(2/3)} = \frac{3}{\pi} \left(\int_{\theta_3}^{\theta_4} i_0^{(2/0)}(\theta) d\theta + \int_{\theta_4}^{\theta_5} i_0^{(2/3)}(\theta) d\theta \right) \quad (4.86)$$

The resulting final expression is:

$$I_0^{(2/3)} = \frac{3}{\pi R} \left(\sqrt{2E} \left(\frac{\sqrt{3}}{2} \left(\cos\left(\theta_3 + \frac{\pi}{6}\right) - \cos\left(\theta_4 + \frac{\pi}{6}\right) \right) + \cos\theta_4 - \cos\theta_5 \right) - \frac{V_0 + 2V_D}{6} (4\theta_5 - \theta_4 - 2\theta_3) \right) \quad (4.87)$$

By using (4.80) or (4.87), depending on the operation mode, and by considering also (4.66)-(4.74), the converted power P_0 can be expressed as a function of the parameters p and q . So the choice of the number of poles p and of the number of coils per pole-phase q , is driven by the power P_0 that can be obtained at the DC side given a desired DC voltage V_0 .

This way a systematic analysis can be performed by evaluating P_0 for every reasonable pair (p, q) . The results are summarized in a very meaningful way by drawing the iso- P_0 contour lines of the surface $P_0(p, q)$ in the plane (p, q) . In the same plane, equation (4.68), together with the constraint on the minimum value of b , is represented by a line which delimits the feasibility zone.

This procedure has been applied to a case study concerning the design of a PMSG for energy transfer on a train axle rotating at 180 r/min (mechanical frequency $f_m = 3$ Hz). The main geometrical quantities are reported in Table 26. The PM material is NeFeB N35H ($B_r = 1.017$ T, $m_{rev}/m_0 = 1.058$ at 80°C) The PM height has been set four times the total air-gap including the PCB thickness, in order to achieve a proper flux density in the air-gap. Shottky diodes STPS1L40A ($V_{Dmax} = 0.42$ V) for the rectifier as well as a DC voltage $V_0 = 4$ V have been considered. A copper resistivity $\rho_{cu} = 2.15 \cdot 10^{-8}$ ($\Omega \cdot m$) at 80 °C has been assumed.

TABLE 26 GEOMETRICAL DATA FOR THE CASE STUDY

D_{av} [mm]	l [mm]	g [mm]	h_m [mm]	a_m	d_{min} [mm]	s [mm]	b_{min} [mm]
227	13	3.2	12.8	0.75	0.4	0.105	0.6

Figure 4.57 shows the resulting P_0 contour lines in the plane (p, q) together with the limit line due to (4.68) and $b_{min} = 0.6$ mm. Furthermore, also the boundary line (blue dash-dot) between modes 2/0 and 2/3 is traced: this is simply the contour line related to (4.82), where E_B must be replaced by (4.71) which is a function of (p, q) thanks to (4.66)-(4.70) and (4.72). A satisfactory design is achieved by maximizing the amount of the extracted power P_0 inside the feasible zone.

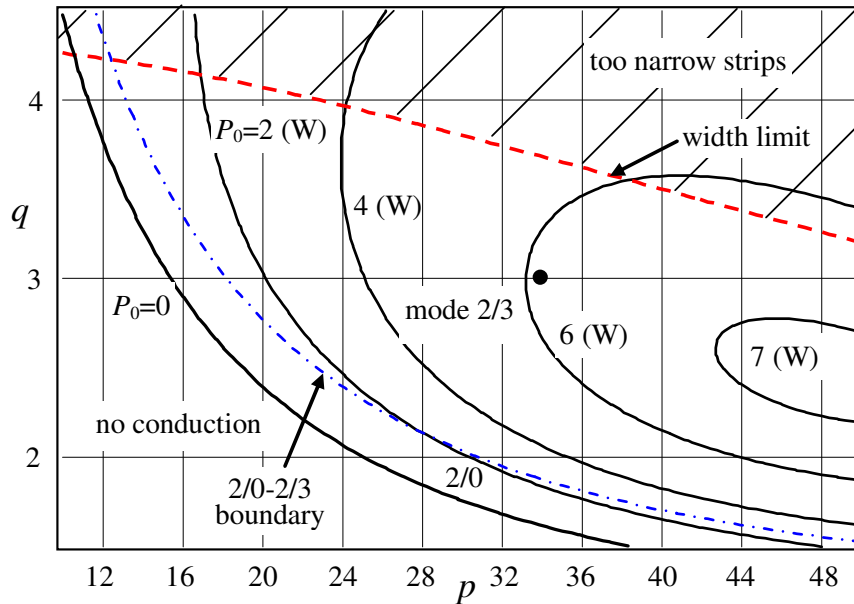


FIGURE 4.57 P_0 CONTOUR LINES (CONTINUOUS), MINIMUM STRIP WIDTH CONSTRAINT (RED-DASHED) WITH $b_{min}=0.6$ (mm), BOUNDARY BETWEEN MODES 2/0 AND 2/3 (BLUE-DASH-DOT). DIODE VOLTAGE DROP $V_D = 0.42$ V.

Of course the winding feasibility also requires p integer and even and q integer. For instance, a satisfactory design can be achieved by choosing $q = 3$ and $p = 34$. In fact, lower values of p are more desirable in order to limit the electrical frequency when the shaft speed increases. With this choice, (corresponding to the dot marked in the center of Figure 4.57) the transferred DC power, is $P_0 = 6.19$ W and the other electrical and magnetic quantities are reported in Table 27. In particular, the phase reactance at the frequency $f_m \cdot p/2 = 51$ Hz is: $X_L = 0.042 \Omega$, i.e. $X_L \approx R/30$. This justifies the approximation $L=0$ which has been considered in the steady state model of the bridge rectifier.

TABLE 27 FINAL ELECTRICAL PARAMETERS FOR THE CASE STUDY

p	q	f [Hz]	τ [mm]	B_1 [T]	φ [mWb]	E [V]	R [Ω]	L [mH]	P_0 [W]
34	3	51	21	0.74	0.0816	3.62	1.245	0.130	6.19

Here the diode characteristic has been simply modeled by a constant voltage drop, however a differential resistance could be also lumped in the winding resistance R . Anyway, the diode voltage drop have a remarkable impact on the performances of the whole system. This is confirmed by Figure 4.58, which reports the P_0 - contour lines in the case $V_D = 1.1$ V (V_{Dmax} of the diode 1N4002). Notice that the maximum power is roughly halved with respect to the previous case. In particular, with the choice $p=34$ and $q=3$, it results $P_0 = 3.72$ W.

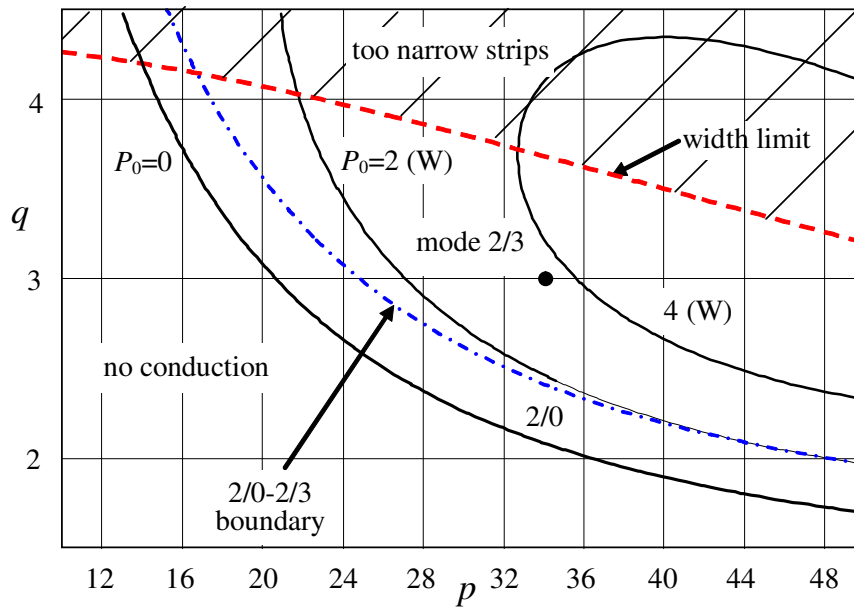


FIGURE 4.58 P_0 CONTOUR FOR THE CASE STUDY WHOSE DATA ARE REPORTED IN TABLE 26. DIODE VOLTAGE DROP $V_D = 1.1$ V.

Several simulations have been performed thanks to Simulink[®] (SimPowerSystem Toolbox) in order to validate the model of the machine and of the rectifying diode bridge: the power P_0 is computed as the average DC current times the DC voltage desired. Moreover, even if the model of the diode rectifier neglects the machine inductance, it still predicts quite accurate results with a small ac inductance added at the machine's model. With an inductive reactance less than 0.3 times the resistance, the P_0 error is less than 5%.

Figure 4.59 represents the Simulink[®] model used for the validation.

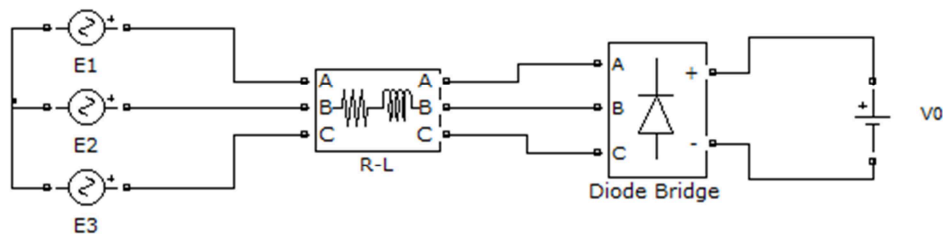


FIGURE 4.59 SIMULINK[®] MODEL FOR THE VALIDATION

Figure 4.60 shows the waveforms of the EMF e_1 , of the AC current i_1 and of the DC current i_0 as obtained from the simulation. The simulation parameters are set according to the data given in Table 27 and with $V_D = 0.42$ V. The simulation confirms that the rectifier is operating in the mode 2/3 and predicts a DC transferred power $P_0 = 6.12$ W. Thus the percentage error between the values of the transferred power obtained by the simulation and by the analytical model is 1.1%.

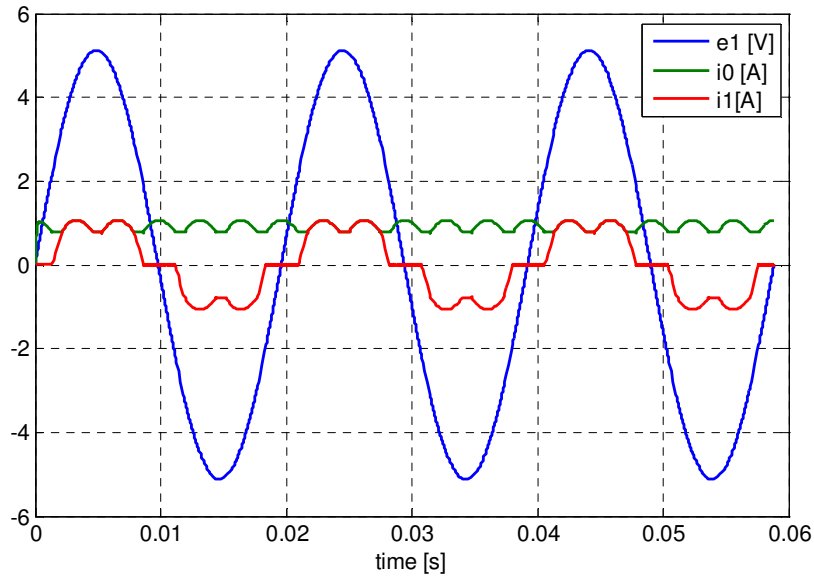


FIGURE 4.60 SIMULATION RESULTS (SIMULINK® - SIMPOWER SYSTEM TOOLBOX) OF THE RECTIFIER OPERATION WITH THE DATA IN TABLE 27

A simulation with the same data except for the diode voltage drop $V_D = 1.1$ gives $P_0 = 3.72$ W which is the same value obtained from the analytical computation.

The preliminary design has been based on the transferred power computed for the mechanical frequency of 3 Hz which corresponds to a train speed of 30km/h. Of course, the complete design also requires the evaluation of the performances of the machine in the operation above that speed. Since the internal EMF linearly increases with the speed, A DC-DC converter installation is expected in order to regulate the voltage after the diode rectifying conversion stage. This way the telemetry system can be properly powered starting from the voltage obtained at the minimum speed to the maximum voltage at the full speed of 300 km/h.

Moreover at high speed, and so at high frequency, the leakage inductance is more relevant and therefore a more accurate computation has to be adopted. These aspects will be examined in a future work.

REFERENCES

- [1] Agilent Technologies. Application Note 290-1—Practical Strain Gage Measurements.
- [2] www.witricity.com.
- [3] A. Kurs , A. Karalis, R. Moffatt , J. D. Joannopoulos, P. Fisher, M. Soljačić, Wireless Power Transfer via Strongly Coupled Magnetic Resonances, *Science* 6 July 2007: 317 (5834), 83-86. Published online 7 June 2007.
- [4] Maksimovic, D.; , "Design of the zero-voltage-switching quasi-square-wave resonant switch," *Power Electronics Specialists Conference, 1993. PESC '93 Record., 24th Annual IEEE* , vol., no., pp.323-329, 20-24 Jun 1993.
- [5] Vorperian, V.; Tymerski, R.; Lee, F.C.Y.; , "Equivalent circuit models for resonant and PWM switches," *Power Electronics, IEEE Transactions on* , vol.4, no.2, pp.205-214, Apr 1989.
- [6] Patterson, O.D.; Divan, D.M.; , "Pseudo-resonant full bridge DC/DC converter," *Power Electronics, IEEE Transactions on* , vol.6, no.4, pp.671-678, Oct 1991.
- [7] Vorperian, V.; , "Quasi-square-wave converters: topologies and analysis," *Power Electronics, IEEE Transactions on* , vol.3, no.2, pp.183-191, Apr 1988.
- [8] R. W. Erikson, D. Maksimovic, "Fundamentals of Power Electronics" Second Edition, Springer 2001.
- [9] N. Mohan, T. M. Undeland, W. P. Robbins, "Power Electronics: Converters, Applications and Design", Third Edition, John Wiley & Sons, 2003.
- [10] S. D. Freeland, Doctor of Philosophy Thesis, California Institute of Technology, 1988, "Input-Current Shaping for Single-Phase Ac-Dc Power Converters"
- [11] V. Vorperian, Doctor of Philosophy Thesis, California Institute of Technology, 1984, "Analysis of Resonant Converters"
- [12] J. Pyrhonen, T. Jokinen, V. Hrabovcova, "Design of Rotating Electrical Machines", John Wiley & Sons, 2008.
- [13] Bui Van Ha; Maglio, M.M.; Zich, R.E.; , "Contactless energy transfer in adverse environment using rectennas," *Electromagnetic Compatibility (AP EMC), 2012 Asia-Pacific Symposium on* , vol., no., pp.801-804, 21-24 May 2012.
- [14] Roberts, G.; Hadfield, P.; Humphries, M.E.; Bauder, F.; Izquierdo, J.M.G.; , "Design and evaluation of the power and data contactless transfer device," *Aerospace Conference, 1997. Proceedings., IEEE* , vol.3, no., pp.523-533 vol.3, 1-8 Feb 1997.
- [15] deBoeij, J.; Lomonova, E.; Duarte, J.; Vandenput, A.; , "Contactless Energy Transfer to a Moving Actuator," *Industry Applications Conference, 2006. 41st IAS Annual Meeting. Conference Record of the 2006 IEEE* , vol.4, no., pp.2020-2025, 8-12 Oct. 2006.
- [16] sobe, T.; Kobayashi, K.; Wakasugi, K.; Shimada, R.; , "Efficiency improvement of contactless energy transfer systems using series compensation device named MERS," *Power Electronics and Applications (EPE 2011), Proceedings of the 2011-14th European Conference on* , vol., no., pp.1-10, Aug. 30 2011-Sept. 1 2011.

- [17] Walsh, C.; Rondineau, S.; Jankovic, M.; Zhao, G.; Popovic, Z.; , "A conformal 10 GHz rectenna for wireless powering of piezoelectric sensor electronics," *Microwave Symposium Digest, 2005 IEEE MTT-S International* , vol., no., pp. 4 pp., 12-17 June 2005.
- [18] Marian, V.; Vollaire, C.; Allard, B.; Verdier, J.; , "Low power rectenna topologies for medium range wireless energy transfer," *Power Electronics and Applications (EPE 2011), Proceedings of the 2011-14th European Conference on* , vol., no., pp.1-10, Aug. 30 2011-Sept. 1 2011.
- [19] Hagerty, J.A.; Helmbrecht, F.B.; McCalpin, W.H.; Zane, R.; Popovic, Z.B.; , "Recycling ambient microwave energy with broad-band rectenna arrays," *Microwave Theory and Techniques, IEEE Transactions on* , vol.52, no.3, pp. 1014- 1024, March 2004.
- [20] McSpadden, J.O.; Lu Fan; KaiChang; , "Design and experiments of a high-conversion-efficiency 5.8-GHz rectenna," *Microwave Theory and Techniques, IEEE Transactions on* , vol.46, no.12, pp.2053-2060, Dec 1998.
- [21] Bassetti, M.; Braghin, F.; Castelli-Dezza, F.; Iacchetti, M.F.; Maglio, M.M.; , "Energy transfer on rotating shafts using pm-printed winding machine," *Electrical Machines (ICEM), 2012 XXth International Conference on* , vol., no., pp.664-670, 2-5 Sept. 2012.
- [22] L. Brown, D. Kuhlmann-Wilsdorf, W. Jesser, "Testing and Evaluation of Metal Fiber Brush Operation on Slip Rings and Commutators," *IEEE Trans. on Components and Packaging Technologies* , vol.31, no.2, pp.485-494, June 2008.
- [23] N. Morita, T. Ueno, T. Otaka, M. Arata, "Comparison of Brush Dynamic Operation Characteristics for Turbine Generator Steel Collector Ring," *Electrical contacts - 2007, the 53rd IEEE holm conference on* , vol., no., pp.205-210, 16-19 Sept. 2007.
- [24] C. Byungcho, N. Jaehyun, C. Honnyong, A. Taeyoung, C. Seungwon, "Design and implementation of low-profile contactless battery charger using planar printed circuit board windings as energy transfer device," *IEEE Trans. Ind. Electron.*, vol. 51, no. 1, pp. 140-147, Feb. 2004.
- [25] J. de Boeij, E. Lomonova, J. Duarte, A. Vandenput, "Contactless Energy Transfer to a Moving Actuator," *Industry Applications Conference, 2006. 41st IAS Annual Meeting. Conference Record of the 2006 IEEE* , vol.4, no., pp.2020-2025, 8-12 Oct. 2006.
- [26] T. Isobe, K. Kobayashi, K. Wakasugi, R. Shimada, "Efficiency improvement of contactless energy transfer systems using series compensation device named MERS," *Power Electronics and Applications (EPE 2011), Proceedings of the 2011-14th European Conference on* , vol., no., pp.1-10, Aug. 30 2011-Sept. 1 2011.
- [27] Mi-Ching Tsai; Liang-Yi Hsu; , "Design of a Miniature Axial-Flux Spindle Motor With Rhomboidal PCB Winding," *Magnetics, IEEE Transactions on* , vol.42, no.10, pp.3488-3490, Oct. 2006.
- [28] T.S. Low, M.A. Jabbar, T.S. Tan, "Design aspects and performance of a slotless PM motor for hard disk drives," *Industry Applications Magazine, IEEE* , vol.3, no.6, pp.43-51, Nov/Dec 1997.
- [29] G.H. Jang, J.H. Chang, "Development of an axial-gap spindle motor for computer hard disk drives using PCB winding and dual air gaps," *Magnetics, IEEE Transactions on* , vol.38, no.5, pp. 3297- 3299, Sep 2002.
- [30] A. Parviainen, M. Niemela, J. Pyronen, "Modeling of axial flux permanent-magnet machines," *IEEE Trans. Ind. Appl.*, vol.40, no. 5, pp. 1333-1340, Sept./Oct. 2004.

- [31] M-J. Chung, D. G. Gweon, "Modeling of the armature slotting effect in the magnetic field distribution of a linear permanent magnet motor," in Arch. Elektrotech., 202, vol. 84, pp. 101-108.
- [32] J.H. Davis, "Inductances of Printed Circuit Windings," Power Apparatus and Systems, IEEE Transactions on , vol.PAS-93, no.4, pp.1076-1082, July 1974.
- [33] M. Hancock, "Rectifier action with constant load voltage: Infinite capacitance condition," Proc. Inst. Elect. Eng., London 1973, vol. 120, no. 12, pp. 1529-1530.
- [34] K. L. Lian, B. K. Perkins, P.W. Lehn, "Harmonic analysis of a three-phase diode rectifier based on sampled-data model," IEEE Trans. Power Del., Vol. 23, No 2, Apr. 2008, pp. 1088-1096.
- [35] V. Caliskan, D. J. Perreault, T. M. Jahns, J. G. Kassakian, "Analysis of three-phase rectifiers with constant-voltage loads," IEEE Trans. Circuits Syst. I, Vol. 50, No 9, Sep. 2003, pp. 1220, 1226.
- [36] J. A. M. Bleijs, "Continuous conduction mode operation of three-phase diode bridge rectifier with constant load voltage," IEE Proc. Electr. Power Appl., vol. 152, no. 2, Mar. 2005, pp. 359-368.

CONCLUSIONS

This work has been focused on different aspects involving the diagnostic for the new generation of high speed trains.

During the three years of Ph.D. programme, the author had the possibility to face different constructional and analytical aspect regarding the maintenance in a wide and multidisciplinary sense. The topics followed the research activities that, at the time they were conducted, were considered important for the company and the research group the author worked with.

The first part has been centered on a possible cause of electric faults due to the electrical machine insulation stress. Basing on this topic, the insulation system has been studied under the light of a non-sinusoidal voltage feeding. The more recent standards indicate the type of tests and the construction techniques to respect for a proper insulation construction of a machine fed by an electronic power converter.

To deeply investigate on the square wave voltage feeding, a motor model has been derived to comprehend not only the low frequency operation but also the high frequency voltage oscillations and spikes that occur at the machine's terminals. A simulation model can help in predicting the overvoltage level and can be a useful tool for the design of a proper filter.

The overvoltage stress analysis continued also inside the machine's coil thanks to an analytical simplified model. Despite of the model simplified assumptions, the results can clearly show the impact of different insulation construction techniques on the voltage distribution inside a coil. Even if the correct parameters have not been derived, the simple algorithm can lead to interesting considerations about the coil construction and the insulation reinforcement in certain points.

After the first part focused on the insulation construction and on the voltage stress, the second part deals with the technology for a train axle telemetry system. In particular, starting from the strain gage features, the study has been pointed to the telemetry system power feeding. The strain gage together with the acquisition and data transfer unit placed on the rotating axle, requires a certain amount of electric power to work. Three different technologies have been evaluated to feed the telemetry without contacts and so avoiding brushes and slip rings. With the use of a high frequency magnetic field linked to a coil, a good amount of power can be transferred in a coreless transformer wound around the train axle. The advantage of the series resonant circuits for this technology are clearly shown with the use of an accurate analytical model validated with different system simulations.

The second technology is based on the RF power transmission which transfer capability, even if it requires small components and easy to build, remains very low. This leads to the use of more than one antenna to collect the proper amount of power. The transferred power has been verified trough a 3D computer simulation and a similar-concept system tests have been performed to investigate the power collected and the sensitivity to the axle rotational angle.

The third technology analyzed considers an electrical machine construction made with the support of a particular bearing. This idea involves the electromagnetic design of an axial-flux three-phase machine with PCB rotating windings to provide high robustness end good reliability.

The first solution is the one actually chosen from a steel manufacturing company which provides components for the trains, like the train axle, for its diagnostic research area. Performance tests on a similar design system have been done onboard which clearly show the good chance in using this power transmission system for the train axle telemetry equipment.

APPENDICES

In the following appendices, the command lines of Maple® are reported for the analytical and numerical computation of the power transfer system equations as reported in Chapter 4. The symbolic computation is used to derive the analytical expressions, where possible, or the numerical results to solve the system model and to derive the graphical results analyzed. Not all the results are shown explicitly because of their long form that would be of little use, but the computation formula are all reported in the files. The graphical results and power computations are also shown considering one of the cases as explained in Chapter 4.

APPENDIX A

restart

$$\alpha := \text{sqrt}(1 - \xi^2) :$$

$$vc := (\theta) \rightarrow (A \cdot \cos(\alpha \cdot \theta) + B \cdot \sin(\alpha \cdot \theta)) \cdot e^{-\xi \cdot \theta} - M \frac{\cos(\theta)}{2 \cdot \xi} :$$

$$sol1 := \text{diff}(vc(\theta), \theta) :$$

$$ic := (\theta) \rightarrow \left(-A \sin(\sqrt{1 - \xi^2} \theta) \sqrt{1 - \xi^2} + B \cos(\sqrt{1 - \xi^2} \theta) \sqrt{1 - \xi^2} \right) e^{-\xi \theta} - \left(A \cos(\sqrt{1 - \xi^2} \theta) + B \sin(\sqrt{1 - \xi^2} \theta) \right) \xi e^{-\xi \theta} + \frac{1}{2} \frac{\sin(\theta)}{\xi} :$$

#EQUATIONS :

$$eq3 := ic(\delta) = 0 :$$

$$eq4 := ic(\delta + \pi) = 0 :$$

$$eq5 := vc(\delta) + vc(\delta + \pi) = 0 :$$

$$sol2 := \text{solve}(\{eq3, eq5\}, \{A, B\}) :$$

$$A := \text{simplify}(\text{rhs}(sol2[1]))$$

$$\frac{1}{2} \frac{1}{\xi \left(\sqrt{1 - \xi^2} \cos(\sqrt{1 - \xi^2} \pi) + \xi \sin(\sqrt{1 - \xi^2} \pi) + \sqrt{1 - \xi^2} e^{\xi \pi} \right)} \left(e^{\xi \delta} \left(e^{\xi \pi} \sin(\delta) \sin(\sqrt{1 - \xi^2} \delta) + \sin(\delta) \sin(\sqrt{1 - \xi^2} \delta) \cos(\sqrt{1 - \xi^2} \pi) + \sin(\delta) \cos(\sqrt{1 - \xi^2} \delta) \sin(\sqrt{1 - \xi^2} \pi) + 4 e^{\xi \pi} M \sqrt{1 - \xi^2} \cos(\sqrt{1 - \xi^2} \delta) \xi - 4 \xi^2 e^{\xi \pi} M \sin(\sqrt{1 - \xi^2} \delta) \right) \right)$$

$$B := \text{simplify}(\text{rhs}(sol2[2]))$$

$$\frac{1}{2} \frac{1}{\xi \left(\sqrt{1 - \xi^2} \cos(\sqrt{1 - \xi^2} \pi) + \xi \sin(\sqrt{1 - \xi^2} \pi) + \sqrt{1 - \xi^2} e^{\xi \pi} \right)} \left(e^{\xi \delta} \left(4 e^{\xi \pi} M \sqrt{1 - \xi^2} \sin(\sqrt{1 - \xi^2} \delta) \xi + 4 \xi^2 e^{\xi \pi} \cos(\sqrt{1 - \xi^2} \delta) M - e^{\xi \pi} \cos(\sqrt{1 - \xi^2} \delta) \sin(\delta) - \sin(\delta) \cos(\sqrt{1 - \xi^2} \delta) \cos(\sqrt{1 - \xi^2} \pi) \right) \right)$$

$$+ \sin(\delta) \sin\left(\sqrt{1-\xi^2} \delta\right) \sin\left(\sqrt{1-\xi^2} \pi\right)\right)$$

$$\delta := \text{solve}(eq4, \delta)$$

$$-\arcsin\left(\frac{4 M \xi \sin\left(\sqrt{1-\xi^2} \pi\right) e^{\xi \pi}}{\sqrt{1-\xi^2} \left(2 \cos\left(\sqrt{1-\xi^2} \pi\right) e^{\xi \pi} + \left(e^{\xi \pi}\right)^2 + 1\right)}\right)$$

#MEAN CURRENT COMPUTATION

$$Io := (\xi, M) \rightarrow \left(\frac{1}{\pi} \cdot \int_{\delta(\xi, M)}^{\pi + \delta(\xi, M)} ic(\theta) d\theta \right) :$$

$$Po := (\xi, M) \rightarrow M \cdot Io(\xi, M)$$

$$(\xi, M) \rightarrow M Io(\xi, M)$$

#WINDING DATA

$$V1 := 5 :$$

$$k1 := 1 :$$

$$N1 := 4 :$$

$$Pm := 1.020508e-6 : \quad \text{\#MAGNETIZING PERMEANCE}$$

$$Pd2 := 2.68029e-7 : \quad \text{\#SECONDARY LEAKAGE PERMEANCE}$$

$$Pd1 := 8.85064e-7 : \quad \text{\#PRIMARY LEAKAGE PERMEANCE}$$

$$f := 30e3 :$$

$$w := \text{evalf}(2 \cdot \pi \cdot f) :$$

$$II := \frac{VI}{w \cdot Pm \cdot NI^2}$$

1.624547765

$$\rho := 1.7e-8 :$$

$$Dim := 0.195 :$$

$$\alpha CU := \frac{1}{10} :$$

$$Aw := 24 \cdot 1e-6 :$$

$$Ka := 1 + \frac{1}{9} :$$

$$\xi := \frac{9}{8} \cdot \frac{\rho \cdot Dim}{f \cdot (Pd1 + Pd2) \cdot \alpha CU \cdot Aw} \cdot Ka$$

0.04991105082

with(*plots*)

[*animate, animate3d, animatecurve, arrow, changecoords, complexplot, complexplot3d, conformal, conformal3d, contourplot, contourplot3d, coordplot, coordplot3d, densityplot, display, dualaxisplot, fieldplot, fieldplot3d, gradplot, gradplot3d, graphplot3d, implicitplot, implicitplot3d, inequal, interactive, interactiveparams, intersectplot, listcontplot, listcontplot3d, listdensityplot, listplot, listplot3d, loglogplot, logplot, matrixplot, multiple, odeplot, pareto, plotcompare, pointplot, pointplot3d, polarplot, polygonplot, polygonplot3d, polyhedra_supported, polyhedraplot, rootlocus, semilogplot, setcolors, setoptions, setoptions3d, spacecurve, sparsematrixplot, surfdata, textplot, textplot3d, tubeplot*]

plot1 := contourplot(-vc($\delta I(\xi, M)$) + sin($\delta I(\xi, M)$) - M, $\xi = 0.01 \dots 1$, $M = 0.001 \dots 1$, contours = [0], color = green, numpoints = 10000, resolution = 400)

PLOT(...)

plot2 := implicitplot($\xi = \xi$, $\xi = 0 \dots 1$, $M = 0 \dots 1$, color = blue)

PLOT(...)

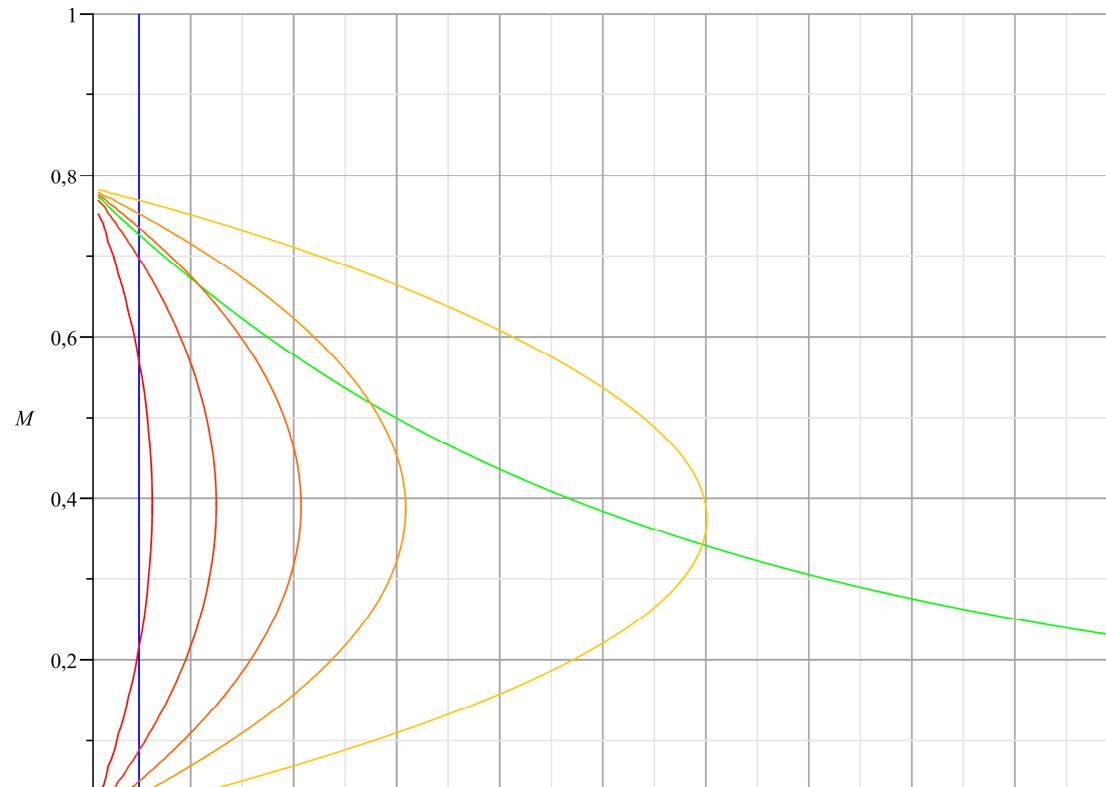
plot3 := contourplot(Po(ξ, M), $\xi = 0.01 \dots 1$, $M = 0.001 \dots 1$, contours = [1, 0.5, 0.3, 0.2, 0.1], gridlines, numpoints = 10000, resolution = 400)

$graph1 := (\{plot1, plot2, plot3\})$

$display(graph1)$

$PLOT(...)$

$\{PLOT(...), PLOT(...), PLOT(...)\}$



```
#display( {plot3, plot1} )
```

```
unwith(plots)
```

```
# WINDING CURVE AND CCM BOUNDARY CROSSING POINT
```

```
 $\xi := \xi :$ 
```

```
eq6 := -vc(  $\delta l(\xi, M)$  ) + sin(  $\delta l(\xi, M)$  ) - M = 0 :
```

```
sol3 := fsolve( {eq6}, {M} )
```

```
{M=0.7263078992}
```

```
Mlim := rhs(sol3[1])
```

```
0.7263078992
```

```
Vdc := 4 :
```

```
 $V_s := \frac{N2 \cdot V1 \cdot k1}{N1}$ 
```

```
 $\frac{5}{4} N2$ 
```

```
 $M1 := \frac{Vdc}{V_s}$ 
```

```
 $\frac{16}{5 N2}$ 
```

```
 $L := (Pd1 + Pd2) \cdot N2^2$ 
```

```
0.000001153093 N22
```

```
 $R := evalf(\xi \cdot 2 \cdot w \cdot L)$ 
```

```
0.02169662426 N22
```

$$\delta delay := evalf(\delta l(\xi, MI))$$

$$-1. \arcsin\left(\frac{0.1015963855}{N2}\right)$$

$$Popu := evalf(Po(\xi, MI))$$

$$\frac{24589.82807 \left(\frac{0.0033820809}{N2} - 0.02878031304 \sqrt{0.0008315809 - \frac{0.0000085834}{N2^2}} \right)}{N2}$$

$$Iopu := evalf(Io(\xi, MI))$$

$$-\frac{25.98899620}{N2} + 221.1571718 \sqrt{0.0008315809 - \frac{0.0000085834}{N2^2}}$$

$$C := \frac{1}{w^2 \cdot L}$$

$$\frac{0.00002440806877}{N2^2}$$

#BASE REFERENCE VALUES

$$Ib := w \cdot C \cdot Vs$$

$$\frac{5.751015715}{N2}$$

$$Pb := w \cdot C \cdot Vs^2$$

$$7.188769644$$

$$Pdc := Popu \cdot Pb$$

$$\frac{1.767706096 \cdot 10^5 \left(\frac{0.0033820809}{N2} - 0.02878031304 \sqrt{0.0008315809 - \frac{0.0000085834}{N2^2}} \right)}{N2}$$

#Pdc ZERO LIMIT

$$eq10 := Pdc = 0$$

$$\frac{1.767706096 \cdot 10^5 \left(\frac{0.0033820809}{N2} - 0.02878031304 \sqrt{0.0008315809 - \frac{0.0000085834}{N2^2}} \right)}{N2} = 0$$

sol10 := solve({eq10}, {N2})

{N2 = 4.076347067}

#N2 LIMIT FOR Pdc > 0

N2i := rhs(sol10[1])

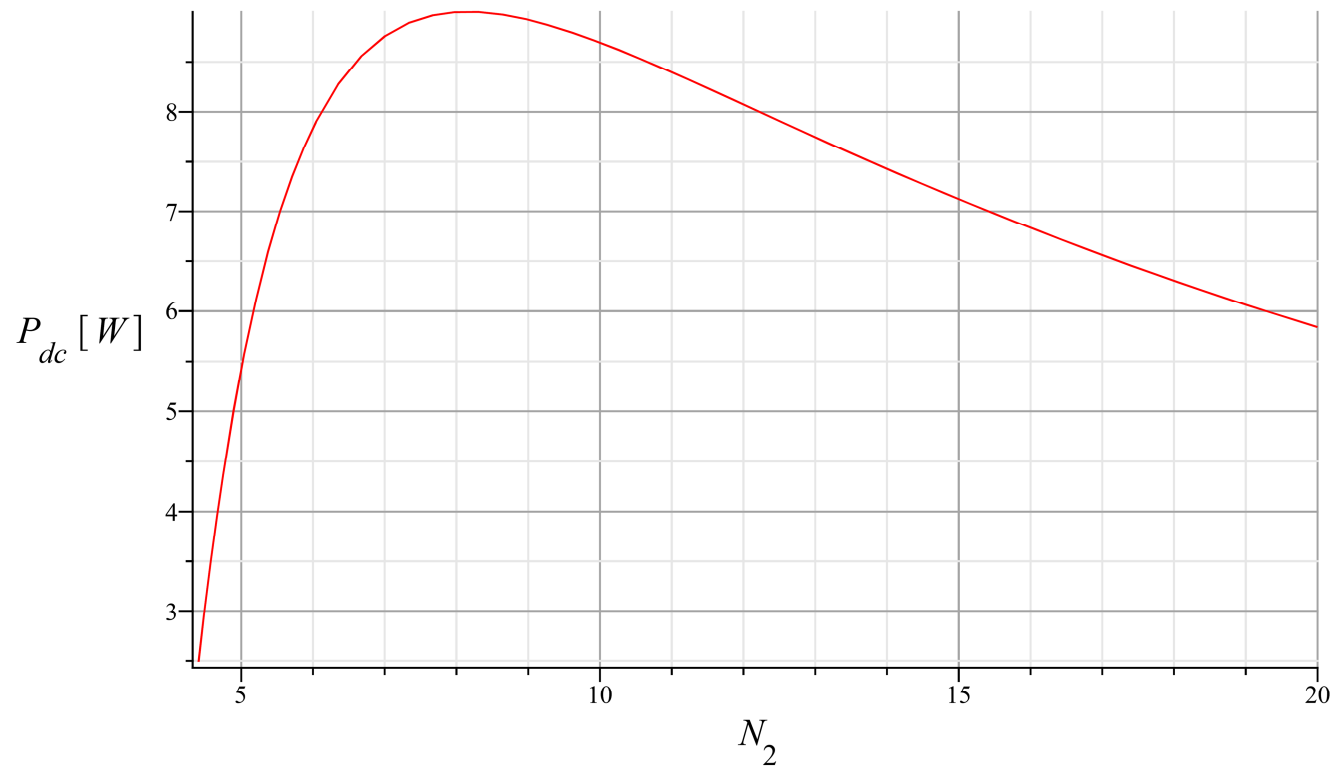
4.076347067

#N2 LIMIT FOR CCM ZONE OPERATION

N2lim := $\frac{\frac{V_{dc}}{M_{lim}} \cdot N1}{V1 \cdot k1}$

4.405844964

plot(Pdc, N2 = N2lim .. 20, gridlines, labels = [N2, P_{dc} [W]], labelfont = [15, 15])



N2 AT THE MAXIMUM POWER

$eq11 := diff(Pdc, N2) = 0 :$

$sol11 := fsolve(\{eq11\}, \{N2 = N2i..20\})$

$\{N2 = 8.152060981\}$

$N2 := 7 :$
 $M1$

$$\frac{16}{35}$$

$evalf(Vs)$

$$8.750000000$$

L

$$0.000056501557$$

C

$$4.981238524 \cdot 10^{-7}$$

R

$$1.063134589$$

$Pdc2 := Popu \cdot Pb$

$$8.755201133$$

$Idc := Iopu \cdot Ib$

$$2.188800285$$

$Rl := \frac{Vdc^2}{Pdc}$

$$1.827485144$$

$Ld1 := N1^2 \cdot Pd1$

$$0.000014161024$$

$Ld2 := N2^2 \cdot Pd2$

$$0.000013133421$$

$Lm := N1^2 \cdot Pm$

$$0.000016328128$$

$Cs1 := \frac{1}{w^2 \cdot Ld1}$

$$0.000001987481501$$

$$Cs2 := \frac{1}{w^2 \cdot Ld2}$$

0.000002142988734

$$R1 := \text{evalf}\left(\frac{N1^2 \cdot \rho \cdot \pi \cdot Dim}{\frac{2}{3} \cdot \alpha CU \cdot A\text{fin}}\right)$$

0.000002499451116

Afin

$$R2 := \text{evalf}\left(\frac{N2^2 \cdot \rho \cdot \pi \cdot Dim}{\frac{1}{3} \cdot \alpha CU \cdot A\text{fin}}\right)$$

0.00001530913808

Afin

$$A := \text{evalf}(A(\xi, MI))$$

6.290537468

$$B := \text{evalf}(B(\xi, MI))$$

0.3683846819

$$\alpha := \text{sqrt}(1 - \xi^2)$$

0.9987536668

$$ic := (\theta) \rightarrow (-A \sin(\alpha \cdot \theta) \cdot \alpha + B \cos(\alpha \cdot \theta) \cdot \alpha) e^{-\xi \theta} - (A \cos(\alpha \cdot \theta) + B \sin(\alpha \cdot \theta)) \xi e^{-\xi \theta} + \frac{1}{2} \frac{\sin(\theta)}{\xi} :$$

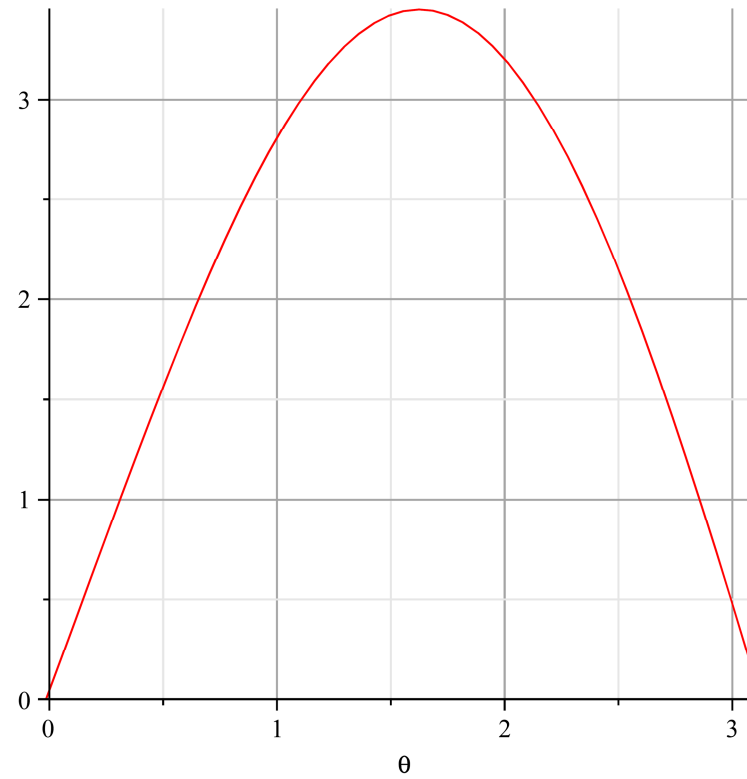
$$vc := (\theta) \rightarrow (A \cdot \cos(\alpha \cdot \theta) + B \cdot \sin(\alpha \cdot \theta)) \cdot e^{-\xi \cdot \theta} - MI - \frac{\cos(\theta)}{2 \cdot \xi}$$

$$\theta \rightarrow (A \cos(\alpha \theta) + B \sin(\alpha \theta)) e^{-\xi \theta} - MI - \frac{1}{2} \frac{\cos(\theta)}{\xi}$$

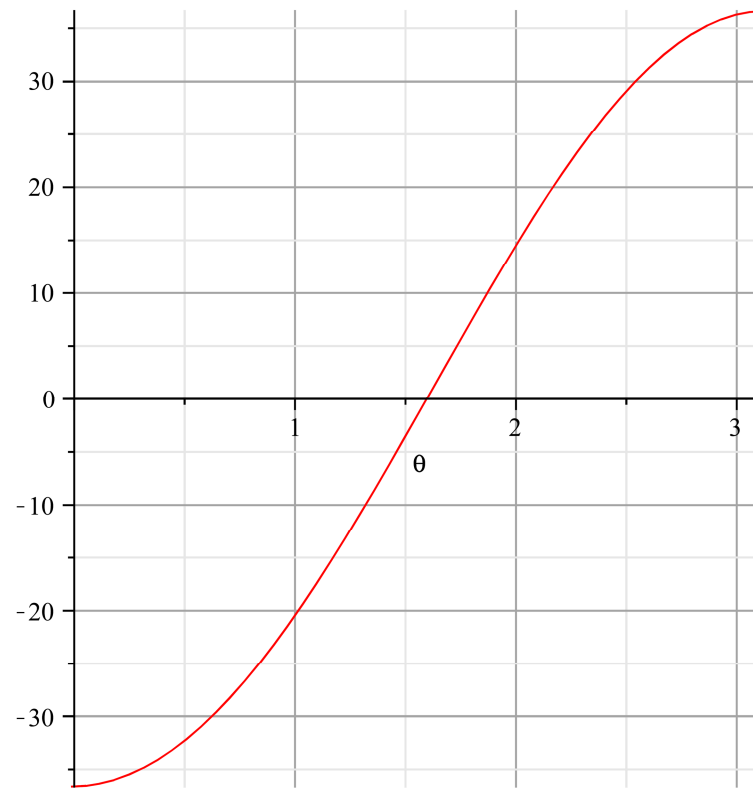
$\delta := \text{evalf}(\delta l(\xi, MI))$

-0.01451427659

$\text{plot}(ic(\theta) \cdot w \cdot C \cdot Vs, \theta = \delta.. \pi + \delta, \text{gridlines})$



`plot(vc(theta) * Vs, theta = delta..pi + delta, gridlines)`



APPENDIX B

restart

$$\alpha := \text{sqrt}(1 - \xi^2) :$$

$$vc := (\theta) \rightarrow (A \cdot \cos(\alpha \cdot \theta) + B \cdot \sin(\alpha \cdot \theta)) \cdot e^{-\xi \cdot \theta} - M - \frac{\cos(\theta)}{2 \cdot \xi} :$$

$$sol1 := \text{diff}(vc(\theta), \theta) :$$

$$ic := (\theta) \rightarrow \left(-A \sin(\sqrt{1 - \xi^2} \theta) \sqrt{1 - \xi^2} + B \cos(\sqrt{1 - \xi^2} \theta) \sqrt{1 - \xi^2} \right) e^{-\xi \theta} - \left(A \cos(\sqrt{1 - \xi^2} \theta) + B \sin(\sqrt{1 - \xi^2} \theta) \right) \xi e^{-\xi \theta} + \frac{1}{2} \frac{\sin(\theta)}{\xi} :$$

#EQUATIONS FOR $\theta1$:

$$eq3 := vc(\theta1) = \sin(\theta1) - M :$$

$$eq4 := ic(\theta1) = 0 :$$

$$sol1 := \text{solve}(\{eq3, eq4\}, \{A, B\}) :$$

$$A := \text{rhs}(sol1[1])$$

$$\frac{1}{2} \frac{1}{e^{-\xi \theta1} \xi \sqrt{1 - \xi^2}} \left(\sin(\theta1) \sin(\sqrt{1 - \xi^2} \theta1) + \sqrt{1 - \xi^2} \cos(\sqrt{1 - \xi^2} \theta1) \cos(\theta1) + 2 \sqrt{1 - \xi^2} \cos(\sqrt{1 - \xi^2} \theta1) \sin(\theta1) \xi - \xi \sin(\sqrt{1 - \xi^2} \theta1) \cos(\theta1) - 2 \xi^2 \sin(\sqrt{1 - \xi^2} \theta1) \sin(\theta1) \right)$$

$$B := \text{rhs}(sol1[2])$$

$$\frac{1}{2} \frac{1}{e^{-\xi \theta1} \xi \sqrt{1 - \xi^2}} \left(-\cos(\sqrt{1 - \xi^2} \theta1) \sin(\theta1) + \cos(\sqrt{1 - \xi^2} \theta1) \xi \cos(\theta1) + 2 \cos(\sqrt{1 - \xi^2} \theta1) \xi^2 \sin(\theta1) \right)$$

$$+ \sqrt{1-\xi^2} \cos(\theta l) \sin(\sqrt{1-\xi^2} \theta l) + 2 \sqrt{1-\xi^2} \sin(\theta l) \xi \sin(\sqrt{1-\xi^2} \theta l))$$

$$vc := (\theta) \rightarrow (A \cdot \cos(\alpha \cdot \theta) + B \cdot \sin(\alpha \cdot \theta)) \cdot e^{-\xi \cdot \theta} - M \cdot \frac{\cos(\theta)}{2 \cdot \xi} :$$

$$ic := (\theta) \rightarrow \left(-A \sin(\sqrt{1-\xi^2} \theta) \sqrt{1-\xi^2} + B \cos(\sqrt{1-\xi^2} \theta) \sqrt{1-\xi^2} \right) e^{-\xi \theta} - \left(A \cos(\sqrt{1-\xi^2} \theta) + B \sin(\sqrt{1-\xi^2} \theta) \right) \xi e^{-\xi \theta} + \frac{1}{2} \frac{\sin(\theta)}{\xi} :$$

#CONDITIONS FOR $\theta 1$ E $\theta 2$:

$$eq5 := ic(\theta 2) = 0 :$$

$$eq6 := vc(\theta 1) = -vc(\theta 2) :$$

$$Io := (\xi, \theta l) \rightarrow \frac{1}{\pi} \cdot \int_0^{\pi} ic(\theta) d\theta :$$

$$Po := (\xi, M, \theta l) \rightarrow Io(\xi, \theta l) \cdot M :$$

#WINDING DATA

$$Vl := 5 :$$

$$kl := 1 :$$

$$Nl := 4 :$$

$$Pd2 := 2.68029e-7 : \#SECONDARY LEAKAGE PERMEANCE$$

$$Pd1 := 8.85064e-7 : \#PRIMARY LEAKAGE INDUCTANCE$$

$$f := 30e3 :$$

$$w := evalf(2 \cdot \pi \cdot f) :$$

$$\rho := 1.7e-8 :$$

$$Dim := 0.195 :$$

$$\alpha CU := \frac{1}{10} :$$

$$Aw := 24 \cdot 1e-6 :$$

$$Ka := 1 + \frac{1}{9} :$$

$$\xi := \frac{9}{8} \cdot \frac{\rho \cdot Dim}{f \cdot (Pd1 + Pd2) \cdot \alpha CU \cdot Aw} \cdot Ka$$

0.04991105082

$$Vdc := 4 :$$

$$N2 := 4 :$$

$$Vs := \frac{N2 \cdot V1 \cdot k1}{N1}$$

5

$$M := \frac{Vdc}{Vs}$$

$\frac{4}{5}$

$$L := (Pd1 + Pd2) \cdot N2^2$$

0.000018449488

$$R := \text{evalf}(\xi \cdot 2 \cdot w \cdot L)$$

0.3471459882

$$C := \frac{1}{w^2 \cdot L}$$

0.000001525504298

$$\text{sol2} := \text{fsolve}\left(\{eq5, eq6\}, \left\{\theta1 = -\frac{\pi}{2} \dots \frac{\pi}{2}, \theta2 = \frac{\pi}{2} \dots \frac{3}{2} \cdot \pi\right\}\right)$$

{ $\theta1 = 0.6512478943, \theta2 = 2.914982983$ }

$$\theta1 := \text{rhs}(\text{sol2}[1])$$

0.6512478943

$$\theta2 := \text{rhs}(\text{sol2}[2])$$

2.914982983

$ic(\theta)$

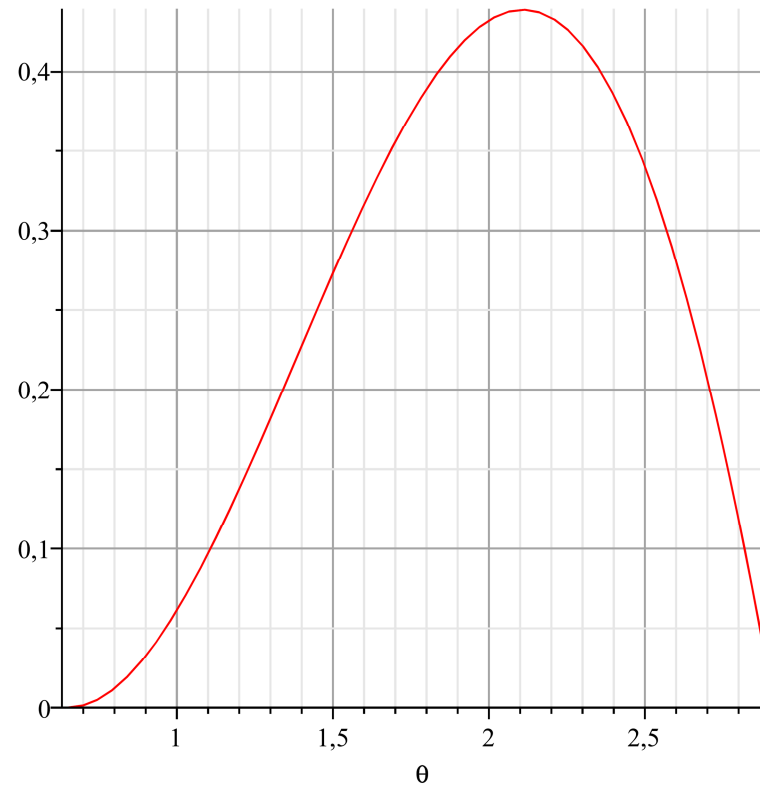
$$(-10.57067454 \sin(0.9987536668 \theta) + 0.7159026224 \cos(0.9987536668 \theta)) e^{-0.04991105082 \theta}$$

$$- 0.04991105082 (10.58386556 \cos(0.9987536668 \theta) + 0.7167959890 \sin(0.9987536668 \theta)) e^{-0.04991105082 \theta} + 10.01782154 \sin(\theta)$$

$evalf(Po(\xi, M, \theta1, \theta2))$

0.1034801573

$plot(ic(\theta) \cdot w \cdot C \cdot Vs, \theta = \theta1 .. \theta2, gridlines)$



$$I_o := \text{evalf} \left(\frac{1}{\pi} \cdot \int_{\theta_l}^{\theta_2} ic(\theta) \, d\theta \right)$$

0.1233900512

$$P_o := I_o \cdot M$$

0.09871204096

$$I_b := w \cdot C \cdot V_s$$

1.437753928

$$P_b := w \cdot C \cdot V_s^2$$

7.188769642

$$P_{dc} := P_o \cdot P_b$$

0.7096181234

$$I_{dc} := I_o \cdot I_b$$

0.1774045308

$$R_l := \frac{V_{dc}^2}{P_{dc}}$$

22.54733845

APPENDIX C

restart

$$i := (\theta) \rightarrow A \cdot e^{-2 \cdot \xi \cdot \theta} + \frac{1}{4 \cdot \xi^2 + 1} \cdot (2 \cdot \xi \cdot \sin(\theta) - \cos(\theta)) - \frac{M}{2 \cdot \xi} :$$

$$eq2 := i(\delta) = 0$$

$$A e^{-2 \xi \delta} + \frac{2 \xi \sin(\delta) - \cos(\delta)}{4 \xi^2 + 1} - \frac{1}{2} \frac{M}{\xi} = 0$$

solve(eq2, A) :

$$A := e^{2 \xi \delta} \cdot \left(\frac{1}{4 \cdot \xi^2 + 1} \cdot (\cos(\delta) - 2 \cdot \xi \cdot \sin(\delta)) + \frac{M}{2 \cdot \xi} \right) :$$

i(θ) :

$$eq3 := i(\delta + \pi) = 0$$

$$e^{2 \xi \delta} \left(\frac{\cos(\delta) - 2 \xi \sin(\delta)}{4 \xi^2 + 1} + \frac{1}{2} \frac{M}{\xi} \right) e^{-2 \xi (\delta + \pi)} + \frac{\cos(\delta) - 2 \xi \sin(\delta)}{4 \xi^2 + 1} - \frac{1}{2} \frac{M}{\xi} = 0$$

solve(eq3, δ) :

$$\#Io := (\xi, M) \rightarrow \left(\frac{1}{\pi} \cdot \int_{\delta(\xi, M)}^{\pi + \delta(\xi, M)} ic(\theta) d\theta \right) :$$

$$Io := (\xi, M) \rightarrow -\frac{1}{2} \frac{1}{\pi \xi^2 (4 \xi^2 + 4 \xi^2 e^{2 \xi \pi} + 1 + e^{2 \xi \pi})} \left(-4 M \xi^2 e^{2 \xi \pi} - M e^{2 \xi \pi} \right. \\ \left. - 2 \sqrt{-\xi^2 (4 \xi^2 + 1) (4 M^2 \xi^2 e^{4 \xi \pi} - 8 M^2 \xi^2 e^{2 \xi \pi} + 4 M^2 \xi^2 - 8 \xi^2 e^{2 \xi \pi} - 4 \xi^2 e^{4 \xi \pi} - 4 \xi^2 + M^2 - 2 M^2 e^{2 \xi \pi} + M^2 e^{4 \xi \pi})} + 4 M \xi^3 e^{2 \xi \pi} \pi \right. \\ \left. + 4 M \xi^3 \pi + 4 M \xi^2 + \xi M e^{2 \xi \pi} \pi + \xi M \pi + M \right) :$$

$$Po := (\xi, M) \rightarrow M \cdot Io(\xi, M) :$$

#WINDING DATA

$V1 := 5 :$
 $k1 := 1 :$
 $N1 := 4 :$
 $Pm := 1.020508e-6 : \#MAGNETIZING PERMEANCE$
 $Pd2 := 2.68029e-7 : \#SECONDARY LEAKAGE INDUCTANCE$
 $Pd1 := 8.85064e-7 : \#PRIMARY LEAKAGE INDUCTANCE$

$f := 30e3 :$
 $w := \text{evalf}(2 \cdot \pi \cdot f) :$

$$II := \frac{V1}{w \cdot Pm \cdot N1^2}$$

1.624547765

$\rho := 1.7e-8 :$
 $Dim := 0.195 :$
 $\alpha CU := \frac{1}{10} :$
 $Aw := 24 \cdot 1e-6 :$
 $Ka := 1 + \frac{1}{9} :$

$$\xi := \frac{9}{8} \cdot \frac{\rho \cdot Dim}{f \cdot (Pd1 + Pd2) \cdot \alpha CU \cdot Aw} \cdot Ka$$

0.04991105082

with(plots)

[animate, animate3d, animatecurve, arrow, changecoords, complexplot, complexplot3d, conformal, conformal3d, contourplot, contourplot3d, coordplot, coordplot3d, densityplot, display, dualaxisplot, fieldplot, fieldplot3d, gradplot, gradplot3d, graphplot3d, implicitplot, implicitplot3d, inequal, interactive, interactiveparams, intersectplot, listcontplot, listcontplot3d, listdensityplot, listplot, listplot3d, loglogplot, logplot, matrixplot, multiple, odeplot, pareto, plotcompare, pointplot, pointplot3d, polarplot, polygonplot, polygonplot3d, polyhedra_supported, polyhedraplot, rootlocus, semilogplot, setcolors, setoptions, setoptions3d, spacecurve, sparsematrixplot, surfdata, textplot, textplot3d, tubeplot]

```
plot3 := contourplot(Po( $\xi$ , M),  $\xi = 0.01 \dots 1$ , M = 0.001 ..1, contours = [0.18, 0.15, 0.12, 0.09, 0.06], gridlines, numpoints = 10000, resolution = 400)
```

PLOT(...)

```
plot2 := implicitplot( $\xi = \xi^2$ ,  $\xi = 0 \dots 1$ , M = 0 ..1, color = blue)
```

PLOT(...)

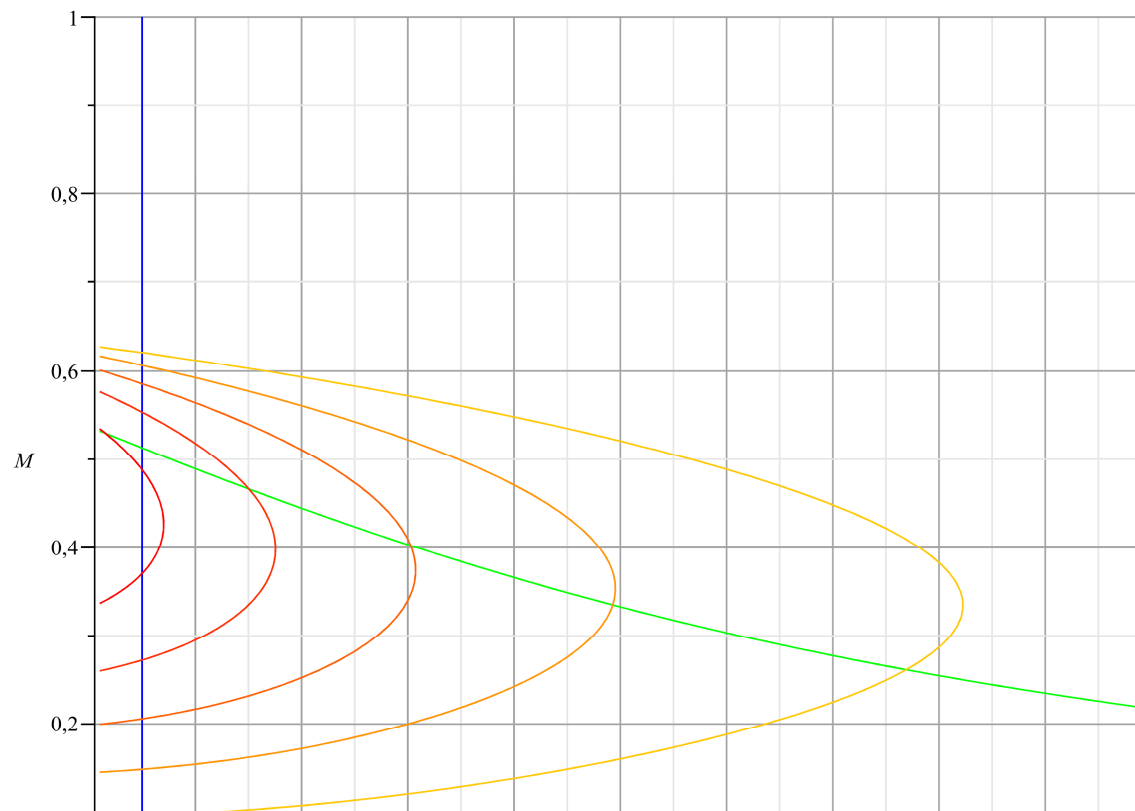
```
plot1 := contourplot(sin( $\delta$ ) - M,  $\xi = 0.01 \dots 1$ , M = 0.001 ..1, contours = [0], color = green, numpoints = 10000, resolution = 400)
```

PLOT(...)

```
graph1 := ({plot1, plot2, plot3})
```

{PLOT(...), PLOT(...), PLOT(...)}

```
display(graph1)
```



$$\xi := \xi$$

$$0.04991105082$$

$$eq6 := \sin(\delta) - M = 0 :$$

$$sol3 := fsolve(\{eq6\}, \{M\})$$

$$\{M = 0.5129721276\}$$

$$Mlim := rhs(sol3[1])$$

$$0.5129721276$$

$$Vdc := 4 :$$

$$Vs := \frac{N2 \cdot V1 \cdot k1}{N1}$$

$$\frac{5}{4} N2$$

$$M := \frac{Vdc}{Vs}$$

$$\frac{16}{5 N2}$$

$$L := (Pd1 + Pd2) \cdot N2^2$$

$$0.000001153093 N2^2$$

$$R := evalf(\xi \cdot 2 \cdot w \cdot L)$$

$$0.02169662426 N2^2$$

$$evalf(\delta)$$

$$\arctan\left(-\frac{1.178696954}{N2} + 198.7332290 \sqrt{-\frac{0.00353028654}{N2^2} + 0.0001406183718}, \frac{11.80797618}{N2} + 19.83796859 \sqrt{-\frac{0.00353028654}{N2^2} + 0.0001406183718}\right)$$

$$Ib := \frac{Vs}{R} \cdot 2 \cdot \xi$$

$$\frac{5.751015714}{N2}$$

$$Pb := Ib \cdot Vs$$

$$7.188769642$$

$$Popu := \text{evalf}(Po(\xi, M))$$

$$\frac{85.47242561 \left(\frac{0.0097402341}{N2} - 2 \cdot \sqrt{-\frac{0.00353028653}{N2^2} + 0.0001406183718} \right)}{N2}$$

$$Iopu := \text{evalf}(Io(\xi, M))$$

$$-\frac{0.2601629482}{N2} + 53.42026600 \sqrt{-\frac{0.00353028653}{N2^2} + 0.0001406183718}$$

$$Pdc := Popu \cdot Pb$$

$$\frac{614.4415785 \left(\frac{0.0097402341}{N2} - 2 \cdot \sqrt{-\frac{0.00353028653}{N2^2} + 0.0001406183718} \right)}{N2}$$

$$eq10 := Pdc = 0$$

$$\frac{614.4415785 \left(\frac{0.0097402341}{N2} - 2 \cdot \sqrt{-\frac{0.00353028653}{N2^2} + 0.0001406183718} \right)}{N2} = 0$$

#N2 LIMIT FOR Pdc > 0

$$sol10 := \text{solve}(\{eq10\}, \{N2\})$$

$$\{N2 = 5.027336537\}$$

$$N2i := \text{rhs}(sol10[1])$$

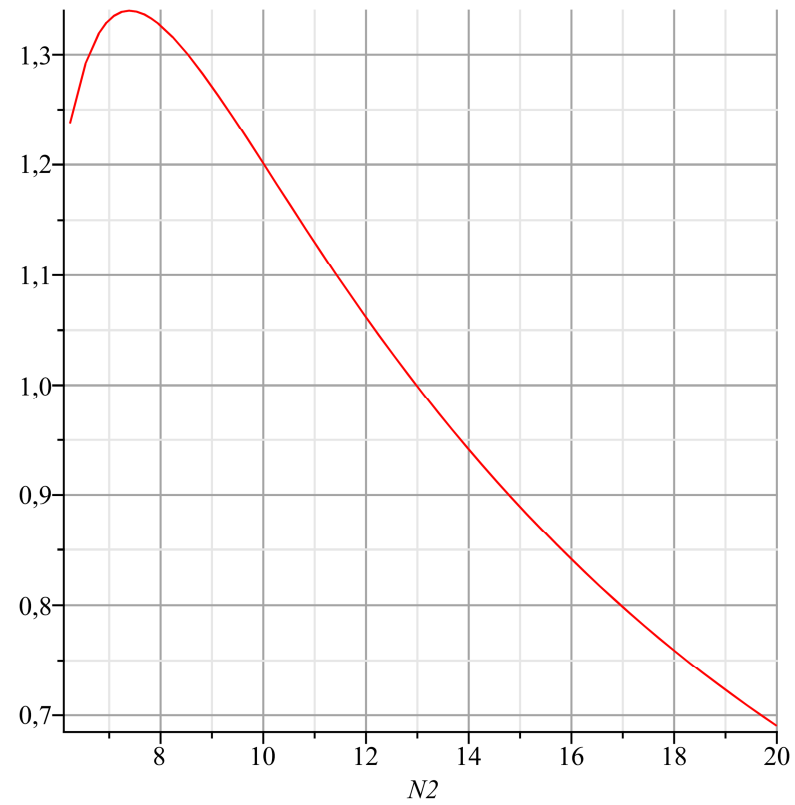
$$5.027336537$$

#N2 LIMIT FOR CCM OPERATION

$$N2lim := \frac{\frac{Vdc}{Mlim} \cdot N1}{V1 \cdot k1}$$

6.238155696

plot(Pdc, N2 = N2lim ..20, gridlines)



N2 AT THE MAXIMUM POWER

$eq11 := \text{diff}(Pdc, N2) = 0 :$

$sol11 := \text{fsolve}(\{eq11\}, \{N2 = N2i .. 20\})$

$N2max := \text{rhs}(sol11[1])$ {N2 = 7.394431641}

7.394431641

$N2 := \text{ceil}(N2lim)$

7

$Pdc2 := Popu \cdot Pb$

1.331595419

$Idc2 := Iopu \cdot Ib$

0.3328988545

$Rload := \frac{Vdc^2}{Pdc2}$

12.01566164

$\text{evalf}(Vs)$

8.750000000

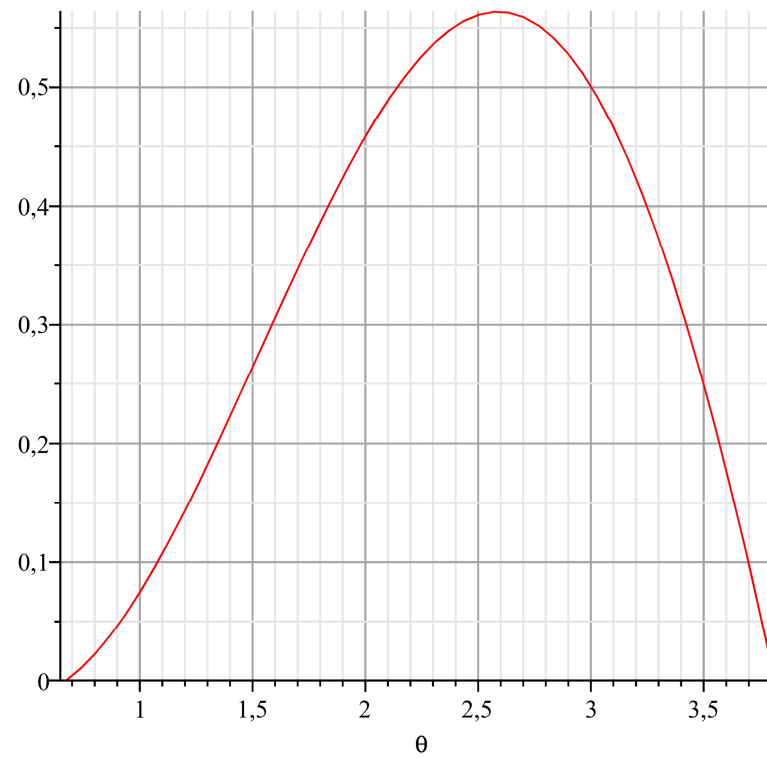
L

0.000056501557

R

1.063134589

$\text{plot}(Ib \cdot i(\theta), \theta = \delta .. \delta + \pi, \text{gridlines})$



APPENDIX D

restart

$$i := (\theta) \rightarrow A \cdot e^{-2 \cdot \xi \cdot \theta} + \frac{1}{4 \cdot \xi^2 + 1} \cdot (2 \cdot \xi \cdot \sin(\theta) - \cos(\theta)) - \frac{M}{2 \cdot \xi} :$$

$$eq2 := i(\theta l) = 0$$

$$A e^{-2 \xi \theta l} + \frac{2 \xi \sin(\theta l) - \cos(\theta l)}{4 \xi^2 + 1} - \frac{1}{2} \frac{M}{\xi} = 0$$

solve(eq2, A) :

$$A := e^{2 \xi \theta l} \cdot \left(\frac{1}{4 \cdot \xi^2 + 1} \cdot (\cos(\theta l) - 2 \cdot \xi \cdot \sin(\theta l)) + \frac{M}{2 \cdot \xi} \right)$$

$$e^{2 \xi \theta l} \left(\frac{\cos(\theta l) - 2 \xi \sin(\theta l)}{4 \xi^2 + 1} + \frac{1}{2} \frac{M}{\xi} \right)$$

i(θ) :

$$eq3 := i(\theta l) = 0$$

$$e^{2 \xi \theta l} \left(\frac{\cos(\theta l) - 2 \xi \sin(\theta l)}{4 \xi^2 + 1} + \frac{1}{2} \frac{M}{\xi} \right) e^{-2 \xi \theta l} + \frac{2 \xi \sin(\theta l) - \cos(\theta l)}{4 \xi^2 + 1} - \frac{1}{2} \frac{M}{\xi} = 0$$

$$eq4 := \sin(\theta l) - M = 0$$

$$\sin(\theta l) - M = 0$$

Vdc := 4 :

VI := 5 :

kl := 1 :

NI := 4 :

$Pd2 := 2.68029e-7$: #SECONDARY LEAKAGE PERMEANCE
 $Pd1 := 8.85064e-7$: #PRIMARY LEAKAGE PERMEANCE

$f := 30e3$:

$w := evalf(2 \cdot \pi \cdot f)$:

$\rho := 1.7e-8$:

$Dim := 0.195$:

$\alpha CU := \frac{1}{10}$:

$Aw := 24 \cdot 1e-6$:

$Ka := 1 + \frac{1}{9}$:

$\xi := \frac{9}{8} \cdot \frac{\rho \cdot Dim}{f \cdot (Pd1 + Pd2) \cdot \alpha CU \cdot Aw} \cdot Ka$

0.04991105082

$N2 := 6$:

$Vs := \frac{N2 \cdot V1 \cdot k1}{N1}$

$\frac{15}{2}$

$M := \frac{Vdc}{Vs}$

$\frac{8}{15}$

$L := (Pd1 + Pd2) \cdot N2^2$

0.000041511348

$R := evalf(\xi \cdot 2 \cdot w \cdot L)$

0.7810784734

$$sol2 := fsolve\left(\{eq3, eq4\}, \left\{\theta_1 = -\frac{\pi}{2} \dots \frac{\pi}{2}, \theta_2 = \frac{\pi}{2} \dots \frac{3}{2} \cdot \pi\right\}\right)$$

$$\{\theta_1 = 0.5625362445, \theta_2 = 3.626596394\}$$

$$\theta_1 := rhs(sol2[1])$$

$$0.5625362445$$

$$\theta_2 := rhs(sol2[2])$$

$$3.626596394$$

$$i(\theta)$$

$$6.481619911 e^{-0.09982210164 \theta} + 0.09883724268 \sin(\theta) - 0.9901338587 \cos(\theta) - 5.342838155$$

$$I_b := \frac{V_s}{R} \cdot 2 \cdot \xi$$

$$0.9585026190$$

$$P_b := I_b \cdot V_s$$

$$7.188769642$$

$$I_o := evalf\left(\frac{1}{\pi} \cdot \int_{\theta_1}^{\theta_2} i(\theta) d\theta\right)$$

$$0.3074389170$$

$$P_o := evalf(I_o \cdot M)$$

$$0.1639674224$$

$$I_{dc} := I_o \cdot I_b$$

$$0.2946810071$$

$$P_{dc} := P_o \cdot P_b$$

$$1.178724028$$

`plot(Ib·i(θ), θ = θ1 ..θ2, gridlines)`

